THE UNIVERSITY OF CHICAGO

PROBING QUANTUM DYNAMICS AND SPECTRAL BROADENING IN SEMICONDUCTOR NANOCRYSTALS WITH NONLINEAR SPECTROSCOPIES

A DISSERTATION SUBMITTED TO
THE FACULTY OF THE DIVISION OF THE PHYSICAL SCIENCES
IN CANDIDACY FOR THE DEGREE OF
DOCTOR OF PHILOSOPHY

DEPARTMENT OF CHEMISTRY

BY
NICHOLAS EDWARD WILLIAMS

CHICAGO, ILLINOIS
JUNE 2019

In loving memory of my father, Edward T. Williams

TABLE OF CONTENTS

LIST OF FIGURES

ACKNOWLEDGMENTS

There are many people that I have met and relied on through my time at UChicago that have made this experience very worthwhile, and without whom this dissertation would not have been possible. First, I would like to thank Professor Greg Engel who has been a supportive mentor and always encouraged me to solve interesting problems both in and out of the lab. Thanks to your willingness to let me take on opportunities to grow as a leader and develop my management, communication, and strategy skills, I'm sure that I'll have the ability and confidence to take on whatever comes next. Thank you for giving me the space and resources to grow throughout graduate school; I will be forever grateful.

To all the members of the Engel Group that I've gotten to work with over the years, nothing that I've done could be possible without each of you. I'm so glad that our group has been able to cultivate an environment where I was encouraged to ask questions, to be wrong, and to learn about chemistry, physics, biology, and how to succeed at being an adult. In particular, I want to thank Lili Wang who taught me everything I know, usually by trial and a lot of error. Of course, Sara Massey and Moira Flanagan were always there to talk through lots of strategies and scientific ideas and be "plain ol' buddies." Finally, I was so happy to have a smart, fun, and encouraging group of younger students that have come up in recent years especially Ryan Wood, Richard Mazuski, Lawson Lloyd, Elizabeth Bain, Sara Sohail, and Jake Higgins.

I want to thank everyone from my year in the Chemistry program, especially Dr. Daniel Micheroni, Darren Veit, Dr. Anthony Schlimgen, Dr. Nicole James, Dr. John Otto, Dr. Michael Leukheide, who spent long nights doing problems sets and pubbing together during our first year and who have really helped each other talk though career goals, academic issues, and everything in between since then.

I have had the pleasure of collaborating with many people while at the University of Chicago, and I am so grateful to have worked with all of them. Most importantly, I would like to thank the members of my committee, Professor Sarah King and Professor Steven

Sibener for your ideas and guidance while writing and finalizing my thesis. I also want to thank Professor Dmitri Talapin for all of the help that I received from him and many members of his group across a number of different projects, especially Eric Janke who was instrumental in producing the work in chapter 3, as well as Dr. Pat Cunningham, Dr. Vishwas Srivastava, Wooje Cho, and Dr. Igor Fedin for their chats and advice on nanoscience. Finally, I would like to acknowledge Prof. Phillipe Guyot-Sinnest and Dr. Edward W. Malachosky for providing their experience and working to characterize and understand the photophysics of the nanocrystals in chapter 4.

About three years ago, I started getting involved and taking leadership roles at the university. I want to take the time to thank Casey Anthony, Katie Perri, and Dr. Anthony Martinez for reeling me in to this fledgling organization called Graduate Council and encouraging me to take on a finance role that I had absolutely no experience in, but that turned out to be the start of very fun and rewarding journey. Thanks to Megan Beck, Jake Nebergall, and Carlos Grandet-Callabero for working with me to build Grad Council from a group of people into a business. Finally, thanks to Joseph Dang for helping me turn that business into a stand-alone government and deal with new political strategies or personnel issues every day.

I have also had the help of many friends and family members throughout the years that helped me accomplish this work and deal with stresses of graduate school. I want to thank my mom, Elaine for always being so loving and supportive and coming out to visit often despite the long distance. I know that the entire group would like to thank you for the constant stream of cookies and care packages that made their way down to the office. I also want to thank my girlfriend Jess Pontis for being the best and getting me through the toughest parts of the past two years. I'm looking forward to spending lots of relaxing time with you and Reggie very soon.

ABSTRACT

Semiconductor nanocrystals (NCs) are becoming increasingly entrenched in modern consumer technologies. Their versatility and capability to produce light emitting devices with high photoluminescence quantum yield, solar cells with excellent power conversion efficiencies, and extendibility to many other applications and industries including biotechnology have made NCs an exciting area of research and engineering. To realize the next generation of devices that use NCs effectively, it is important to understand how these nanoscale materials function at the quantum level using an array of techniques that can probe the electronic structure, morphology and size distributions, and ultrafast carrier dynamics that result in their remarkable macroscopic behavior. In this thesis I use two-dimensional electronic spectroscopy (2DES) to examine these properties and aid synthetic efforts to optimize these materials for various applications. In chapter 3, InP quantum dots are examined using many techniques includes 2DES to explain their broad emission spectra by understanding the electronic structure of emissive defects in the nanocrystalline lattice. Chapter 4 presents work in developing a novel synthesis of methylammonium lead-halide perovskites and using 2DES to probe the ultrafast dynamics of these NCs that are used in effective solar harvesting devices. In chapter 5, thin films of CdSe nanoplatelets are probed using 2DES with various pump laser powers, both at room temperature and 77K to gain insight into these materials that are used in low-threshold laser applications. Finally, chapter 6 concludes the thesis by proposing some future directions for our group as we continue to explore the quantum dynamics and electronic structure of interesting nanomaterials.

CHAPTER 1

INTRODUCTION

1.1 Semiconductor Nanocrystals

Semiconductor nanocrystals (NCs) are materials that exist on the mesoscale between bulk crystals and single molecules. While chemists typically focus on manipulating chemical composition to achieve desired material properties, nanocrystals offer a route toward engineering quantum properties more directly through changing the material's size, shape, and local environment.[1, 2] Nanocrystals are small enough that the electronic wavefunction is larger than the boundary of the material itself, which confines charged particles together, often producing desirable effects, like improved photoluminescence quantum yield, that are useful for a range of optoelectronic applications. However, while chemists have learned to measure the composition and structure of small molecules through well-optimized analytical techniques, accessing actionable information for materials that consist of thousands of atoms proves very challenging and has required researchers to adapt existing spectroscopies and microscopies to understand nanocrystal formation, sample homogeneity, quantum yield, and ultrafast dynamics. Significant progress has been made on nanomaterial design and discovery in the past three decades, with semiconductor NCs now being routinely produced in very homogeneous batches through size selection techniques, which provide narrow fluorescence linewidths, in addition to techniques like implementing a core-shell coating that have improved the quantum yields tremendously.[3, 4] However, many challenges remain as we begin to face problems related not only to size inhomogeneity, but other complex sources of broadening that can be very difficult to isolate. In this thesis, I will aim to understand some of these issues using a novel type of spectroscopy that has proven to be very effective at revealing lineshape and sources of broadening in order to help guide synthetic efforts toward nanomaterial discovery and design.

1.2 Improving Semiconductor Nanocrystals by Understanding Electronic Structure and Quantum Dynamics

Semiconductor nanocrystals have emerged over the past three decades as a novel class of materials that can be used to solve impactful problems across many industries from consumer lighting[5–13] to biomedical sensing,[14–19] transistors,[20, 21] and solar cell technology.[22] These materials are so versatile because they are self-assembled via cost-effective, scalable solution processing methods, they are optically active and capable of high quantum yields and narrow emission lines, and their small size (∼1-10 nm) provides a large surface area which can catalyze chemical reactions or be functionalized for a diverse set of applications.[23] Because of their potential impact across many industries, intense research efforts have been directed at creating new nanocrystalline compounds, altering the morphology and composition of existing materials to yield new properties, or refining synthetic techniques to tailor the properties of existing NCs for a given application. To achieve these goals, many characterization methods are used to help researchers understand the impact of different synthetic recipes on macroscopic device properties. Particle size distribution and morphology, fluorescence quantum yield, ultrafast carrier dynamics, and charge carrier mobility are all examples of quantities that are commonly characterized through a variety of techniques to develop a complete picture of why a given material performs the way it does. In this thesis, I will use two-dimensional electronic spectroscopy (2DES), an ultrafast spectroscopic technique that can reveal electronic structure, state-to-state relaxation dynamics, electronic and electron-phonon coupling, and segment sources of spectral broadening,[24] applying this method to semiconductor NCs. Two-dimensional electronic spectroscopy can complement many other methods and build a more complete picture of the electronic structure and carrier dynamics that drive macroscopic properties of semiconductor nanocrystals. Taken together, they can be used to create a holistic explanation of the behavior of a class of nanomaterials and inform synthetic efforts to optimize a material for a set of diverse applications. Semiconductor

nanocrystals exhibit unique properties because at least one spatial dimension of the crystal is constrained to a size that is smaller than its electronic wavefunction. This confinement gives rise to distinct quantum states with narrow emission and absorption profiles, like atoms, while maintaining some material characteristics of the bulk crystal. Confining in one dimension creates materials called quantum wells or nanoplatelets, while nanowires or nanorods and quantum dots result from confining the wavefunction in two and three dimensions, respectively. CdSe quantum dots have found success in modern LED display technologies because their narrow emission features, large quantum yield, and high degree of tunability can potentially result in brighter screens and a wider color gamut.[11] In this dissertation, I will be focusing on InP quantum dots, which currently compete with CdSe in the QLED display market, lead-halide perovskite quantum dots, which are a popular class of materials for solar energy conversion, and CdSe nanoplatelets, which are 2D materials that have shown excellent potential for low-threshold laser gain media. I will be using two-dimensional electronic spectroscopy (2DES) to probe the electronic structure and excited state dynamics of these materials with the goal of better understanding the tradeoffs between synthetic capabilities and macroscopic behavior.

1.3 Spectroscopy

In this thesis I will be focusing on how nanomaterials absorb visible light, transfer that energy through different quantum states of the system, and ultimately dissipate that energy either radiatively or non-radiatively. This involves a detailed knowledge of the material's electronic structure and the interactions between excited charge carriers and the surrounding environment. In the case of colloidal semiconductor nanocrystals, the environment of the material is quite complex and involves not only a solvent, but the ligand environment, any trap states that may exist either embedded in the quantum dot or on the surface, and the phonon vibrations or other excitations in the crystal. An excitation is created in any material by absorbing energy from an external oscillating electric field whose frequency is resonant

with the energy gap between the electronic ground state and an excited state of the system. In a spectroscopic technique like linear absorption, we detect these energy gaps by measuring changes in the intensity of an incident electric field as the oscillation frequency is scanned. This can be done in either the time domain or the frequency domain via a Fourier transform, the latter yielding the familiar linear spectrum as a function of the wavelength. For an ensemble of nanocrystals in solution, each nanocrystal can have a slightly different size and shape, and therefore have a different absorption spectrum, resulting in inhomogeneous broadening of the peak linewidth. Additionally, quantum states have an intrinsic linewidth due to their characteristic decoherence time, known as the homogeneous linewidth. Finally, a quantum state on an individual nanocrystal can experience fluctuations over intermediate timescales between the instantaneous homogeneous limit and the static inhomogeneous limit as the state dephases when it responds to changes in its local environment. In most applications of semiconductor nanomaterials, it is desirable to have very narrow absorption and emission linewidths, meaning that limiting these sources of broadening is a major goal of nanomaterial design. However, it is not possible to separate these sources of broadening using linear spectroscopy. Therefore, it is difficult to determine why one material has broader linewidths than another. One way to separate inhomogeneous and homogeneous broadening is to turn to nonlinear spectroscopic techniques such as two-dimensional electronic spectroscopy. Two-dimensional electronic spectroscopy (2DES) is an ultrafast spectroscopic technique that uses short (10^{-15} fs) laser pulses to track changes in the excited state dynamics of a system that absorbs visible light.[25, 26] In a 2DES experiment, three distinct laser pulses are used to interact with the sample, with specified time delays between each pulse. By scanning these time delays, a frequency-frequency correlation map is generated that relates the energy used to excite the system, with the detected energy that is emitted by the system in response to interactions with the three pulses. These 2D spectra are captured at different waiting times (T), during which the system can evolve, explore the excited state, and eventually relax to the ground state.[27–29] One benefit of this technique is that it can resolve homogeneous and

inhomogeneous sources of broadening. If a material, like an ensemble of nanocrystals with different shapes and sizes, is excited by a broadband 2DES setup, larger nanocrystals will absorb and emit light redder than smaller crystals. This manifests in a 2D spectrum as a peak that remains diagonally elongated after long waiting times. Most 2D spectra will show diagonally elongated features at very short waiting times because the system has not had the opportunity to explore all microstates of the system, but if there are no sources of inhomogeneous broadening, the feature will round out and become circular over time. In addition to the lineshape, 2D spectra also provide information about how electronic states couple to one another through off-diagonal peaks.[24] A higher lying excited state may relax to a lower lying state such as a material band edge over the course of a few hundred femtoseconds to tens or hundreds of picoseconds. In a 2DES experiment, this is revealed by a crosspeak in the lower diagonal of the spectrum that grows in over the waiting time. Alternatively, upper diagonal peaks may appear in a spectrum that are either positive and induced by electronic coupling between states, or negative and resulting from excited state absorption from a lower lying excited state to a higher lying excited state. Finally, by following a peak in the 2D spectrum over time, by Fourier transforming along the waiting time axis, it is possible to map out coherences between excited electronic states or between electronic and vibrational states since these manifest as oscillations in the intensity of the signal at a point over time.[30, 31] There are many excellent reviews further detailing the technique, theory, and results of 2D spectroscopy,[32–34] and I will expand upon this section in chapter 2 of this thesis by outlining the theory of nonlinear spectroscopy and describe how our group acquires and processes 2D spectra.

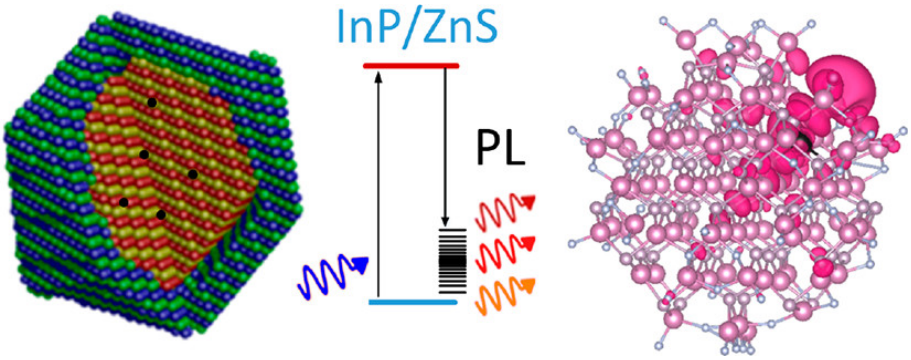

Figure 1.1: Electronic structure calculations along with experimental results show that hole states in ZnS-capped and HF-etched InP quantum dots become localized via shallow trap states. The delocalized electron recombines with this trapped hole to produce broad emission spectra both due to the number of states in the trap manifold and the strong electron-phonon coupling caused by localization of the hole.

1.4 Nanomaterial Systems

1.4.1 InP Quantum Dots

Colloidal quantum dots (QDs) have emerged as an important class of tunable light emitters that have narrow emission line widths and saturated colors that are suitable for commercial lighting and display technologies.[5–8, 35] Many of the current products using quantum dots involve cadmium[36] or lead-based[37, 38] materials because they have proven to have the best performance in terms of narrow linewidths, high quantum yield, and emission tunability. However, for consumer lighting and display devices, or biological labeling and imaging technologies, it is desirable to develop nanomaterials that do not contain toxic heavy metals and can rival the performance of QDs such as CdSe. Indium Phosphide QDs provide a promising alternative to Cd and Pb-based QDs but have not been capable of producing the quantum yields or color purity needed to compete with existing technologies, though significant recent progress in InP QD synthesis has been made.[39]

Recent studies have shown that the emission linewidths of single InP QDs is narrow and very comparable to CdSe single particle linewidths.[40–42] Therefore, it is apparent that the broad ensemble linewidths of InP QDs must be due to inhomogeneous broadening.

Typically, inhomogeneous broadening in QD systems is due to variations in size and/or morphology of the QDs in the ensemble. Therefore, it should be possible to prepare high-performance InP QDs by properly selecting for a narrow enough distribution of sizes. In this project, we examine InP/ZnS core-shell QDs and lightly HF-etched core-only InP QDs to determine the origin of their broad emission linewidths using a variety of theoretical models, characterization methods, and spectroscopic tools including ultrafast techniques like transient absorption and two-dimensional electronic spectroscopy (2DES).

We find that the broad emission linewidths are not due to sample size inhomogeneity but rather due to variations in the lattice disorder introduced by surface trap passivation methods. Upon HF-etching the surface or coating the core InP QD in a shell of ZnS, the lattice becomes disordered and causes defects such as Zn dopants into the crystal lattice. These states then introduce a new phonon-coupled, radiative recombination channel with broad emission spectra due to both electron-phonon coupling and variations in the electronic structure of the defect states.

1.4.2 Perovskite Quantum Dots

Organic-inorganic lead-halide hybrid perovskite materials have drawn much recent interest because of the remarkable photophysical properties of both bulk crystals and nanoscale materials. In the bulk phase, microcrystals of lead-halide perovskites have proven to be a promising material for solar cell applications because of their weak exciton binding energies,[43] efficient photogeneration of charge carriers,[44, 45] high charge carrier mobilities,[46, 47] and bimolecular charge recombination dynamics.[48] These factors combine to make lead-halide perovskite-based photovoltaic devices capable of obtaining power conversion efficiencies of up to 23%.[49–53] While bulk phase perovskites have promising performance for photovoltaic devices, the characteristics that make them excellent solar harvesters, also make them very poor light emitters. By confining the carriers produced by light absorption, lead-halide perovskite quantum dots (QDs) have proven to be good emitters at room temperature without

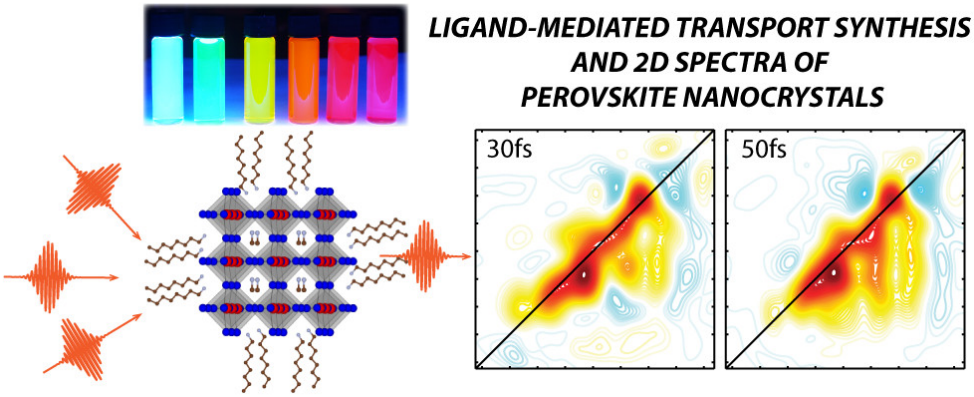

Figure 1.2: Methyl-Ammonium Lead Halide Perovskite quantum dots were synthesized through a novel ligand-mediated transport method and probed using two-dimensional electronic spectroscopy. The 2D spectra reveal sub-50 fs relaxation dynamics of multiple electronic states as well as electronic coherences that dephase rapidly at room temperature.

the need for a shell layer or other surface passivation methods.[54–58] These materials can be tuned over the entire visible spectrum not only by changing the size of the QDs, but also the composition.[59–62] For example, methyl-ammonium lead chloride ($MAPbCl_3$) QDs have blue emission at around 410 nm, while $MAPbI_3$ QDs emit as red as 700 nm. The colors in-between can be obtained by doping in Br- ions to form hybrid QDs.

We developed an atmospheric pressure, room temperature synthesis of $MAPbX_3$ (X = Br, I, or a mixture of the two) QDs that is industrially scalable, not requiring the typical external temperature and inert atmosphere controls of hot injection methods. These QDs are colloidally stable in atmosphere and can be concentrated to 0.2 OD in a 200 μm sample cell. This concentration is high enough for us to easily perform two-dimensional electronic spectroscopy (2DES) on a range of sizes and compositions of $MAPbX_3$ QDs. The broadband 2DES experiments reveal multiple electronic states that shift with the size of the nanocrystals and display fast (<100 fs) relaxation to the photoluminescent state as well as electronic coupling between higher-lying excited states.

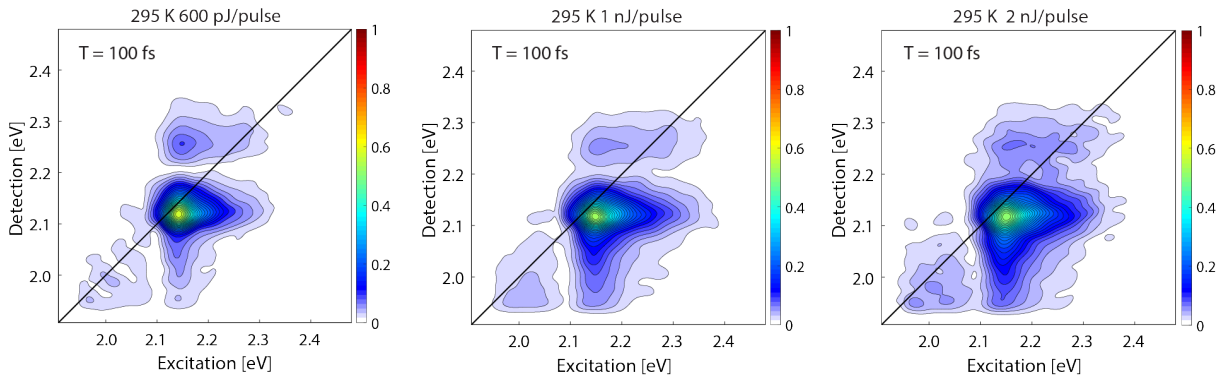

Figure 1.3: 6 ML CdSe nanoplatelets were probed using two-dimensional electronic spectroscopy at various excitation powers and at both room temperature and 77K. Shown here are room temperature 2D spectra at left: 600 pJ/pulse, center: 1 nJ/pulse, and right: 2 nJ/pulse.

1.4.3 CdSe Nanoplatelets

CdSe Nanoplatelets (NPLs) are two-dimensional materials that have a well-defined, few-atomic layer height, and lateral dimensions on the order of hundreds of nanometers.[63] Due to their structure, they have a very sharp absorption and emission profile, similar to expitaxial quantum wells, with high photoluminescence quantum yields (∼40%) even for bare nanoplatelets without a surface passivating shell layer.[64] Through synthetic controls, it is possible to change the thickness of NPLs so that they form into an ensemble with a specific number of atomic monolayers (MLs). CdSe NPL syntheses have been developed that yield thicknesses of 2-5 MLs,[63, 65–68] which produce emission lines from 396 nm to 553 nm. Recently, Cho et al.[69] developed a method for refining the synthesis and post-synthetic processing of 6 ML NPLs that gives a homogeneous distribution and a sharp photoluminescence emission feature at 583 nm. Here, we report a study of these novel 6 ML NPLs using two-dimensional electronic spectroscopy (2DES) to better understand the electronic structure of these materials as well as their ultrafast carrier dynamics under different excitation conditions and at both room temperature and 77K. We find that for thin films of 6 ML NPLs, very clean 2DES spectra can be obtained at room temperature with distinct excitonic features representing the heavy hole and light hole states.

Also, electronic coherences between the two excitonic states indicated by oscillatory features can be observed since both the upper and lower diagonal crosspeaks have quantum beating signals at the same energy as the separation between the two states that dissapates within 40 fs. Upon changing the excitation power, the relaxation rate does not change indicating second-order excitonic recombination, as expected. However, if the power is increased to more than 2 nJ/pulse from our femtosecond laser source, multiexciton effects begin to significantly affect the spectra, limiting our ability to interpret the lineshape and dynamics as higher order nonlinear processes start to dominate. Interestingly, the signal at low temperature (77K) appears to photobleach at much lower powers than at room temperature, but more investigations are necessary to determine the causes of this counterintuitive behavior.

1.5 Outline of Dissertation

The purpose of this work is to develop strategies for uncovering the design principles of semiconductor nanomaterials by examining the electronic structure, ultrafast carrier dynamics, and inter-particle couplings that drive useful macroscopic properties like photoluminescence quantum yield. I use two-dimensional electronic spectroscopy (2DES) to study a variety of nanomaterial systems and use the information gained from this powerful technique to better inform their synthesis. In chapter 2, I will layout the basic terminology and physics that will be used throughout the thesis both for semiconductor systems and nonlinear spectroscopies. Then, in chapter 3 I use 2DES along with a variety of other characterization techniques to learn how crystal lattice disorder impacts the photoluminescence properties of InP quantum dots. In chapter 4, I present a novel synthetic approach to lead-halide perovskite quantum dots and use 2DES to examine their electronic structure and gain insight into ultrafast dynamics and quantum beating signals of these materials. In chapter 5, I again use 2DES to investigate the excitonic properties of a novel synthesis of CdSe nanoplatelets devised by the Talapin group. Finally, in chapter 6, I provide examples of future directions for the Engel group to pursue as we continue to build on the foundation of using our cutting-edge ultrafast

spectroscopic techniques, touching both on new sample avenues to investigate as well as ways to improve our 2DES apparatus to better meet the pace of the constantly evolving field of nanomaterial discovery.

REFERENCES

[1] Al. L Efros and Efros A. L. "Interband absorption of light in a semiconductor sphere". In: *Soviet Physics Semiconductors* 16 (1982), pp. 772–775.

[2] L E Brus. "A simple model for the ionization potential, electron affinity, and aqueous redox potentials of small semiconductor crystallites". en. In: *The Journal of Chemical Physics* 79.11 (Dec. 1983), pp. 5566–5571. ISSN: 0021-9606.

[3] C B Murray, D J Norris, and M G Bawendi. "Synthesis and characterization of nearly monodisperse CdE (E = sulfur, selenium, tellurium) semiconductor nanocrystallites". EN. In: *Journal of the American Chemical Society* 115.19 (Sept. 1993), pp. 8706–8715. ISSN: 0002-7863.

[4] Margaret A. Hines and Philippe Guyot-Sionnest. "Synthesis and Characterization of Strongly Luminescing ZnS-Capped CdSe Nanocrystals". In: *The Journal of Physical Chemistry* 100.2 (Jan. 1996), pp. 468–471. ISSN: 0022-3654.

[5] Dmitri V. Talapin, Jong-Soo Lee, Maksym V. Kovalenko, and Elena V. Shevchenko. "Prospects of Colloidal Nanocrystals for Electronic and Optoelectronic Applications". In: *Chemical Reviews* 110.1 (2009), pp. 389–458.

[6] Dmitri V. Talapin and Jonathan Steckel. "Quantum dot light-emitting devices". In: *MRS Bulletin* 38.9 (2019), pp. 685–691.

[7] Yasuhiro Shirasaki, Geoffrey J. Supran, Moungi G. Bawendi, and Vladimir Bulović. "Emergence of colloidal quantum-dot light-emitting technologies". In: *Nature Photonics* 7.1 (2012), p. 13. ISSN: 1749-48931749-4893.

[8] V. L. Colvin, M. C. Schlamp, and A. P. Alivisatos. "Light-emitting diodes made from cadmium selenide nanocrystals and a semiconducting polymer". In: *Nature* 370.6488 (2019), p. 354. ISSN: 1476-46871476-4687.

[9] Al. L. Efros and M. Rosen. "The Electronic Structure of Semiconductor Nanocrystals". In: *Annual Review of Materials Science* 30.1 (2000), pp. 475–521.

[10] Alexander H. Mueller, Melissa A. Petruska, Marc Achermann, Donald J. Werder, Elshan A. Akhadov, Daniel D. Koleske, Mark A. Hoffbauer, and Victor I. Klimov. "Multicolor Light-Emitting Diodes Based on Semiconductor Nanocrystals Encapsulated in GaN Charge Injection Layers". In: *Nano Letters* 5 (2005), pp. 1039–1044.

[11] Geoffrey J. Supran, Yasuhiro Shirasaki, Katherine W. Song, Jean-Michel Caruge, Peter T. Kazlas, Moungi G. Bawendi, and Vladimir Bulović. "QLEDs for displays and solid-state lighting". In: *MRS Bulletin* 38 (2019), pp. 703–711.

[12] Bhola N. Pal, Istvan Robel, Aditya Mohite, Rawiwan Laocharoensuk, Donald J. Werder, and Victor I. Klimov. "High-Sensitivity p–n Junction Photodiodes Based on PbS Nanocrystal Quantum Dots - Pal - 2012 - Advanced Functional Materials - Wiley Online Library". In: *Advanced Functional Materials* 22 (2019).

[13] Jan W. Stouwdam and René A. J. Janssen. "Red, green, and blue quantum dot LEDs with solution processable ZnO nanocrystal electron injection layers". In: *Journal of Materials Chemistry* 18 (2008), pp. 1889–1894.

[14] Paul Alivisatos. "The use of nanocrystals in biological detection". In: *Nature Biotechnology* 22.1 (2003), p. 47. ISSN: 1546-16961546-1696.

[15] Brad A. Kairdolf, Andrew M. Smith, Todd H. Stokes, May D. Wang, Andrew N. Young, and Shuming Nie. "Semiconductor Quantum Dots for Bioimaging and Biodiagnostic Applications". In: *http://dx.doi.org/10.1146/annurev-anchem-060908-155136* (2013).

[16] I. V. Martynenko, A. P. Litvin, F. Purcell-Milton, A. V. Baranov, A. V. Fedorov, and Y. K. Gun'ko. "Application of semiconductor quantum dots in bioimaging and biosensing". In: *Journal of Materials Chemistry B* 5 (2017), pp. 6701–6727.

[17] Igor L. Medintz, H. Tetsuo Uyeda, Ellen R. Goldman, and Hedi Mattoussi. "Quantum dot bioconjugates for imaging, labelling and sensing". In: *Nature Materials* 4.6 (2005), p. 435. ISSN: 1476-46601476-4660.

[18] Shuming Nie, Yun Xing, Gloria J. Kim, and Jonathan W. Simons. "Nanotechnology Applications in Cancer". In: *http://dx.doi.org/10.1146/annurev.bioeng.9.060906.152025* (2007).

[19] A. M. Smith, M. M. Wen, and S. Nie. "Imaging dynamic cellular events with quantum dots The bright future". In: *Biochem (Lond)* 32.3 (2010), pp. 12–. ISSN: 0954-982X (Print).

[20] Jaeyoung Jang, Dmitriy S. Dolzhnikov, Wenyong Liu, Sooji Nam, Moonsub Shim, and Dmitri V. Talapin. "Solution-Processed Transistors Using Colloidal Nanocrystals with Composition-Matched Molecular "Solders": Approaching Single Crystal Mobility". In: *Nano Letters* 15.10 (2015), pp. 6309–6317.

[21] Xiangfeng Duan, Chunming Niu, Vijendra Sahi, Jian Chen, J. Wallace Parce, Stephen Empedocles, and Jay L. Goldman. "High-performance thin-film transistors using semiconductor nanowires and nanoribbons". In: *Nature* 425.6955 (2003), p. 274. ISSN: 1476-46871476-4687.

[22] Andras G. Pattantyus-Abraham, Illan J. Kramer, Aaron R. Barkhouse, Xihua Wang, Gerasimos Konstantatos, Ratan Debnath, Larissa Levina, Ines Raabe, Mohammad K. Nazeeruddin, Michael Grätzel, and Edward H. Sargent. "Depleted-Heterojunction Colloidal Quantum Dot Solar Cells". In: *ACS Nano* 4.6 (2010), pp. 3374–3380.

[23] Michael A Boles, Daishun Ling, Taeghwan Hyeon, and Dmitri V Talapin. "The surface science of nanocrystals". In: *Nature Materials* 15.2 (Feb. 2016), pp. 141–153. ISSN: 1476-1122.

[24] Y. C. Cheng, G. S. Engel, and G. R. Fleming. "Elucidation of population and coherence dynamics using cross-peaks in two-dimensional electronic spectroscopy". In: *Chemical Physics* 341.1-3 (2007), pp. 285–295. ISSN: 0301-0104.

[25] J. D. Hybl, A. A. Ferro, and D. M. Jonas. "Two-dimensional Fourier transform electronic spectroscopy". In: *Journal of Chemical Physics* 115.14 (2001), pp. 6606–6622. ISSN: 0021-9606.

[26] T. Brixner, T. Mancal, I. V. Stiopkin, and G. R. Fleming. "Phase-stabilized two-dimensional electronic spectroscopy". In: *Journal of Chemical Physics* 121.9 (2004), pp. 4221–4236. ISSN: 0021-9606.

[27] Y. C. Cheng and G. R. Fleming. "Dynamics of Light Harvesting in Photosynthesis". In: *Annual Review of Physical Chemistry*. Vol. 60. Annual Review of Physical Chemistry. 2009, pp. 241–262. ISBN: 978-0-8243-1060-8.

[28] G. D. Scholes, G. R. Fleming, A. Olaya-Castro, and R. van Grondelle. "Lessons from nature about solar light harvesting". In: *Nature Chemistry* 3.10 (2011), pp. 763–774. ISSN: 1755-4330.

[29] J. R. Caram, H. B. Zheng, P. D. Dahlberg, B. S. Rolczynski, G. B. Griffin, D. S. Dolzhnikov, D. V. Talapin, and G. S. Engel. "Exploring size and state dynamics in CdSe quantum dots using two-dimensional electronic spectroscopy". In: *Journal of Chemical Physics* 140.8 (2014). ISSN: 0021-9606.

[30] Gregory S. Engel, Tessa R. Calhoun, Elizabeth L. Read, Tae-Kyu Ahn, Tomáš Mančal, Yuan-Chung Cheng, Robert E. Blankenship, and Graham R. Fleming. "Evidence for wavelike energy transfer through quantum coherence in photosynthetic systems". In: *Nature* 446.7137 (2007), p. 782. ISSN: 1476-46871476-4687.

[31] Y. C. Cheng and G. R. Fleming. "Coherence quantum beats in two-dimensional electronic spectroscopy". In: *Journal of Physical Chemistry A* 112.18 (2008), pp. 4254–4260. ISSN: 1089-5639.

[32] Minhaeng Cho. "Coherent Two-Dimensional Optical Spectroscopy". In: *Chemical Reviews* 108.4 (2008), pp. 1331–1418.

[33] David M. Jonas. "Two-Dimensional Femtosecond Spectroscopy". In: *Annual Reviews* 54 (2003), pp. 425–463.

[34] T. A. A. Oliver. "Recent advances in multidimensional ultrafast spectroscopy". In: *R Soc Open Sci*. Vol. 5. 2018. ISBN: 2054-5703 (Electronic).

[35] Changhee Lee, Jaehoon Lim, Jeonghun Kwak, Kookheon Char, Seonghoon Lee, and Wan Ki Bae. "Perspective on synthesis, device structures, and printing processes for quantum dot displays". In: *Optical Materials Express, Vol. 2, Issue 5, pp. 594-628* (2012).

[36] X. L. Dai, Y. Z. Deng, X. G. Peng, and Y. Z. Jin. "Quantum-Dot Light-Emitting Diodes for Large-Area Displays: Towards the Dawn of Commercialization". In: *Advanced Materials* 29.14 (2017). ISSN: 0935-9648.

[37] L. Protesescu, S. Yakunin, M. I. Bodnarchuk, F. Krieg, R. Caputo, C. H. Hendon, R. X. Yang, A. Walsh, and M. V. Kovalenko. "Nanocrystals of Cesium Lead Halide Perovskites (CsPbX3, X = Cl, Br, and I): Novel Optoelectronic Materials Showing Bright Emission with Wide Color Gamut". In: *Nano Letters* 15.6 (2015), pp. 3692–3696. ISSN: 1530-6984.

[38] J. S. Manser, J. A. Christians, and P. V. Kamat. "Intriguing Optoelectronic Properties of Metal Halide Perovskites". In: *Chemical Reviews* 116.21 (2016), pp. 12956–13008. ISSN: 0009-2665.

[39] S. Kim, T. Kim, M. Kang, S. K. Kwak, T. W. Yoo, L. S. Park, I. Yang, S. Hwang, J. E. Lee, S. K. Kim, and S. W. Kim. "Highly Luminescent InP/GaP/ZnS Nanocrystals and Their Application to White Light-Emitting Diodes". In: *Journal of the American Chemical Society* 134.8 (2012), pp. 3804–3809. ISSN: 0002-7863.

[40] J. Cui, A. P. Beyler, L. F. Marshall, O. Chen, D. K. Harris, D. D. Wanger, X. Brokmann, and M. G. Bawendi. "Direct probe of spectral inhomogeneity reveals syn-

thetic tunability of single-nanocrystal spectral linewidths". In: *Nature Chemistry* 5.7 (2013), pp. 602–606. ISSN: 1755-4330.

[41] V. Chandrasekaran, M. D. Tessier, D. Dupont, P. Geiregat, Z. Hens, and E. Brainis. "Nearly Blinking-Free, High-Purity Single-Photon Emission by Colloidal InP/ZnSe Quantum Dots". In: *Nano Letters* 17.10 (2017), pp. 6104–6109. ISSN: 1530-6984.

[42] D. V. Talapin, S. Haubold, A. L. Rogach, A. Kornowski, M. Haase, and H. Weller. "A novel organometallic synthesis of highly luminescent CdTe nanocrystals". In: *Journal of Physical Chemistry B* 105.12 (2001), pp. 2260–2263. ISSN: 1520-6106.

[43] V. D'Innocenzo, G. Grancini, M. J. P. Alcocer, A. R. S. Kandada, S. D. Stranks, M. M. Lee, G. Lanzani, H. J. Snaith, and A. Petrozza. "Excitons versus free charges in organo-lead tri-halide perovskites". In: *Nature Communications* 5 (2014). ISSN: 2041-1723.

[44] A. Marchioro, J. Teuscher, D. Friedrich, M. Kunst, R. van de Krol, T. Moehl, M. Gratzel, and J. E. Moser. "Unravelling the mechanism of photoinduced charge transfer processes in lead iodide perovskite solar cells". In: *Nature Photonics* 8.3 (2014), pp. 250–255. ISSN: 1749-4885.

[45] C. S. Ponseca, T. J. Savenije, M. Abdellah, K. B. Zheng, A. Yartsev, T. Pascher, T. Harlang, P. Chabera, T. Pullerits, A. Stepanov, J. P. Wolf, and V. Sundstrom. "Organometal Halide Perovskite Solar Cell Materials Rationalized: Ultrafast Charge Generation, High and Microsecond-Long Balanced Mobilities, and Slow Recombination". In: *Journal of the American Chemical Society* 136.14 (2014), pp. 5189–5192. ISSN: 0002-7863.

[46] G. C. Xing, N. Mathews, S. Y. Sun, S. S. Lim, Y. M. Lam, M. Gratzel, S. Mhaisalkar, and T. C. Sum. "Long-Range Balanced Electron- and Hole-Transport Lengths in Organic-Inorganic $CH_3NH_3PbI_3$". In: *Science* 342.6156 (2013), pp. 344–347. ISSN: 0036-8075.

[47] S. D. Stranks, G. E. Eperon, G. Grancini, C. Menelaou, M. J. P. Alcocer, T. Leijtens, L. M. Herz, A. Petrozza, and H. J. Snaith. "Electron-Hole Diffusion Lengths Exceeding 1 Micrometer in an Organometal Trihalide Perovskite Absorber". In: *Science* 342.6156 (2013), pp. 341–344. ISSN: 0036-8075.

[48] F. Deschler, M. Price, S. Pathak, L. E. Klintberg, D. D. Jarausch, R. Higler, S. Huttner, T. Leijtens, S. D. Stranks, H. J. Snaith, M. Atature, R. T. Phillips, and R. H. Friend. "High Photoluminescence Efficiency and Optically Pumped Lasing in Solution-Processed Mixed Halide Perovskite Semiconductors". In: *Journal of Physical Chemistry Letters* 5.8 (2014), pp. 1421–1426. ISSN: 1948-7185.

[49] B. Chen, Y. Bai, Z. S. Yu, T. Li, X. P. Zheng, Q. F. Dong, L. Shen, M. Boccard, A. Gruverman, Z. Holman, and J. S. Huang. "Efficient Semitransparent Perovskite Solar Cells for 23.0%-Efficiency Perovskite/Silicon Four-Terminal Tandem Cells". In: *Advanced Energy Materials* 6.19 (2016). ISSN: 1614-6832.

[50] D. Q. Bi, C. Y. Yi, J. S. Luo, J. D. Decoppet, F. Zhang, S. M. Zakeeruddin, X. Li, A. Hagfeldt, and M. Gratzel. "Polymer-templated nucleation and crystal growth of perovskite films for solar cells with efficiency greater than 21%". In: *Nature Energy* 1 (2016). ISSN: 2058-7546.

[51] H. P. Zhou, Q. Chen, G. Li, S. Luo, T. B. Song, H. S. Duan, Z. R. Hong, J. B. You, Y. S. Liu, and Y. Yang. "Interface engineering of highly efficient perovskite solar cells". In: *Science* 345.6196 (2014), pp. 542–546. ISSN: 0036-8075.

[52] W. S. Yang, J. H. Noh, N. J. Jeon, Y. C. Kim, S. Ryu, J. Seo, and S. I. Seok. "High-performance photovoltaic perovskite layers fabricated through intramolecular exchange". In: *Science* 348.6240 (2015), pp. 1234–1237. ISSN: 0036-8075.

[53] W. Y. Nie, H. H. Tsai, R. Asadpour, J. C. Blancon, A. J. Neukirch, G. Gupta, J. J. Crochet, M. Chhowalla, S. Tretiak, M. A. Alam, H. L. Wang, and A. D. Mohite.

"High-efficiency solution-processed perovskite solar cells with millimeter-scale grains". In: *Science* 347.6221 (2015), pp. 522–525. ISSN: 0036-8075.

[54] S. Yakunin, L. Protesescu, F. Krieg, M. I. Bodnarchuk, G. Nedelcu, M. Humer, G. De Luca, M. Fiebig, W. Heiss, and M. V. Kovalenko. "Low-threshold amplified spontaneous emission and lasing from colloidal nanocrystals of caesium lead halide perovskites". In: *Nature Communications* 6 (2015). ISSN: 2041-1723.

[55] F. Zhang, H. Z. Zhong, C. Chen, X. G. Wu, X. M. Hu, H. L. Huang, J. B. Han, B. S. Zou, and Y. P. Dong. "Brightly Luminescent and Color-Tunable Colloidal $CH_3NH_3PbX_3$ (X = Br, I, Cl) Quantum Dots: Potential Alternatives for Display Technology". In: *Acs Nano* 9.4 (2015), pp. 4533–4542. ISSN: 1936-0851.

[56] S. B. Sun, D. Yuan, Y. Xu, A. F. Wang, and Z. T. Deng. "Ligand-Mediated Synthesis of Shape-Controlled Cesium Lead Halide Perovskite Nanocrystals via Reprecipitation Process at Room Temperature". In: *Acs Nano* 10.3 (2016), pp. 3648–3657. ISSN: 1936-0851.

[57] H. L. Huang, F. C. Zhao, L. G. Liu, F. Zhang, X. G. Wu, L. J. Shi, B. S. Zou, Q. B. Pei, and H. Z. Zhong. "Emulsion Synthesis of Size-Tunable $CH_3NH_3PbBr_3$ Quantum Dots: An Alternative Route toward Efficient Light-Emitting Diodes". In: *Acs Applied Materials & Interfaces* 7.51 (2015), pp. 28128–28133. ISSN: 1944-8244.

[58] Y. Bekenstein, B. A. Koscher, S. W. Eaton, P. D. Yang, and A. P. Alivisatos. "Highly Luminescent Colloidal Nanoplates of Perovskite Cesium Lead Halide and Their Oriented Assemblies". In: *Journal of the American Chemical Society* 137.51 (2015), pp. 16008–16011. ISSN: 0002-7863.

[59] G. Nedelcu, L. Protesescu, S. Yakunin, M. I. Bodnarchuk, M. J. Grotevent, and M. V. Kovalenko. "Fast Anion-Exchange in Highly Luminescent Nanocrystals of Cesium Lead Halide Perovskites ($CsPbX_3$, X = Cl, Br, I)". In: *Nano Letters* 15.8 (2015), pp. 5635–5640. ISSN: 1530-6984.

[60] D. M. Jang, K. Park, D. H. Kim, J. Park, F. Shojaei, H. S. Kang, J. P. Ahn, J. W. Lee, and J. K. Song. "Reversible Halide Exchange Reaction of Organometal Trihalide Perovskite Colloidal Nanocrystals for Full-Range Band Gap Tuning". In: *Nano Letters* 15.8 (2015), pp. 5191–5199. ISSN: 1530-6984.

[61] I. Lignos, S. Stavrakis, G. Nedelcu, L. Protesescu, A. J. Demello, and M. V. Kovalenko. "Synthesis of Cesium Lead Halide Perovskite Nanocrystals in a Droplet-Based Microfluidic Platform: Fast Parametric Space Mapping". In: *Nano Letters* 16.3 (2016), pp. 1869–1877. ISSN: 1530-6984.

[62] Y. Q. Xu, Q. Chen, C. F. Zhang, R. Wang, H. Wu, X. Y. Zhang, G. C. Xing, W. W. Yu, X. Y. Wang, Y. Zhang, and M. Xiao. "Two-Photon-Pumped Perovskite Semiconductor Nanocrystal Lasers". In: *Journal of the American Chemical Society* 138.11 (2016), pp. 3761–3768. ISSN: 0002-7863.

[63] Sandrine Ithurria and Benoit Dubertret. "Quasi 2D Colloidal CdSe Platelets with Thicknesses Controlled at the Atomic Level". In: *Journal of the American Chemical Society* 130.49 (2008), pp. 16504–+. ISSN: 0002-7863.

[64] Yijie Yang, Chaojian Zhang, Xiangwei Qu, Wenda Zhang, Mikita Marus, Bing Xu, Kai Wang, and Xiaowei Sun. "High quantum yield colloidal semiconducting nanoplatelets and high color purity nanoplatelet QLED". In: *IEEE Transactions on Nanotechnology* (2019), pp. 1–1. ISSN: 1536-125X.

[65] Sandrine Ithurria and Dmitri V Talapin. "Colloidal Atomic Layer Deposition (c-ALD) using Self-Limiting Reactions at Nanocrystal Surface Coupled to Phase Transfer between Polar and Nonpolar Media". In: *Journal of the American Chemical Society* 134.45 (Nov. 2012), pp. 18585–18590. ISSN: 0002-7863.

[66] Cecile Bouet, Benoit Mahler, Brice Nadal, Benjamin Abecassis, Mickael D Tessier, Sandrine Ithurria, Xiangzhen Xu, and Benoit Dubertret. "Two-Dimensional Growth

of CdSe Nanocrystals, from Nanoplatelets to Nanosheets". In: *Chemistry of Materials* 25.4 (2013), pp. 639–645. ISSN: 0897-4756.

[67] Benoit Mahler, Brice Nadal, Cecile Bouet, Gilles Patriarche, and Benoit Dubertret. "Core/Shell Colloidal Semiconductor Nanoplatelets". In: *Journal of the American Chemical Society* 134.45 (2012), pp. 18591–18598. ISSN: 0002-7863.

[68] Mickaël D. Tessier, Piernicola Spinicelli, Dorian Dupont, Gilles Patriarche, Sandrine Ithurria, and Benoit Dubertret. "Efficient Exciton Concentrators Built from Colloidal Core/Crown CdSe/CdS Semiconductor Nanoplatelets". In: *Nano Letters* 14.1 (Jan. 2014), pp. 207–213. ISSN: 1530-6984.

[69] Wooje Cho, Siyoung Kim, Igor Coropceanu, Vishwas Srivastava, Benjamin T. Diroll, Abhijit Hazarika, Igor Fedin, Giulia Galli, Richard D. Schaller, and Dmitri V. Talapin. "Direct Synthesis of Six-Monolayer (1.9 nm) Thick Zinc-Blende CdSe Nanoplatelets Emitting at 585 nm". In: *Chemistry of Materials* 30.20 (Oct. 2018), pp. 6957–6960. ISSN: 0897-4756.

CHAPTER 2

BACKGROUND

2.1 Electronic Structure of Semiconductors

A band structure is a plot of the allowed energies of a solid's electrons and can be used to determine the optoelectronic or magnetic properties of the bulk system. This thesis will focus on semiconductors, which are solid materials with a characteristic gap between the highest occupied (valence) and lowest unoccupied (conduction) bands. In a semiconductor, an electron in the valence band can be optically or electrically excited into the conduction band, leaving behind a positively charged hole, both of which are free to move in the crystal.[1] These free carriers can then be practically exploited to make amplifiers, switches, and energy conversion devices. This section will provide an overview of semiconductor band theory and discuss the nanocrystalline electronic structure that emerges when a macroscopic crystal is truncated to a few thousand atoms.

2.1.1 Band Structure Introduction

In an atomic system, the electronic structure is characterized by a set of discrete energy levels, and when two atoms are brought close enough together that their wavefunctions begin to overlap, the individual atomic states split into bonding, non-bonding, and anti-bonding molecular orbitals. In a solid material, many ($\sim 10^{23}$) atoms are bound together, forming a set of quantum states that are so closely spaced they can be considered continuous bands. These bands describe the energy of the electrons in the system as a function of the wavevector, $\vec{k}$, which is related to the phase of the electronic wavefunction in a given crystal dimension. For example, consider a chain of H atoms with interatomic distance, a. One possibility is that the phase of the wavefunction does not change at different lattice points, corresponding to $\vec{k} = 0$, which is referred to as the Γ point. For the H atom 1s orbitals, this is the lowest energy configuration, however, for a 2px orbital, it is the highest energy

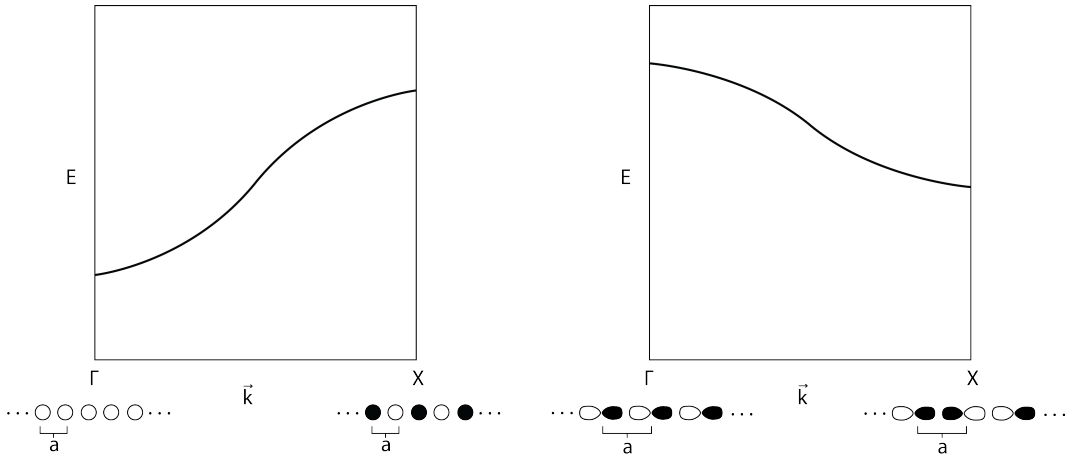

Figure 2.1: Bands are formed in extended solids by continuously varying the phase of the electronic wavefunction across the periodic lattice. This figure shows two examples of how an infinite linear chain of molecular orbitals can form continuous band structures. Left: 1s orbitals in a linear arrangement have an energy minimum at the Γ point where the phase is the same for all orbitals in the chain. The maximum energy is obtained by alternating the phase of the wavefunction at each lattice point, which is represented by $\vec{k} = X$. Right: Conversely for $2p_x$ orbitals, the highest energy occurs at the Γ point and the lowest energy is at the X point. The $2p_x$ orbital band has shallower curvature due to higher delocalization of the wavefunction.[2]

configuration. The converse is true for $\vec{k} = \pi/a$ (X), where the phase of the wavefunction changes at each lattice position. At these points of symmetry, the electronic wavefunctions form standing waves and have two allowed energies, the energy difference between these solutions is known as a bandgap. Since $\vec{k}$ can take on any value, the 1s and 2px bands of this H atom chain would have the structure shown in Figure 2.1. Finally, note that the dispersion for the 1s band is much higher than the 2px band, indicating that the carrier mobility in the 2px band is higher owing to the greater degree of delocalization compared to a 1s band.[2]

Bands are filled following a Fermi-Dirac distribution (eq. 2.1), and the energy at which there is an equal probability of a state being filled or not at a given temperature is known as the Fermi energy, E_f.

$$f(E_f) = \frac{1}{1 + e^{(E_f - \mu)/k_b T}} \tag{2.1}$$

Here μ is the total chemical potential of the system, T is the temperature, and k_b is

the Boltzmann constant. Using this formula, the fermi energy occurs at $E_f = \mu$ since the distribution is $f(E_f) = \frac{1}{2}$, giving an equal probability of a state at that energy being filled and unfilled. The band directly below the Fermi energy is called the valence band, and the band directly above this level is known as the conduction band. Different types of materials such as metals, insulators, and semiconductors are segmented by the value of the bandgap between the valence and conduction bands. In metals, the Fermi energy is an allowed energy of the system, the bandgap is negative, and electrons are free to flow in the conduction band at room temperature. While semiconductors and insulators have positive bandgaps such that conduction band electrons can only be created with help from an external energy source. Insulators have bandgaps that are too large to overcome by typical excitations (<10 eV), while semiconductors have small bandgaps (∼2 eV or less) and electrons can be promoted to the conduction band relatively easily by, for instance heating or solar illumination.[1]

Band structure diagrams concisely represent the electronic structure of a solid material by plotting each of the bands (or a subset close to the Fermi energy) and their dispersion curves between important points of symmetry in k-space. Figure 2.2 shows a calculated band structure of InP, which is a direct gap semiconductor with the highest energy point of the valence band at the same point in k-space as the lowest energy point of the conduction band. Semiconductors that have an offset between the maximum and minimum of the valence and conduction bands are known as indirect gap semiconductors, of which Silicon is the most common example. The k-axis is labelled by symbols that denote important points of symmetry for the unit cell's geometry, while the interior labels refer to the irreducible representation of the wavefunction at each symmetry point.[3]

2.1.2 Semiconductor Carrier Dynamics

When optical light is incident on a semiconductor, various physical processes can occur. A portion of the incident light wil be reflected at the surface of the crystal and the rest will be transmitted. Inside the crystal the radiation can then be either absorbed or scattered. Ab-

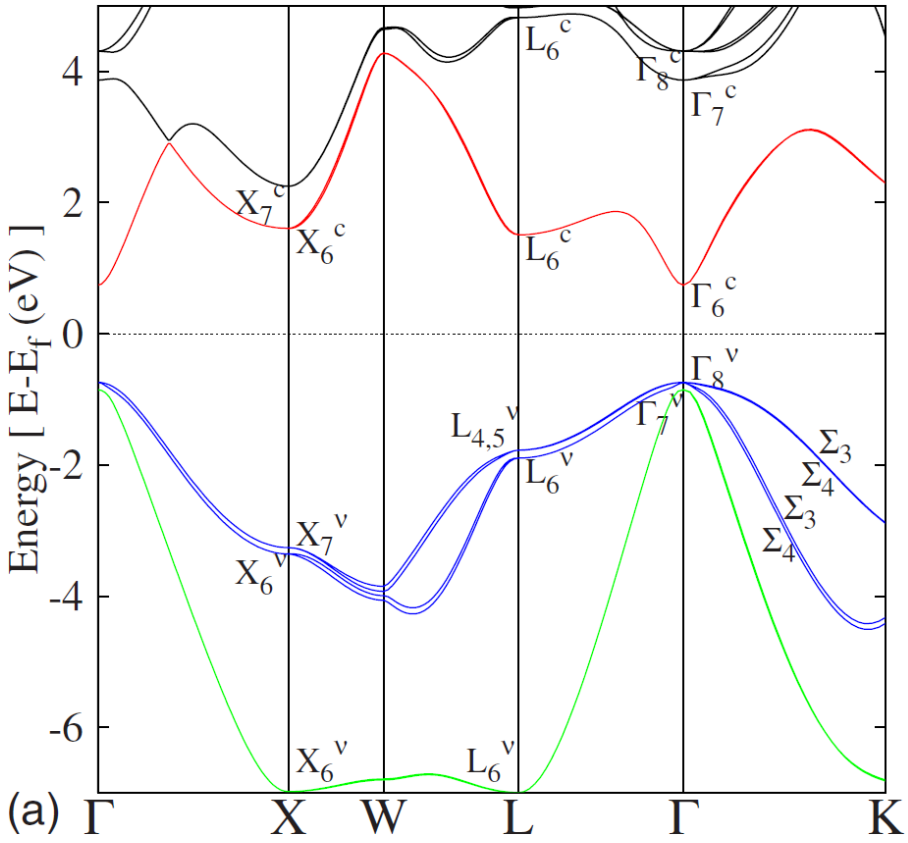

Figure 2.2: Calculated band structure of bulk InP. Here various points of high symmetry are denoted on the horizontal axis and the band dispersion between these symmetry points is plotted vs. the energy relative to the Fermi level (E_f). The symbols on the interior of the plot refer to the irreducible representations of the wavefunction for each allowed solution at every symmetry point with Σ denoting the path between Γ and L. InP is a direct gap semiconductor with the lowest-lying transition occuring between the Γ_8^v valence band and the Γ_6^c conduction band. The Γ_8^v band is four-fold degenerate at the Γ point, breaking into two heavy hole and two light hole bands further from the symmetry point. Importantly, the energy difference between the Γ, L, and X valleys in the lowest lying conduction band is relatively small <1 eV, allowing phonon-mediated transport between these three minima at room temperature, which acts as the basis of microwave emitters like Gunn diodes. Reprinted figure with permission from [Yoon-Suk Kim, Kerstin Hummer, and Georg Kresse, Accurate band structures and effective masses for InP, InAs, and InSb using hybrid functionals, Phys. Rev. B 80, 035203-5, 2009.] Copyright 2009 by the American Physical Society.

sorption can occur if the frequency of the light is greater than the bandgap energy necessary to excite charge carriers from the valence band to the conduction band. These charge carriers can then relax via scattering and produce heat, or they can recombine and photoluminesce (Figure 2.3). If the incident light is at an energy greater than the bandgap, the free carriers will typically relax to the band edge faster than the photoluminescence lifetime, and the emitted light will be at the bandgap frequency, no matter what incident frequency was used. In bulk semiconductors, the electron and hole states have very weak Coulomb coupling due to the large dielectric screening from the valence electrons. However, particularly in confined systems or in bulk materials at low temperatures, bound electron-hole pairs called excitons can be formed by absorption of incident light at energies slightly redder than the bandgap (corresponding to the exciton binding energy) or relaxation from free carriers to these bound states. Excitonic states can also be emissive but will have notably different decay dynamics than free carriers since excitons will undergo one-particle recombination rather than the typical two-body free carrier recombination. Additionally, the dynamics of both excitons and free carriers can be greatly impacted by either acoustic or optical modes of the crystal lattice. Rather than emit light, charge carriers can also recombine non-radiatively via either trap-assisted recombination, or a three-body Auger process where an electron recombines with a hole, driving another excited electron in the conduction band into a higher energy state. In most applications, the loss in quantum efficiency due to these non-radiative pathways, both for bulk and confined systems are undesirable and efforts to engineer semiconductor devices attempt to control or limit the impact of Auger recombination or mid-gap trap states that arise from defects either in the crystal lattice or on the surface of the crystal.[4]

Defects can arise from a variety of sources, but they are capable of profoundly impacting the behavior of a semiconducting material. For example, introducing phosphorus or boron atoms into a perfect Silicon lattice will increase the number of electrons or holes present in the system, which in turn raises or lowers the Fermi energy and impacts the conductivity of the material. This behavior has been used to great effect by engineering defect sites

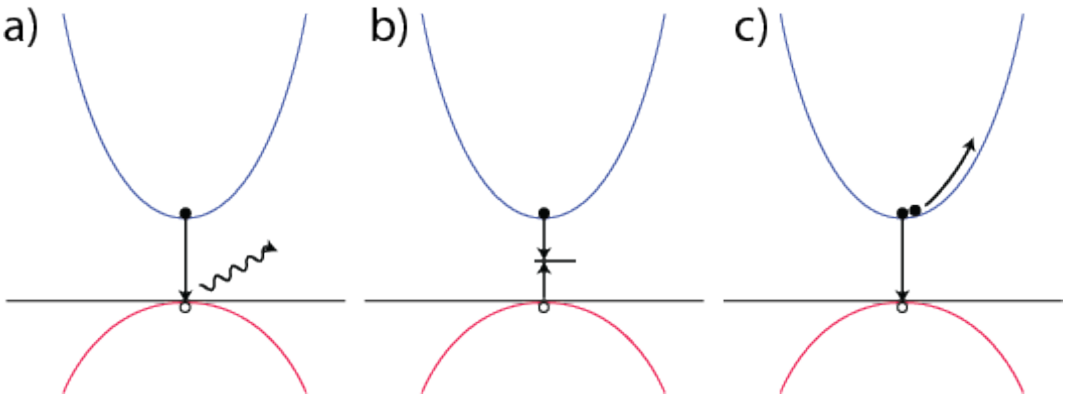

Figure 2.3: Dominant charge carrier recombination pathways in semiconductors. After forming electrons and holes upon optical or electrical excitation the system can undergo different types of relaxation a) the excited electron and hole may recombine radiatively after both relax to the band edge producing photoluminescence. b) The electron or hole may relax to mid-gap trap states before recombination typically resulting in dissapation of energy via heat. c) An electron in the conduction band can recombine with a hole in the valence band causing another conduction band electron to be excited to a hot carrier state, which will then relax back down to the band edge. This three-body process is known as Auger recombination.

purposefully to create modern diodes and transistors. However, point defects like atomic vacancies can alter the performance of the system in undesirable ways by acting as sinks for free charge carriers and for example, decreasing the photoluminescence quantum yield in an LED or the conversion efficiency of a solar cell.[4]

2.1.3 Confined Semiconductors

The band structure theory presented in the previous sections holds true for a defect-free, infinite, periodic lattice. If the semiconductor crystal is truncated so that infinitely large potential barriers separated by length L exist and can reflect the electronic wavefunctions, the semiconductor is said to be spatially confined. For an electron with effective mass m* confined in one dimension with infinite potential barriers a distance L apart, the solutions to the Schrödinger equation are identical to a particle in a one-dimensional box:

$$E_n = \frac{\hbar^2}{2m}(kz^2 + kx^2 + ky^2) = \frac{\hbar^2}{2m}(\frac{n^2\pi^2}{L^2} + kx^2 + ky^2) \tag{2.2}$$

Since in this case confinement only occurs in one dimension, the electrons can move about the unconfined 2D plane as if they were free particles. In the confined dimension, the discrete energy levels that emerge are dependent on the inverse square of L, so that the smaller L becomes, the larger the confinement energy, causing optical transitions to blueshift in response to shrinking size. If L is small enough that it is on the order of the exciton Bohr radius, the exciton binding energy increases due to confinement and excitonic spectral features become much more prominent than in the bulk case as a result. If the semiconductor is confined in all three dimensions, which is the case for a quantum dot, then equation 1.3 reduces to:

$$E_n = \frac{\hbar^2 n^2}{8mL^2} \tag{2.3}$$

Therefore, in all dimensions the band-like semiconductor electronic structure gives way to discrete states that resemble an atomic system. In realistic quantum dots the potential is not a square potential like in a quantum well but is spherically symmetric. Applying this barrier potential to the Schrödinger equation gives wavefunctions that are products of the spherical Bessel functions and the spherical harmonic functions:

$$\Phi_{n,L,m}(r,\theta,\varphi) = \frac{\sqrt{2}}{R^3}\frac{j_L(\phi_{n,L}\, r/R)}{j_{L+1}(\phi_{n,L})}Y_{L,m}(\theta,\varphi) \tag{2.4}$$

where r, θ, and φ are the radial, angular, and azimuthal spherical coordinates respectively. The values for n, L, and M are the quantum numbers of the system, similar to hydrogenic solutions to the Schrödinger equation and represented by the letters (S, P, D, F, ... for different values of L). Finally, $\phi_{n,L}$ is the nth root of the spherical Bessel function of the Lth order.[5] For these solutions, the energies of the system are given by:

$$E_{nL} = \frac{\hbar^2 \phi_{nL}^2}{2mR^2} \tag{2.5}$$

where m is the particle mass representing the effective mass of either the electron or hole.

The bandgap in QDs is the value of the energy gap between the values of E_nL for the band edge electron and hole states.

$$E_g = E_{g,0} + \frac{\hbar^2\pi^2}{2m_{eh}R^2} \tag{2.6}$$

Where m_{eh} is the reduced mass for the electron and hole $m_{eh} = m_e * m_h/(m_e + m_h)$ and $\phi_{n,L}$ reduces to π for $n = 1, L = 0$. An additional correction is often used in the strong confinement regime that is related to the Coulomb interaction of the electron and hole wavefunctions giving an energy gap of:

$$E_g = E_{g,0} + \frac{\hbar^2\pi^2}{2m_{eh}R^2} - \frac{1.765e^2}{\epsilon R^2} \tag{2.7}$$

where ϵ is the dielectric constant and e is the electric charge constant.[5, 6] In quantum dot materials, particularly the colloidal nanocrystals explored in this thesis, the dielectric constant of the semiconductor material is significantly higher than the surrounding environment. This causes reduced dielectric screening in the quantum dot, greatly enhancing the Coulomb interaction compared to the bulk material in addition to the increased interaction due to confinement. The large carrier-carrier interactions in turn lead to very interesting dynamical phenomena including an increased rate of Auger recombination, which detrimentially affects the performance of most quantum dot devices since energy is lost to the formation of a hot exciton, which relaxes through thermal processes. Alternatively, the strong carrier coupling allows for efficient carrier multiplication, generating remarkable internal quantum efficiencies that form the basis of many quantum dot applications.[7]

2.1.4 Colloidal Nanocrystals

In this thesis I explore nanocrystalline materials that are synthesized via wet chemistry, forming colloidal suspensions of semiconductor crystals that are on the order of 1 – 10 nm in radius. In these materials the size of the electronic wavefunction is determined by the

physical size of the system, which over three decades of research has been refined to near atomic precision.[8, 9] The size of the particles is be controlled by carefully manipulating the temperature and time at which the reaction proceeds. The inherent imprecision in this technique produces an ensemble of nanocrystals that have slight variations in size. This size variation manifests itself as inhomogeneously broadened absorption and emission spectra since each nanocrystal has a slightly different size-dependent band gap.[9, 10] However, synthetic techniques have improved to the point that well understood materials like CdSe quantum dots can be tuned very precisely and produce narrow spectra ($\sim$10 nm).[11, 12] Due to their colloidal nature, nanomaterials created synthetically must be capped by ligands to prevent aggregation in solution. Typically, these ligands are long-chain acids like oleic acid but can also be short chalcogenide ligands.[13] Manipulating the nanocrystal surface via ligand exchange or etching techniques are very important to many applications. For example, drug delivery, chemical sensing, and catalytic applications rely on highly engineered ligand environments and take advantage of the nanocrystal's high surface area/volume ratio. In addition to size control and surface modification, colloidal nanocrystals can be tuned further by creating non-spherical particles such as quantum rods,[14] core-shell heterostructures,[15] 2D nanoplatelets,[16] and more. Finally, it is possible to create hybrid materials that involve a core nanomaterial that is coated in another semiconductor with similar lattice constants but a different bandgap. A common example of this type of core-shell material is the CdSe/CdS quantum dot. The band gap of CdSe in bulk is 1.74 eV, while the gap in CdS is wider at 2.42 eV. The shelling process passivates potential surface traps on the CdSe layer to increase the photoluminescence quantum yield, and redshifts the absorption spectrum due to band alignment.

2.2 2D Electronic Spectroscopy

Two-Dimensional Electronic Spectroscopy (2DES) is an ideal technique for studying nanocrystal systems because of its access to both broad spectral resolution and fast time

dynamics.[17, 18] Ultrafast pulses can be used to clock chemical dynamics[19], and using ultrafast techniques like 2DES allows researchers to explore the carrier dynamics of nanomaterials at the sub-100 fs timescale. Learning about the femtosecond dynamics of nanosystems is vital to understanding the underlying physics of how energy flows through the system and how charge carriers couple to one another, to phonon modes of the crystal, and to impurities in the crystal structure.[20–22] Additionally, while the absorption and emission spectra of CdSe quantum dots and nanoplatelets are very sharp and distinct, size inhomogeneity in a nanomaterial ensemble is an important metric for the quality of a synthetic technique. 2DES can quantify the degree of inhomogeneous broadening in a way that related methods like Transient Absorption spectroscopy cannot.[17, 23] Finally, the capacity for 2DES to reveal the coupling between multiple electronic states or between electronic and vibrational states through quantum beating maps is a powerful tool for understanding the electronic structure of any complex system of chromophores.[24–30]

2.2.1 Theory of 2DES

Any optical spectroscopy, including 2DES, involves measuring the macroscopic polarization that is produced by a system in response to an external electric field. This macroscopic polarization is equal to the expectation value of the material dipole moment operator, which can be expressed as the trace of the dipole moment operator acting on the material density matrix. After perturbatively expanding this expression, Eq. 1 is obtained.[31]

$$P(t) = Tr[\mu\rho(t)] = Tr[\mu\rho^{(0)}(t)] + Tr[\mu\rho^{(1)}(t)] + Tr[\mu\rho^{(2)}(t)] + Tr[\mu\rho^{(3)}(t)] + \dots \quad (2.8)$$

The nonlinear optical techniques used in this thesis including 2DES and transient absorption are third-order spectroscopies that probe $P^{(3)}(t)$ using three independent light-matter interactions. $P^{(3)}(t)$ is dependent on the density matrix, whose time dynamics are deter-

mined by the Liouville-Von Neumann equation (Eq. 1.2).[31]

$$\frac{\partial p}{\partial t} = \frac{-i}{\hbar}[H(t), \rho(t)] \tag{2.9}$$

The Hamiltonian in equation 1.2. can be broken into a time independent system Hamiltonian, detailing the electronic structure and couplings between states of the material being studied, and an external time dependent Hamiltonian (Eq. 1.3) that describes the external electric field. In our case E(t) will be a mathematical representation of the ultrafast pulse that encodes the spatial, temporal, and spectral characteristics of the light that will act to perturb the system.[31]

$$H(t) = H_0 + V(t) = H_0 - \mu E(t) \tag{2.10}$$

Combining equations 1.2 and 1.3, the macroscopic polarization can be expressed as follows (Eq. 1.4).

$$P(t) = \int_0^\infty dt_3 \int_0^\infty dt_2 \int_0^\infty dt_1 (R^{(3)}(t_1, t_2, t_3) E_1(t - t_3) E_2(t - t_3 - t_2) E_3(t - t_3 - t_2 - t_1)) \tag{2.11}$$

In this equation, R represents the material response function, which carries all information about the light-matter interactions. The third-order response function can be written as a system of nested commutators between the dipole moment operators for each external field and an element of the density matrix (Eq. 1.5).[31]

$$R^{(3)}(t_3, t_2, t_1) = \frac{i}{\hbar}^3 \Theta(t_1)\Theta(t_2)\Theta(t_3) Tr\{[[[\mu(t_3{+}t_2{+}t_1), \mu(t_2{+}t_1),], \mu(t_1)], \mu(0)]\rho_{gg}\} \tag{2.12}$$

Each term in this commutator represents a particular pathway through which the system can evolve in time. The dipole moment operators will act on either the bra or ket side of the

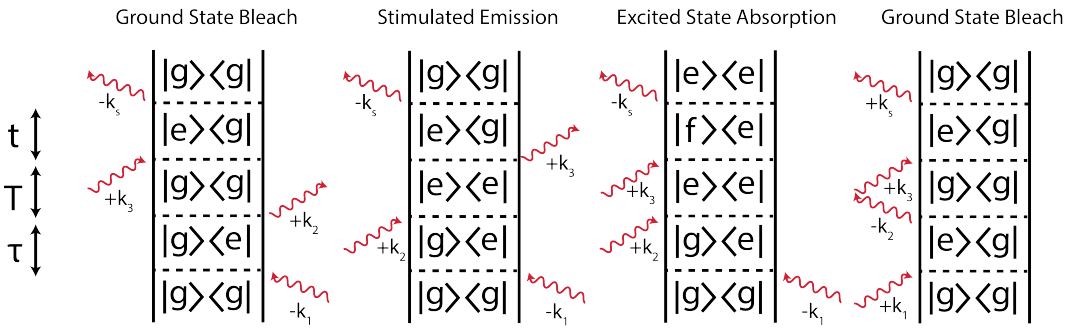

Figure 2.4: Four examples of Feynman diagrams. Each diagram describes the evolution of the density matrix upon interaction with three laser pulses that have defined relative wavevectors. These diagrams are read from the bottom up, representing going forward in time. The first interaction takes the ground population state into a ground-excited state coherence. The second interaction then sends the system into either a ground or excited state population. During the waiting time between the second and third interactions, the system can evolve and relax. After the third interaction, the system is put into another coherence state before emitting a signal E-field. The represented Feynman diagrams depict from left to right: ground state bleach (rephasing), stimulated emission (rephasing), excited state absorption (rephasing), and ground state bleach (non-rephasing).

density matrix element at various time delays. These pathways are commonly represented by Feynman diagrams that represent a possible set of interactions between the system density matrix and the external electric fields.[31] An example Feynman diagram is shown in Figure 2.4.

A Feynman ladder diagram like the one shown in Figure 2.4 consists of two vertical arrows pointing upward and three "rungs" of the ladder represented by horizontal lines. The vertical lines represent time with T = 0 occurring at the first rung of the ladder, while the spaces describe the density matrix element that an interaction puts the system into. Each rung represents a light-matter interaction and can hit on either the left or right (bra or ket) side of the density matrix operator.[31] After the first interaction, the system is driven from a population state or diagonal element of the density matrix into a coherence state (off-diagonal density matrix element). The time between the first and second interactions is therefore known as the coherence time (τ). The second interaction puts the system back into a population state and the time delay between the second and third interaction is the waiting time (T). Finally, the third interaction creates another coherence and the time

between that interaction and detection of the signal polarization is the rephasing time (t). Various nonlinear optical experiments attempt to isolate a set of pathways by controlling the wavevectors of the external electric fields, and hence controlling the side of the ladder diagram on which an interaction happens. There are broadly two types of possible pathways: rephasing and non-rephasing. Rephasing pathways occur when $ks = -k1 + k2 + k3$ while non-rephasing pathways can be collected by setting $ks = k1 - k2 + k3$, or swapping the first and second interactions of a rephasing pathway.[31] A wavevector is considered negative if it interacts incoming on the left side or outgoing on the right side of the ladder, and vice versa for positive wavevectors. By collecting both the rephasing and non-rephasing pathways under identical conditions and combining them, absorptive and dispersive spectra can also be obtained. Techniques like transient absorption spectroscopy make $k1 = k2$, forcing both rephasing and non-rephasing pathways to be emitted in the same direction. These signals constructively interfere and produce absorptive spectra by default. Using a fully collinear pump-probe geometry scheme is possible for 2DES, however the benefits of a background-free detection scheme are lost.[32] Techniques such as phase-cycling can be used to separate rephasing and non-rephasing signals in the pump-probe geometry.[33, 34]

Figure 2.4 depicts various rephasing pathways for a three-level system and places them into three categories: ground state bleach (GSB), stimulated emission (SE), and excited state absorption (ESA). Ground state bleach occurs when the system is taken from the ground state into a coherence, and back to the ground state during the population time. When the system is put into an excited state during the population time, there are two options: the third interaction can either create a ground-excited state coherence (SE) or create a coherence between the excited state and a higher-lying excited state (ESA). By the convention that increased light on the detector is a positive signal, both GSB and SE are defined as positive and ESA is negative. Note that these pathways can occur at the same energies and interfere with each other, occluding analysis of the nonlinear spectrum.

In Figure 2.5, a mock 2D Electronic spectrum is shown that provides examples of what

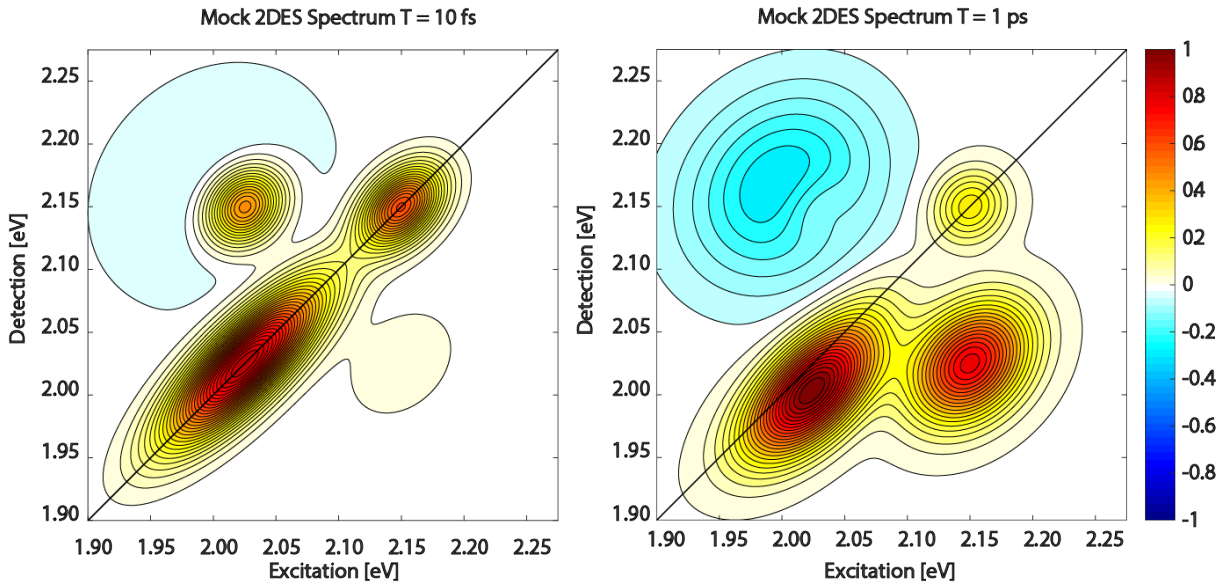

Figure 2.5: Mock 2D spectrum that represents many relevant types of features that are discussed throughout the thesis. A 2D spectrum consists of the excitation axis, which describes at what laser pulse energies the system absorbed energy, and a detection axis that reads out the energies emitted by the system. Common features include diagonal features which can show the homogeneous and inhomogeneous linewidths of each state, off-diagonal features that describe coupling (upper-diagonal) and energy transfer (lower-diagonal) between electronic states, and excited state absorption features that indicate an excited state of the system was pumped into a higher lying excited state.

these types of features look like both at early times and at longer waiting times. Included in this mock spectrum are positive diagonal features that arise from GSB interactions and show varying degrees of inhomogeneous broadening. The redder peak is very inhomogeneously broadened and its lineshape does not significantly round out over time, while the bluer peak is fairly homogeneous and has a rounded out feature as the system is allowed to explore all of the available microstates. Also, the redder band edge feature shifts on the detection energy axis over time which could indicate a phenomenon like a Stokes shift. Energy transfer and coupling peaks can be seen as cross-peaks. The upper-diagonal coupling peak starts strong, and reduces intensity as the system relaxes while the energy transfer peak grows in over time. Finally, excited state absorption features appear as negative peaks in the spectrum indicating excitation from a lower-lying excited state to a higher-lying excited state.

2.2.2 Data Acquisition

The 2D Electronic Spectroscopy system used in the Redfield Lab of the Engel Group consists of three major components: ultrafast pulse generation, white light generation, and the 2D spectrometer itself (Figure 2.6).[35] First, a 5W diode-pumped Nd:YAG continuous wave laser is doubled to 532 nm and used to pump the Ti:Sapphire crystal of a self-mode locking oscillator (Coherent Micra). The oscillator is tuned to yield 50 MHz pulses centered at 800 nm with an average power of ∼500 mW and a typical bandwidth of 60 – 80 nm full width half max (FWHM). The oscillator output is then used to seed a regenerative amplifier (Coherent Legend Elite). Upon entering the amplifier, the pulses from the oscillator are temporally chirped to hundreds of picoseconds by a stretcher grating. Then the pulses are used to seed the amplifier cavity, which is pumped by a 30 W diode-pumped Nd:YLF laser doubled to 532 nm. The amplified laser light is switched by a pair of Pockels cells that act to dump power from the cavity after the pulse has traveled the cavity's Z-fold for a specified number of round-trips (typically 15). After the pulse is ejected from the cavity, it is re-compressed to ∼35 fs, resulting in a 2.8 W final output beam of 5 kHz pulses centered at 805 nm and

35 nm FWHM.

This amplified beam is directed to a 2 m long tube filled with Ar gas pressurized at 13 psi to generate a supercontinuum.[36] The beam is focused into with a 1 m focal length lens and recollimated at the exit. After passing through the tube, the spectrum is broadened to ∼100 nm, with tails extending bluer than 400 nm and redder than 900 nm. For our experiments on semiconductor nanomaterials, light that is redder than 720 nm is blocked by a cold mirror after the Ar tube output for two reasons. First, our samples do not absorb or emit light redder than 720 nm and cutting down the spectrum aids in compression of the bluer light. Also, most of the power is of the beam is in the 800 nm spectral region. Therefore, cutting the spectrum also cuts the power to 150 mW, preventing optical damage in the pulse shaper and unnecessary local heating at the sample position. Next, higher-order dispersion introduced by self-phase modulation in the white light generation process is partially compensated by taking 6 bounces off a pair of chirped mirrors. The output from the chirped mirrors is then sent to a Multiphoton intrapulse interference phase scan (MIIPS) pulse shaper, which can compensate for the dispersion in the rest of the system.[37] The beam exits the MIIPS compressed to ∼8 fs FWHM with a spectrum from 550-700 nm with average power of ∼40 mW and is sent to the spectrometer.

The 2D spectrometer in the Redfield Lab (Figure 2.7) is an all-reflective BOXCARS geometry that utilizes delay stages (Aerotech) to control the timings between pulses.[35, 38] The all-reflective geometery aids in pulse compression by eliminating transmissive optics that can cause differential chirp at different wavelengths in these ultrabroadband pulses, which can lead to artifacts in the cross-peaks of the 2D spectrum.[39] First, the beam is split into two by a 50/50 beamsplitter and these beams are delayed relative to one another by the waiting time stage, which is capable of delays up to 1 ns. These two beams are then split into 4 using another 50/50 beamsplitter and directed to four independent mirrors, two of which (beams 3 and 4) are mounted on micrometers and at 0 deg relative to the incident beam angle, while the other two (beams 1 and 2) are mounted on coherence time delay stages

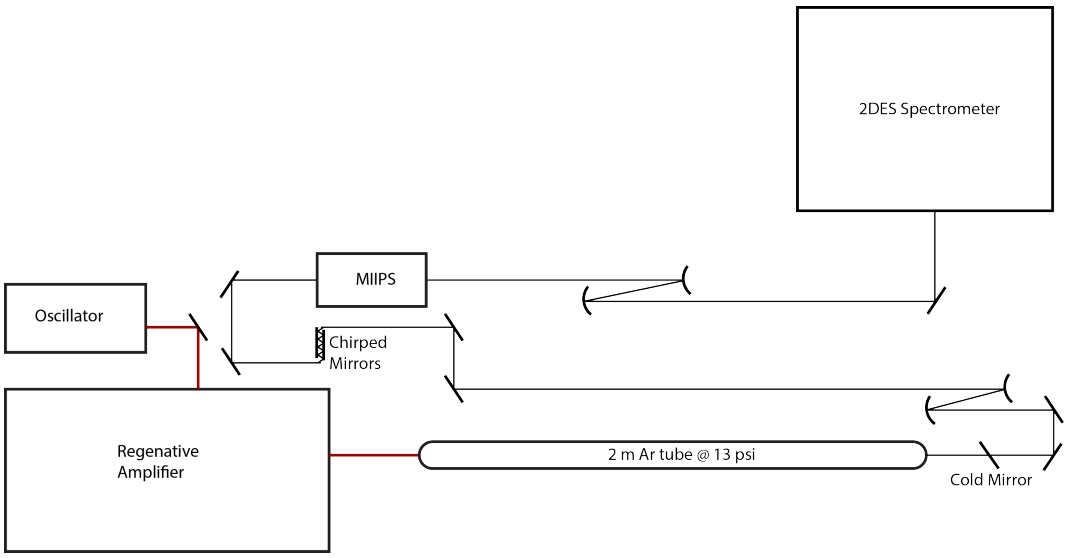

Figure 2.6: The Redfield lab setup consists of four main parts: ultrafast pulse generation from the oscillator and regenerative amplifier, white light generation from the pressurized Ar tube, pulse compression optics from the chirped mirrors and MIIPS, and finally the 2D spectrometer.

and horizontally tilted to create a relative time delay as the stages are scanned. After all of the relative pulse delays are set, the beams are overlapped at the sample cell, which is placed in the focus of an off-axis parabolic mirror pair. A physical mask is used to block beams 1, 2, and 3 after the sample, while the signal and local oscillator are collimated and focused into a spectrometer (Andor Shamrock) where the signal interferogram is spectrally dispersed and sent to a camera (Newton), which records the heterodyned signal. In a typical experiment, for each waiting time point (T), the coherence time delay (tau) is scanned from -90 fs to +90 fs in 1.5 fs steps to capture both the rephasing and non-rephasing signals. Additionally, three reference scans are collected at each waiting time by blocking various beams: (1) blocking beam 3 (2) blocking beams 1 and 2 and (3) blocking beams 1, 2, and 3. These reference scans are used to subtract static scatter that travels in the phase-matched direction with the signal and LO.

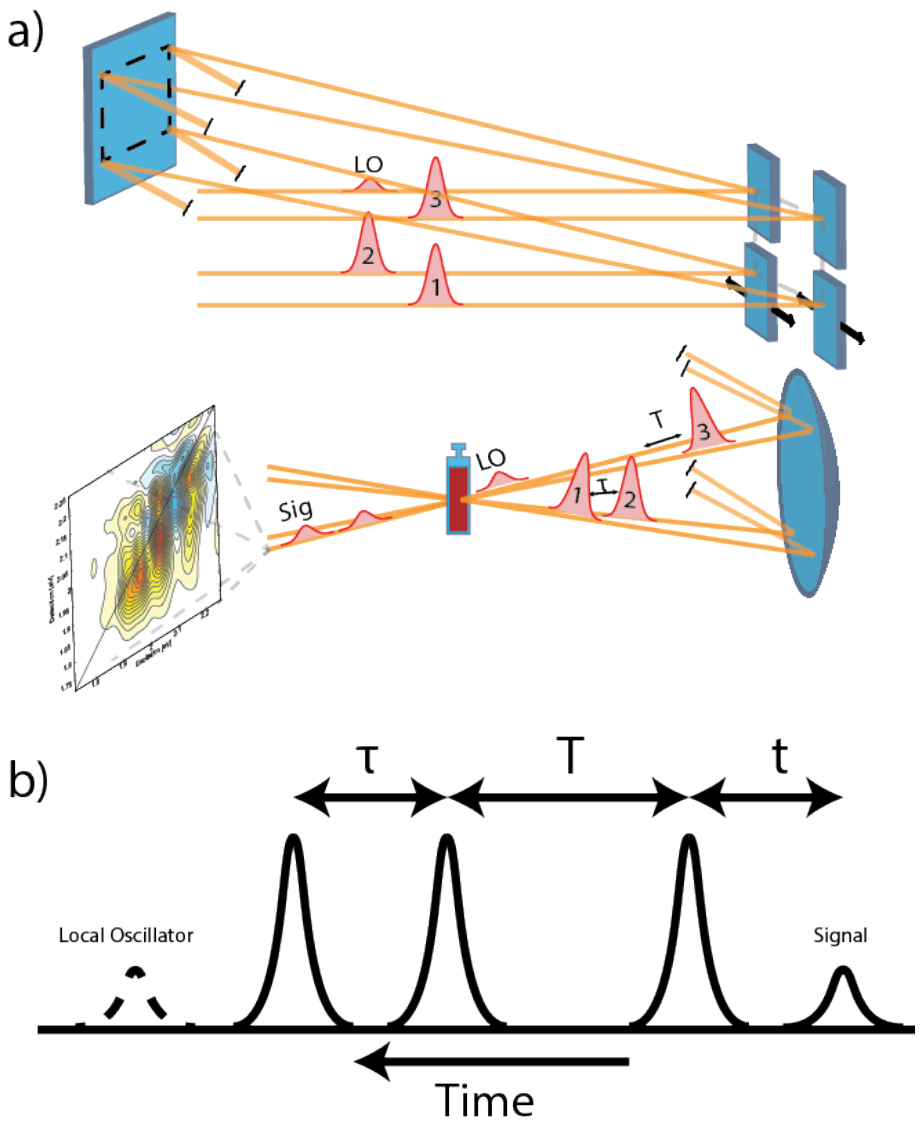

Figure 2.7: a) The all-reflective geometry of the 2D spectrometer in the Redfield Lab. Four laser pulses are created by a pair of beam splitters before hitting off of four independent square mirrors. The coherence time delay is created by translating the bottom two mirrors, which are tilted at slight angles to create a variable time delay when scanned perpendicular to the incoming beam path. After hitting these four mirrors, the beams hit a large single square mirror that directs the beams to an off-axis parabolic (OAP) mirror pair. The beams overlap in space at the sample position, which is placed at the focus of the OAP. The three primary beams are filtered by a spatial mask, and the signal and local oscillator beams are collected on a camera after being spectrally dispered by a grating.[35] b) In a 2DES experiment, the system is pumped by four laser pulses. Before the primary pulses interact, the local oscillator passes through the sample and is used to heterodyne detect the signal electric field. Then, the first of the three main pulses interacts with the sample. After a coherence time (τ) the second pulse interacts. The third pulse then hits the sample after a waiting time (T), and finally the signal pulse is emitted after the rephasing time (t).

2.2.3 Data Processing

After obtaining raw data from the 2D spectroscopy experiment, a number of processesing steps need to be taken to subtract the scatter and ultimately obtain an absorptive 2D cube of spectra at each waiting time point (Figure 2.8). The first step of 2DES data processing in the BOXCARS geometry is to produce an absolute valued 2D spectrum that windows out much of the scatter and the optical frequency from the raw data. This absolute value spectrum does not contain phase information, and so cannot distinguish GSB, SE, or ESA signals. First, for each time point, the rephasing and non-rephasing scans are combined onto a single coherence time axis for both signal and reference data. Then, the scatter is subtracted using the formula $Isig = I1234–I124–I34 + I4$ where $I1234$ is the raw data scan and $I124$, $I34$, and $I4$ are the various reference scans described in the previous section. This scatter subtracted data is then divided by the LO-only reference ($I4$) to remove artifacts due to variations in amplitude of the LO beam across the spectrum. The resulting data frame has a time-domain coherence (τ) axis and a frequency-domain rephasing (t) axis. The t axis is linear in wavelength and must be interpolated into frequency units (typically rad/fs). Next, the t axis is Fourier transformed to create a time-time data frame with both axes in the time domain. Here, the carrier frequency signal that is emitted at the time delay between beams 3 and 4 is subtracted using an apodized windowing function. Finally, the spectrum is Fourier transformed in both domains to produce a frequency-frequency domain 2D spectrum. This processing is applied to each waiting time point with identical windows, and the resulting frames are combined into a final data cube that is used for future analysis. This process may also be completed using just the rephasing or non-rephasing data to produce rephasing/non-rephasing 2D spectra.

Typically, the first analysis that must be performed on the absolute-value 2D spectrum is to recover the phase information. The raw 2D spectrum contains small errors in the phase of the signal that are due to inadequately knowing the exact time delay between the beams. This is because all beams travel different paths in a BOXCARS geometry and are

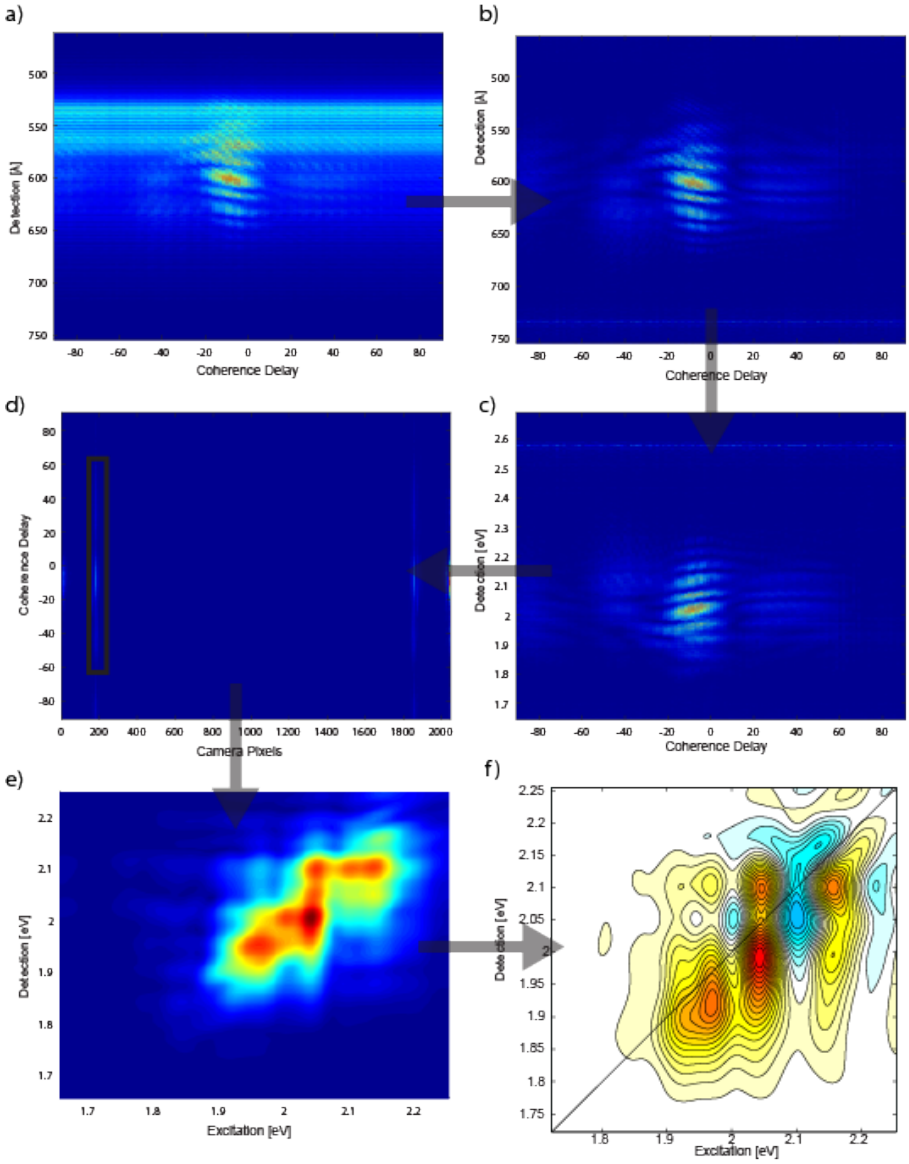

Figure 2.8: Representative example of processing a raw data frame into a real-valued 2D spectrum. a) The raw signal generated on the camera. The x-axis is the coherence time delay (τ) and the y-axis is the camera axis collected in wavelength after the signal beam is dispersed on an optical grating. b) Scatter is removed from the signal data frame by subtracting a series of reference scans that are collected alongside the signal. c) The data is interpolated from wavelength to frequency (rad/fs) d) After casting the data into frequency, the detection axis is Fourier transformed and the signal is windowed in the time-time domain to further isolate the signal. e) After windowing, the signal is Fourier transformed to the frequency-frequency domain, producing an absolute valued 2D spectrum. f) Using pump probe data collected on the sample using an identical laser spectrum, a phase correction is applied to the 2D spectrum. The resulting absorptive spectrum is shown.

susceptible to small fluctuations in temperature and humidity as well as drift in the laser pointing over time that introduce uncertainty in the relative path lengths that the beams travel. In a pump probe geometry such issues do not exist because the first two excitation pulses travel colinearly and the signal is detected in the direction of beam 3, so relative changes timing and therefore phase evolution for the coherence and rephasing times do not occur. Therefore, a transient absorption experiment using the same source, spectrum, lab conditions, and transmissive beam elements as a BOXCARS 2DES experiment can be used as a fitting parameter to determine the correct phase factors for the 2DES measurement. The 2D spectrum is summed down on the coherence axis and fit a separately collected pump probe experiment using the projection slice theorem (Eq. 2.13).[40]

$$PP(T,\omega_t) = Re[A\int_{-\infty}^{\infty} d_{\omega_\tau} S_{2D}(\omega_\tau, T, \omega_t) exp(i\phi + i(\omega_t - \omega_0)t_c(\omega_t - \omega_0)^2 t_q^2 + i(\omega_\tau - \omega_0)\tau_c(\omega_\tau - \omega_0)^2\tau_q^2] \quad (2.13)$$

Here ϕ is relative phase of the electric field and t_c, t_q, τ_c, and τ_q are correction factors that are fit to determine the phase of the 2D spectrum. The factors t_c and t_q are the linear and quadratic phase factors that determine the exact time delay between pulse 3 and the local oscillator as a function of the frequency, while τ_c and τ_q are similar linear and quadratic correction factors for the pulse 1 - pulse 2 time delay. This technique can identically be applied to the rephasing and non-rephasing 2D spectra by setting tau <0 or tau >0 respectively. Further information about our implementation of the phasing process can be found in Appendix A of this thesis.

REFERENCES

[1] Charles Kittel. *Introduction to solid state physics*. Wiley, 2004. ISBN: 9780471415268.

[2] Roald Hoffmann. *Solids and surfaces : a chemist's view of bonding in extended structures*, p. 142. ISBN: 9780471187103.

[3] Yoon-Suk Kim, Kerstin Hummer, and Georg Kresse. "Accurate band structures and effective masses for InP, InAs, and InSb using hybrid functionals". In: *Physical Review B* 80.3 (July 2009), p. 035203. ISSN: 1098-0121.

[4] Peter Y. Yu and Manuel Cardona. *Fundamentals of Semiconductors*. Graduate Texts in Physics. Berlin, Heidelberg: Springer Berlin Heidelberg, 2010. ISBN: 978-3-642-00709-5.

[5] Jeffrey M Pietryga, Young-Shin Park, Jaehoon Lim, Andrew F Fidler, Wan Ki Bae, Sergio Brovelli, and Victor I Klimov. "Spectroscopic and Device Aspects of Nanocrystal Quantum Dots". EN. In: *Chemical Reviews* 116.18 (Sept. 2016), pp. 10513–10622. ISSN: 0009-2665.

[6] Al. L. Efros and M Rosen. "The Electronic Structure of Semiconductor Nanocrystals". en. In: *Annual Review of Materials Science* 30.1 (Aug. 2000), pp. 475–521. ISSN: 0084-6600.

[7] Victor I Klimov. "Spectral and dynamical properties of multilexcitons in semiconductor nanocrystals". In: *Annual Review of Physical Chemistry* 58 (2007), pp. 635–673. ISSN: 0066-426X.

[8] Al. L Efros and Efros A. L. "Interband absorption of light in a semiconductor sphere". In: *Soviet Physics Semiconductors* 16 (1982), pp. 772–775.

[9] L E Brus. "A simple model for the ionization potential, electron affinity, and aqueous redox potentials of small semiconductor crystallites". en. In: *The Journal of Chemical Physics* 79.11 (Dec. 1983), pp. 5566–5571. ISSN: 0021-9606.

[10] A P Alivisatos, A L Harris, N J Levinos, M L Steigerwald, and L E Brus. "Electronic states of semiconductor clusters: Homogeneous and inhomogeneous broadening of the optical spectrum". en. In: *The Journal of Chemical Physics* 89.7 (Oct. 1988), pp. 4001–4011. ISSN: 0021-9606.

[11] C B Murray, D J Norris, and M G Bawendi. "Synthesis and characterization of nearly monodisperse CdE (E = sulfur, selenium, tellurium) semiconductor nanocrystallites". EN. In: *Journal of the American Chemical Society* 115.19 (Sept. 1993), pp. 8706–8715. ISSN: 0002-7863.

[12] Victor I Klimov. *Nanocrystal Quantum Dots*. 2010. ISBN: 9781420079265.

[13] Maksym V Kovalenko, Marcus Scheele, and Dmitri V Talapin. "Colloidal nanocrystals with molecular metal chalcogenide surface ligands." In: *Science (New York, N.Y.)* 324.5933 (June 2009), pp. 1417–20. ISSN: 1095-9203.

[14] Liberato Manna, Erik C. Scher, and A. Paul Alivisatos. "Synthesis of Soluble and Processable Rod-, Arrow-, Teardrop-, and Tetrapod-Shaped CdSe Nanocrystals". In: (2000).

[15] Margaret A. Hines and Philippe Guyot-Sionnest. "Synthesis and Characterization of Strongly Luminescing ZnS-Capped CdSe Nanocrystals". In: *The Journal of Physical Chemistry* 100.2 (Jan. 1996), pp. 468–471. ISSN: 0022-3654.

[16] Sandrine Ithurria and Benoit Dubertret. "Quasi 2D Colloidal CdSe Platelets with Thicknesses Controlled at the Atomic Level". In: *Journal of the American Chemical Society* 130.49 (2008), pp. 16504–+. ISSN: 0002-7863.

[17] David M Jonas. "Two-Dimensional Femtosecond Spectroscopy". en. In: *Annual Review of Physical Chemistry* 54.1 (Oct. 2003), pp. 425–463. ISSN: 0066-426X.

[18] Minhaeng Cho, Tobias Brixner, Igor Stiopkin, Harsha Vaswani, and Graham R Fleming. "Two Dimensional Electronic Spectroscopy of Molecular Complexes". In: *Journal of the Chinese Chemical Society* 53.1 (2006), pp. 15–24.

[19] Eric W.-G. Diau, Jennifer L. Herek, Zee Hwan Kim, and Ahmed H. Zewail. "Femtosecond activation of reactions and the concept of nonergodic molecules". In: *Science (New York, N.Y.)* 279.5352 (Feb. 1998), pp. 847–51. ISSN: 1095-9203.

[20] Minhaeng Cho, Harsha M Vaswani, Tobias Brixner, Jens Stenger, and Graham R. Fleming. "Exciton Analysis in 2D Electronic Spectroscopy". en. In: *The Journal of Physical Chemistry B* 109.21 (June 2005), pp. 10542–10556. ISSN: 1520-6106.

[21] Minhaeng Cho. "Coherent Two-Dimensional Optical Spectroscopy". en. In: *Chemical Reviews* 108.4 (Apr. 2008), pp. 1331–1418. ISSN: 0009-2665.

[22] Yuan-Chung Cheng, Gregory S Engel, and Graham R Fleming. "Elucidation of population and coherence dynamics using cross-peaks in two-dimensional electronic spectroscopy". In: *Chemical Physics* 341.1-3 (Nov. 2007), pp. 285–295. ISSN: 03010104.

[23] Justin R Caram, Haibin Zheng, Peter D Dahlberg, Brian S Rolczynski, Graham B Griffin, Dmitriy S Dolzhnikov, Dmitri V Talapin, and Gregory S Engel. "Exploring size and state dynamics in CdSe quantum dots using two-dimensional electronic spectroscopy". In: *Journal of Chemical Physics* 140.8 (2014). ISSN: 0021-9606.

[24] T Brixner, T Mancal, I V Stiopkin, and G R Fleming. "Phase-stabilized two-dimensional electronic spectroscopy". In: *Journal of Chemical Physics* 121.9 (2004), pp. 4221–4236. ISSN: 0021-9606.

[25] Gregory S Engel, Tessa R Calhoun, Elizabeth L Read, Tae-Kyu Ahn, Tomáš Mančal, Yuan-Chung Cheng, Robert E Blankenship, and Graham R Fleming. "Evidence for wavelike energy transfer through quantum coherence in photosynthetic systems". En. In: *Nature* 446.7137 (Apr. 2007), pp. 782–786. ISSN: 0028-0836.

[26] Daniel B Turner, Rayomond Dinshaw, Kyung-Koo Lee, Michael S Belsley, Krystyna E Wilk, Paul M G Curmi, and Gregory D Scholes. "Quantitative investigations of quantum coherence for a light-harvesting protein at conditions simulating photosynthesis". In: *Physical Chemistry Chemical Physics* 14.14 (2012), p. 4857. ISSN: 1463-9076.

[27] Moira L Flanagan, Phillip D Long, Peter D Dahlberg, Brian S Rolczynski, Sara C Massey, and Gregory S Engel. "Mutations to R. sphaeroides Reaction Center Perturb Energy Levels and Vibronic Coupling but Not Observed Energy Transfer Rates". EN. In: *The Journal of Physical Chemistry A* 120.9 (Mar. 2016), pp. 1479–1487. ISSN: 1089-5639.

[28] Lili Wang, Graham B. Griffin, Alice Zhang, Feng Zhai, Nicholas E. Williams, Richard F. Jordan, and Gregory S. Engel. "Controlling quantum-beating signals in 2D electronic spectra by packing synthetic heterodimers on single-walled carbon nanotubes". In: *Nature Chemistry* 9.3 (Mar. 2017), pp. 219–225. ISSN: 1755-4330.

[29] Yuan-Chung Cheng and Graham R Fleming. "Coherence Quantum Beats in Two-Dimensional Electronic Spectroscopy". In: *The Journal of Physical Chemistry A* 112.18 (May 2008), pp. 4254–4260. ISSN: 1089-5639.

[30] Justin R Caram, Haibin Zheng, Peter D Dahlberg, Brian S Rolczynski, Graham B Griffin, Andrew F Fidler, Dmitriy S Dolzhnikov, Dmitri V Talapin, and Gregory S Engel. "Persistent Interexcitonic Quantum Coherence in CdSe Quantum Dots". In: *Journal of Physical Chemistry Letters* 5.1 (2014), pp. 196–204. ISSN: 1948-7185.

[31] S. (Shaul) Mukamel. *Principles of nonlinear optical spectroscopy*. Oxford University Press, 1995, p. 543. ISBN: 0195092783.

[32] Erik M. Grumstrup, Sang-Hee Shim, Matthew A. Montgomery, Niels H. Damrauer, and Martin T. Zanni. "Facile collection of two-dimensional electronic spectra using femtosecond pulse-shaping Technology". In: *Optics Express* 15.25 (Dec. 2007), p. 16681. ISSN: 1094-4087.

[33] Howe-Siang Tan. "Theory and phase-cycling scheme selection principles of collinear phase coherent multi-dimensional optical spectroscopy". In: *The Journal of Chemical Physics* 129.12 (Sept. 2008), p. 124501. ISSN: 0021-9606.

[34] Zhengyang Zhang, Kym Lewis Wells, Edward William James Hyland, and Howe-Siang Tan. "Phase-cycling schemes for pump–probe beam geometry two-dimensional electronic spectroscopy". In: *Chemical Physics Letters* 550 (Oct. 2012), pp. 156–161. ISSN: 0009-2614.

[35] Haibin Zheng, Justin R Caram, Peter D Dahlberg, Brian S Rolczynski, Subha Viswanathan, Dmitriy S Dolzhnikov, Amir Khadivi, Dmitri V Talapin, and Gregory S Engel. "Dispersion-free continuum two-dimensional electronic spectrometer". In: *Applied Optics* 53.9 (2014), pp. 1909–1917. ISSN: 1559-128X.

[36] Sergei A. Trushin, Kyriaki Kosma, Werner Fuß, and Wolfram E. Schmid. "Sub-10-fs supercontinuum radiation generated by filamentation of few-cycle 800 nm pulses in argon". In: *Optics Letters* 32.16 (Aug. 2007), p. 2432. ISSN: 0146-9592.

[37] Vadim V Lozovoy, Igor Pastirk, and Marcos Dantus. "Multiphoton intrapulse interference IV Ultrashort laser pulse spectral phase characterization and compensation". EN. In: *Optics Letters* 29.7 (Apr. 2004), p. 775. ISSN: 0146-9592.

[38] Yizhu Zhang, Kristina Meyer, Christian Ott, and Thomas Pfeifer. "Passively phase-stable, monolithic, all-reflective two-dimensional electronic spectroscopy based on a four-quadrant mirror". EN. In: *Optics Letters* 38.3 (Feb. 2013), p. 356. ISSN: 0146-9592.

[39] Patrick F. Tekavec, Jeffrey A. Myers, Kristin L. M. Lewis, Franklin D. Fuller, and Jennifer P. Ogilvie. "Effects of chirp on two-dimensional Fourier transform electronic spectra". In: *Optics Express* 18.11 (May 2010), p. 11015. ISSN: 1094-4087.

[40] V P Singh, A F Fidler, B S Rolczynski, and G S Engel. "Independent phasing of rephasing and non-rephasing 2D electronic spectra". en. In: *The Journal of Chemical Physics* 139.8 (Aug. 2013), p. 084201. ISSN: 0021-9606.

CHAPTER 3

THE ORIGIN OF BROAD EMISSION SPECTRA OF INP QUANTUM DOTS: CONTRIBUTIONS FROM STRUCTURAL AND ELECTRONIC DISORDER

Adapted with permission from E.M. Janke*, N.E. Williams*, C. She, D. Zherebetskyy, M. Hudson, L. Wang, D.J. Gosztola, R.D. Schaller, B. Lee, C. Sun, G.S. Engel, D.V. Talapin. The Origin of Broad Emission Spectra of InP Quantum Dots: Contributions from Structural and Electronic Disorder. JACS (2018).

3.1 Abstract

The ensemble emission spectra of colloidal InP quantum dots are broader than achievable spectra of cadmium- and lead-based quantum dots, despite similar single-particle line widths and significant efforts invested in the improvement of synthetic protocols. We seek to explain the origin of persistently broad ensemble emission spectra of colloidal InP quantum dots by investigating the nature of the electronic states responsible for luminescence. We identify a correlation between red-shifted emission spectra and anomalous broadening of the excitation spectra of luminescent InP colloids, suggesting a trap-associated emission pathway in highly emissive core–shell quantum dots. Time-resolved pump–probe experiments find that electrons are largely untrapped on photoluminescence relevant time scales pointing to emission from recombination of localized holes with free electrons. Two-dimensional electronic spectroscopy on InP quantum dots reveals multiple emissive states and increased electron–phonon coupling associated with hole localization. These localized hole states near the valence band edge are hypothesized to arise from incomplete surface passivation and structural disorder associated with lattice defects. We confirm the presence and effect of lattice disorder by X-ray absorption spectroscopy and Raman scattering measurements. Participation of localized electronic states that are associated with various classes of lattice defects gives rise to

phonon-coupled defect related emission. These findings explain the origins of the persistently broad emission spectra of colloidal InP quantum dots and suggest future strategies to narrow ensemble emission lines comparable to what is observed for cadmium-based materials.

3.2 Introduction

Colloidal quantum dots (QDs) represent an important class of tunable light emitters with narrow emission line widths that produce saturated colors. To date, semiconductor systems incorporating cadmium[1] or lead[2, 3] have achieved the best combination of performance parameters including emission colors spanning the visible spectrum, luminescence quantum yield, and narrow emission line widths. Indium phosphide QDs are a promising alternative that retains the spectral range of size tunable emission while expanding the scope of applicability of soluble semiconductor emitters. By avoiding the use of the toxic heavy metals Pb and Cd, InP-based emitters are a viable solution to a broad range of consumer lighting and display technologies, and to biological labeling and imaging applications which preclude the use of emitters that leach heavy metal ions. While efforts to improve InP quantum dot synthesis have raised photoluminescence quantum yields to over 80%,[4] achievable color purity remains modest with persistently broad ensemble emission profiles. Investigations of single-particle line widths[5–7] have reported comparably narrow single-particle emission from InP and CdSe QDs, though achievable ensemble emission spectra from InP colloids remain roughly double what is attained from CdSe quantum dots. The question remains open as to why the synthetic optimization paradigm which has been so successful for materials like CdSe has encountered such difficulty with InP. A likely path to the answer lies in identifying the key characteristics that distinguish InP QDs from the CdSe model system. Recent studies[8–11] have focused on this aspect and have found strong evidence that the growth of colloidal InP proceeds via nonclassical nucleation dominated mechanisms in contrast to that of CdSe. The result can lead to polydispersity of particle sizes and a corresponding broadening of ensemble emission. The effect of size distribution may be particularly impor-

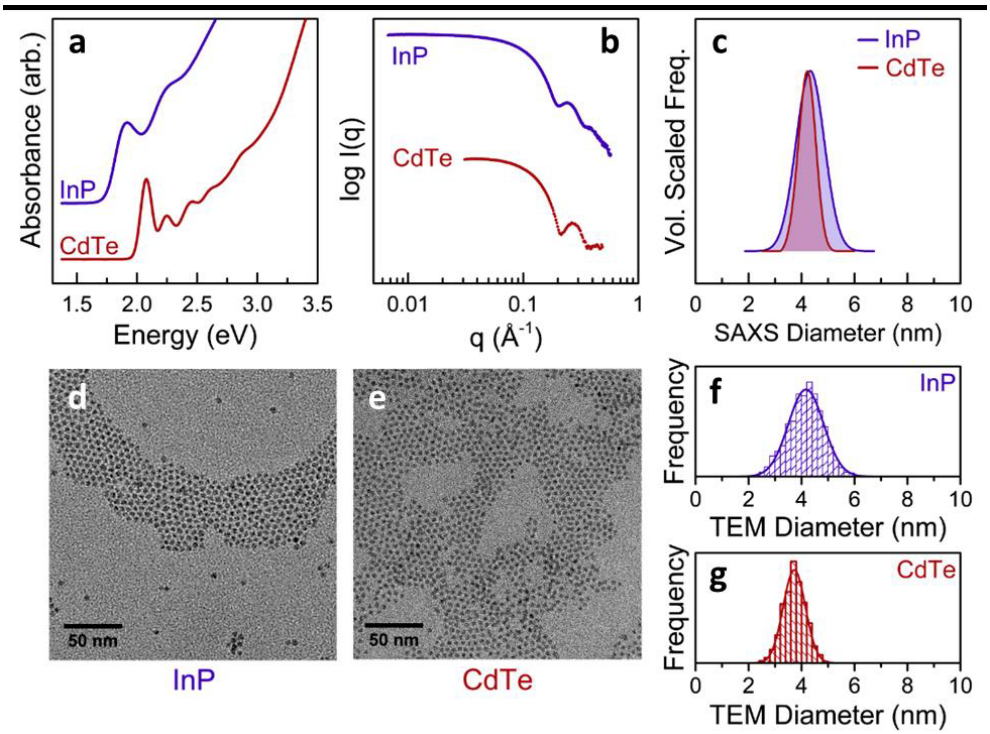

Figure 3.1: a. Absorption spectra of 4nm diameter CdTe and InP nanocrystals. b. SAXS patterns for each material measured as a colloid in toluene. c. Extracted volume scaled diameter distributions from SAXS. d.,e. TEM images of InP and CdTe. f.,g. Particle size distribution histograms extracted by TEM image analysis.

tant for colloidal InP emitters compared to CdSe because of a steeper relation between the band gap and crystallite size (so-called sizing curve) for InP. For a given percent dispersity in nanocrystal size, InP produces a larger range of confinement energies than CdSe. However, the sizing curves for CdTe and InP are very similar, and CdTe colloids can reliably be prepared with very narrow features in the ensemble emission and absorption without postsynthesis size fractionation (Figure 3.1 and Figure 3.2).

Despite more than 20 years of active research on InP QDs, we are unaware of published examples of InP QDs with ensemble emission spectra comparable in width to those routinely reported for high-quality CdTe QDs. If the size distribution were the dominant factor in determining ensemble PL line width in colloidal InP, we expect that energy-selective spectroscopic techniques, such as photoluminescence excitation spectra collected for narrow selected energy ranges of emission, should extract the absorption features of a very monodisperse sub-

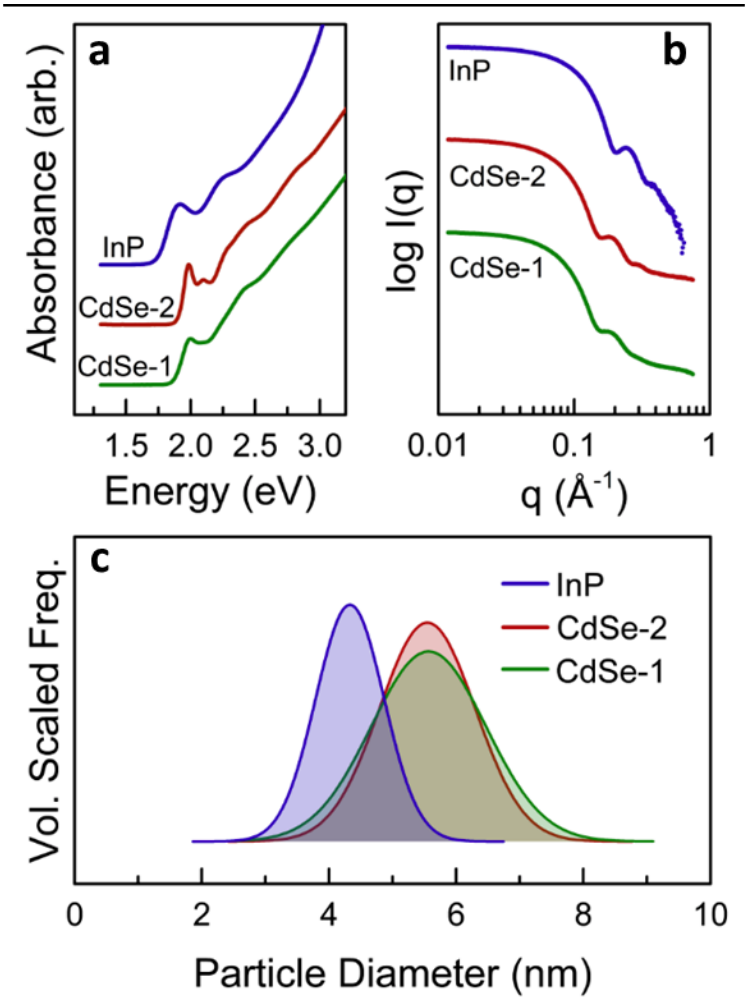

Figure 3.2: Small angle x-ray scattering for size distribution analysis. (a) Offset absorption spectra comparing CdSe of two different levels of polydispersity to a size selected sample of InP. (b) Scattering data and (c) Gaussian size distributions extracted by fitting the scattering traces.

population of particles. However, this is not generally true. Unlike the case for common II-VI systems like CdSe and CdTe, narrow selected bands of the InP emission profile correlate with a broad absorption profile. The implication is that either homogeneous line widths are broad, or they are narrow, and particles emitting at the same energy can have substantially different absorption profiles. As we report here, behavior of InP emission is strongly dependent on sample chemical history and is related to the presence of lattice disorder. In this work, we consider internal disorder within InP quantum dots as an additional factor, independent of particle size, which confounds the preparation of colloidal InP with narrow ensemble emission. We provide evidence for the effect of chemical disorder in broadening the emission line shapes of InP QDs made highly luminescent by two chemically distinct passivation methods including HF etching and ZnS shelling. Despite the very different chemistries involved in these two passivation strategies, both share a common propensity to introduce disorder related electronic states. In particular, we show that the common practice of growing InP/ZnS core- shell structures by inclusion of the Zn precursor during the InP growth results in lattice doping by Zn that introduces a new, phonon-coupled, radiative recombination channel.

3.3 Results and Discussion

3.3.1 Synthesis and Surface Passivation of InP Quantum Dots for Improved Photoluminescence

We synthesized InP colloidal quantum dots by common literature methods[12, 13], reacting $InCl_3$ as the indium precursor and either tris(trimethylsilyl)phosphine or tris(dimethylamino)-phosphine as phosphorus precursors. The colloids were washed in a nitrogen glovebox by repeated dissolution in toluene and precipitation using ethanol as a nonsolvent. Finally, the particles were stored as a colloidal stock solution in toluene. These freshly prepared particles are poorly luminescent and are termed "as-synthesized InP" for the purposes of this study. We additionally consider two chemically different types of luminescent InP samples:

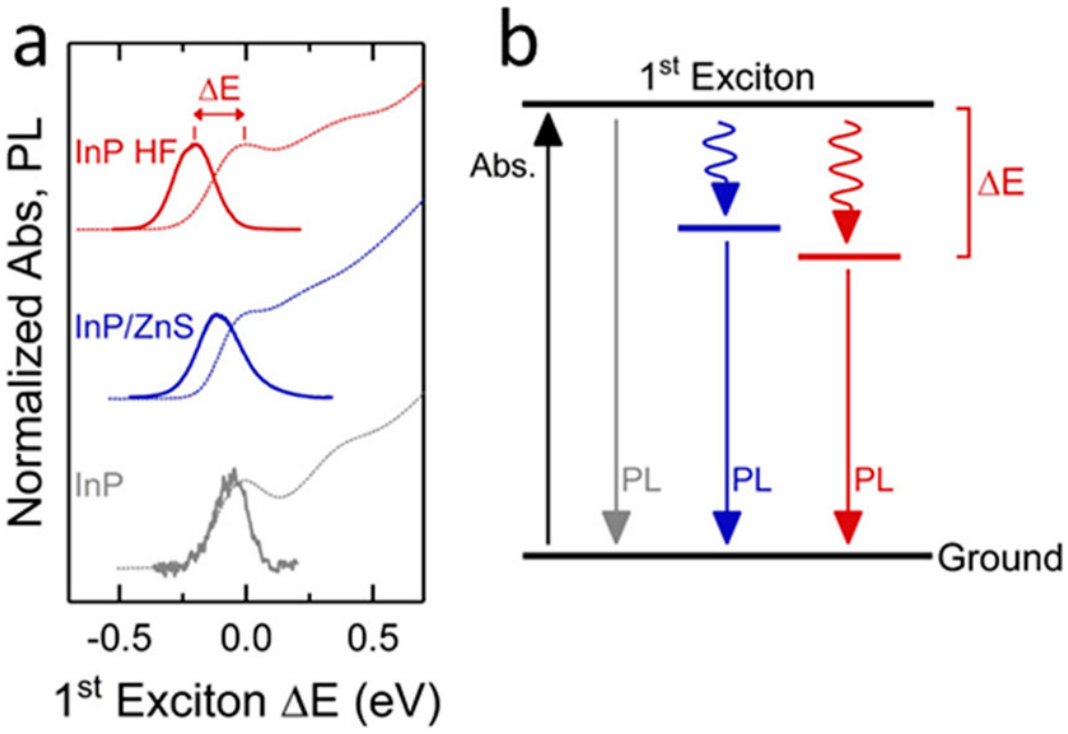

Figure 3.3: Emission red shift of InP quantum dots (QDs). (a) Absorption and emission spectra for three types of InP QDs plotted on a scale zeroed at the first exciton energy. Treatments commonly used to enhance PL quantum yield result in emission bands that are shifted red of the first excitonic absorbance by varying amounts. (b) Differing amounts of nonradiative energy dissipation precede emission for different types of luminescent InP QDs.

"InP/ZnS" core-shells synthesized by established protocols[13–15] and as-synthesized InP cores made luminescent by passivation with dilute (200 ppm) HF. Exposure of InP quantum dots to HF solution under nitrogen atmosphere and with particles protected from light results in a modest increase of photoluminescence (PL) quantum yield from nearly zero out of synthesis to around 1% after the treatment. As has been reported previously,[16, 17] when this HF treatment is conducted under illumination and in air, it results in slow etching and oxidation accompanied by a significant increase in PL quantum yields to 20-40%. This highly luminescent material derived from the as-synthesized particles is termed "InP-HF".

InP quantum dots display an interesting and unusual relationship between their behavior as emitters and the chemistry involved in their preparation and surface passivation. Aerobic HF etching introduces a large red shift of the PL band relative to the first absorption

maximum (Figure 3.3a). The relatively large emission red shift in aerobically HF-treated InP is also observed in highly emissive InP/ZnS core-shell samples grown via the commonly used method wherein InP cores are grown from a solution containing mixed In and Zn metal precursors.[13, 15, 18] Subsequent addition of a sulfur precursor induces the free Zn already present in the reaction mixture to react and form a ZnS shell over the InP cores. Though this route to making InP/ZnS core-shell structures has been previously hypothesized to produce pure InP cores with surface bound Zn, we provide evidence in this work that some Zn remains trapped in the lattice of the cores occupying In sites of the InP lattice. While this chemistry is very distinct from the HF-based passivation scheme, the resulting material shows similar PL quantum yield, line width, and a PL band centered greater than 150 meV red of the first absorption maximum. The red shift of the emission across these multiple classes of InP shown in Figure 3.3a suggests that more than one radiative recombination pathway is active in the material. We refer to this ensemble emission red shift represented by ΔE in Figure 3.3 as "Stokes shift" for the remainder of our discussion.

3.3.2 Photoluminescence Excitation (PLE) Spectroscopy

Photoluminescence excitation (PLE) spectroscopy allows examination of subsets of emitters within the samples and sheds light on the homogeneity of emitting states in QDs. Analysis of ensemble emission of InP, CdSe, and CdTe colloids by PLE reveals a clear difference between the materials. PLE spectra of polydisperse CdSe and CdTe yield excitation spectra corresponding to narrow emission subbands. When taken in steps across the whole emission profile, each PLE spectrum strongly resembles an absorption spectrum of a monodisperse sample with multiple well-resolved excitonic transitions (Figure 3.4a).

Such behavior is observed from samples with different surface passivation schemes, including plain cores and various core-shell structures with II-VI core materials.[7, 19] As-synthesized InP QDs which are neither shelled nor exposed to oxidative HF treatment show similar behavior to CdSe and CdTe; PLE spectra narrow significantly compared to the en-

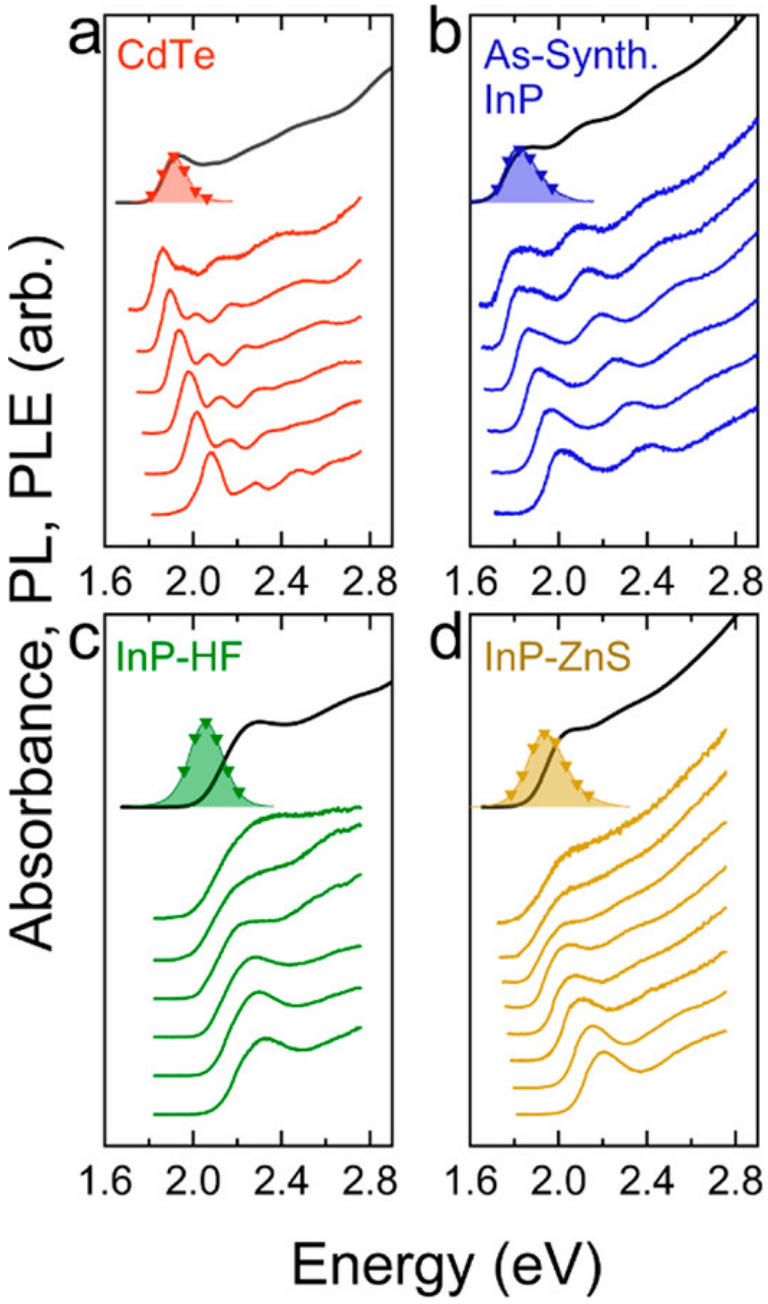

Figure 3.4: Absorption (black traces), PL (shaded), and PLE spectra (colored traces) for polydisperse CdTe QDs (a), as-synthesized InP cores (b), HF-treated InP (c), and InP-ZnS core-shell QDs (d). The PLE spectra are collected by scanning at emission energies marked by triangles. Spectra are offset higher for successively redder emission energies scanned.

semble absorption and spectral features shift as the selected emission energy is varied (Figure 3.4b). This observation suggests that there is no fundamental barrier that prevents colloidal InP QDs from achieving the narrow emission lines that are commonly obtained for II-VI emitters. While the data from unoxidized and unshelled samples imply that InP emitters with low PL quantum yield behave qualitatively similarly to CdSe and CdTe, the samples of InP with bright PL show a significantly different behavior (Figure 3.4c,d). InP samples that are treated with HF under illumination and exposure to air or, alternatively, samples that are passivated by ZnS shells both exhibit bright PL that is significantly redshifted from the first absorption peak. Both samples yield broad excitation spectra that broaden further as the analyzed emission band is shifted redder. As excitation spectra are measured for successively redder emission bands, their spectral features broaden further but do not appreciably change in energy. This data suggests that redder emission is not correlated with redder absorbers in these samples. In other words, the emission at the red-edge of the PL spectrum does not simply originate from a subpopulation of emitters with redder transition energies but rather from a subpopulation of emitters that have a similar absorption edge as the entire ensemble average but that are able to emit redder. For typical high-quantum-yield samples of InP, including those shown in Figure 3.4c,d, the first exciton in the PLE spectra for deep red emission occurs approximately 200 meV blue of the scanned emission band. Figure 3.5 summarizes the results of the PLE studies by comparing ensemble absorption line widths to those of the corresponding excitation spectra extracted from the center of the emission band. We show data for four samples of II-IV semiconductor emitters: CdSe-1(polydisperse), CdSe-2- (monodisperse), CdTe-1(polydisperse), and CdTe-2- (monodisperse). Here, "polydisperse" denotes a sample with ensemble PL broadened by 50% relative to the corresponding "monodisperse" sample.

From these four samples we extract PLE spectra with a roughly 90 meV full width at half-maximum (fwhm) of the first excitonic feature independent of material or polydispersity. That we do not extract narrower PLE spectra for the more monodisperse samples suggests

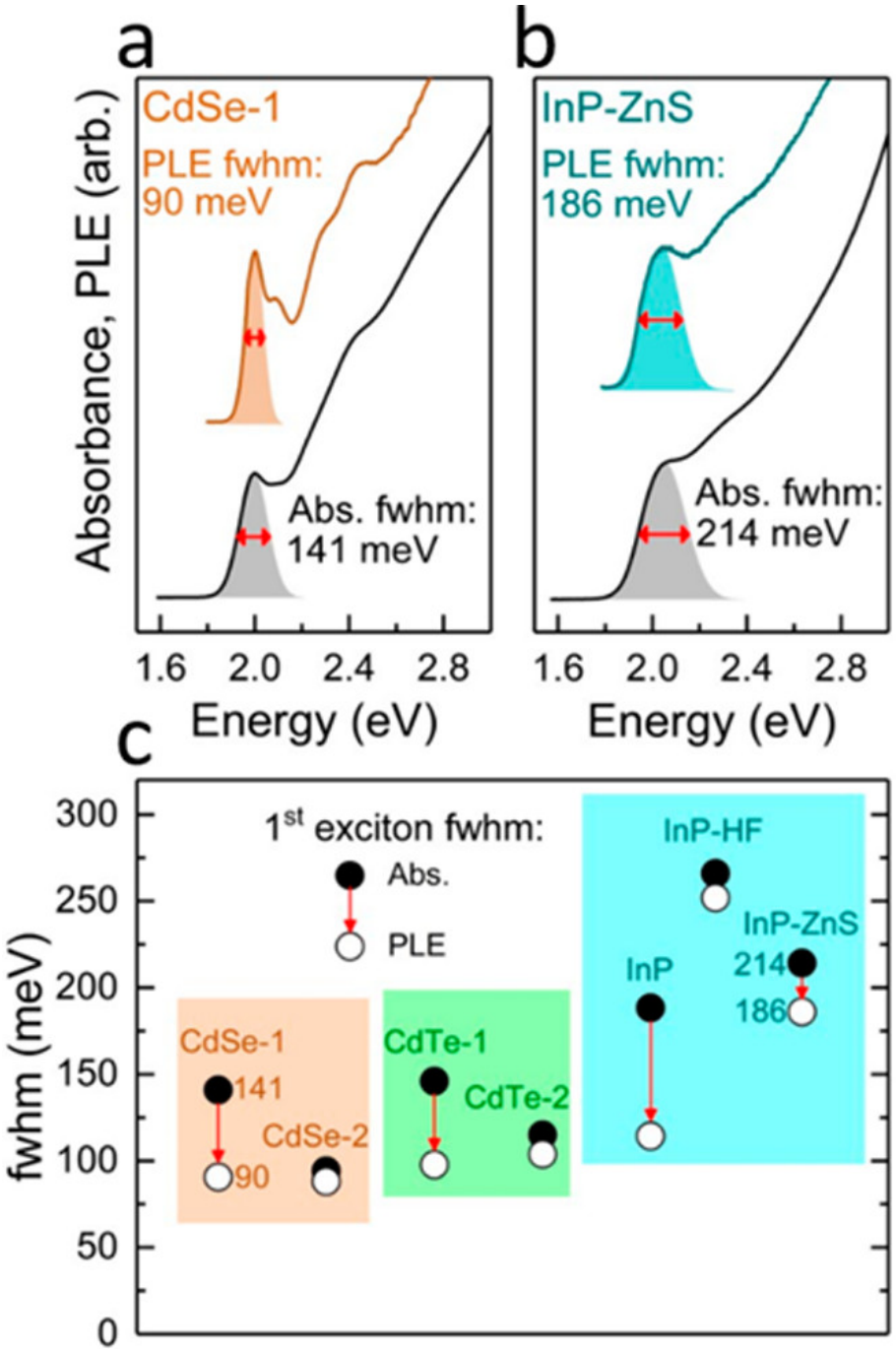

Figure 3.5: Comparison of ensemble absorption spectrum and PLE spectrum line widths. (a, b) Gaussian fits (shaded) compare the fwhm of the first excitonic peak in absorption (black) and PLE (colored) for polydisperse CdSe (a) and InP-ZnS core-shells (b). (c) Summary of first exciton fwhm for absorption (black circles) and PLE (white circles) for a variety of QD samples. PLE line width values are extracted from spectra obtained by scanning the center of the PL band for each sample. CdSe and CdTe samples appended by "1" and "2" represent more polydisperse and more monodisperse samples, respectively.

that this 90 meV value originates from a combination of the single-particle emission line width and measurement related broadening. The weakly emitting InP sample (Figures 3.4b and 3.5c) behaves similarly to CdSe and CdTe QDs yielding a narrowed PLE spectrum with a 114 meV first exciton fwhm. The roughly 20% broader line width for InP compared to CdSe and CdTe is consistent with prior determinations[5] of the single-particle emission widths of these materials. In contrast, the brightly emitting classes of InP (Figure 3.4c,d, InP-HF and InP-ZnS) both yield broad features in their PLE spectra. This observation contradicts the characterization of these bright InP colloids as emitting from a size distribution broadened ensemble of narrow single emitters. Rather, it points to the bright red-shifted PL as resulting from a shallow trap assisted radiative recombination process. If the depth of trap states (ΔE in Figure 3.3b) varies from dot to dot, broad ensemble emission is expected from reasonably monodisperse samples of InP QDs that show narrow emission lines in single-particle PL studies. In the following sections we will investigate the nature of the emissive states in bright InP QDs.

3.3.3 Transient Absorption and Streak Camera Studies of the Picosecond Excited Carrier Dynamics

Transient absorption (TA) and fast time-resolved photoluminescence measurements by streak camera were undertaken to further understand the role of HF etching and ZnS shelling in bringing about bright luminescence. In particular, we sought to understand the effect of passivation chemistry on the lifetimes of photogenerated electrons and holes individually. According to the state filling picture[20] for describing TA in quantum confined II-VI and III-V semiconductors, differential absorption signals are dominated by the state occupation of the electron due to its lower effective mass and the lower degeneracy of the conduction band. For example, in the case of InP[21] the electron effective mass is $0.08m_e$ compared to a hole effective mass of $0.6m_e$. We thus expect that decay kinetics of the transient bleaching signal will only reflect electron state occupation and will be relatively insensitive to hole-trapping

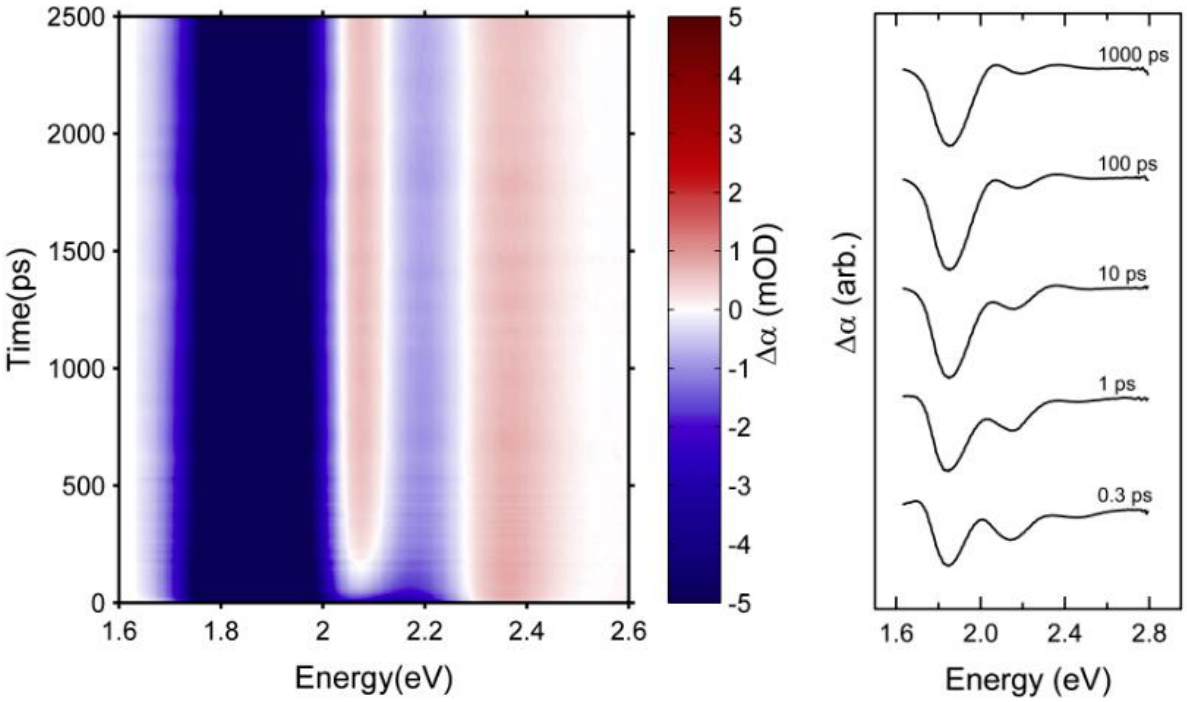

Figure 3.6: Left, a colormap showing the spectral evolution of the transient absorption of an as– synthesized InP sample as an example dataset. Right: offset, un-normalized $\Delta\alpha$ spectra extracted at a discrete series of probe delays (0.3ps – 1000 ps) from the same data used to generate the colormap at left. The observation that evolution of the shape of the $\Delta\alpha$ spectrum ceased completely by 100 picoseconds was found to hold generally for all samples considered. For probe delays of 100 ps and longer, the $\Delta\alpha$ signal at all probe energies simply decayed monotonously.

events. In contrast, picosecond time scale PL measurements provide information about the net population of the emissive state. Irreversible trapping of either carrier will contribute to the observed kinetics. With the combination of the two techniques, the relationship between InP passivation chemistry and the relaxation pathways of electrons and holes can be understood. A pump-probe TA experiment with blue pump (3.0 eV) and broadband probe yielded a set of differential absorption spectra vs pump delay for all samples. Spectra taken in the first few picoseconds following excitation show a rapid spectral evolution due to carrier cooling (Figure 3.6).

Following the completion of this process, the spectral evolution ceases; the shape of the differential absorption spectrum then remains static, and the signal strength decays monotonously with increasing pump delay. At this stage, photoexcited electrons bleach the oscillator strength of transitions which correspond to promotions of valence band electrons to the occupied conduction band level.

Accordingly, the strongest and slowest decaying signal is a bleach which corresponds in energy and line shape to the first excitonic feature in the linear absorption spectrum (Figure 3.7a). The energy of this transition has a well-studied dependence on nanocrystal size due to quantum confinement effects.[17, 22] Thus, electrons relax to a delocalized 1Se "particle in a spherical box" state and bleach the first excitonic absorption by blocking valence band to 1Se transitions. The first exciton bleach recovery kinetics on the time scale of hundreds of picoseconds should then simply track the population of electrons in the 1Se state: $|\Delta\alpha| \propto$ [e-]. Analysis of these kinetics (Figure 3.7b) for samples with different surface passivation chemistries finds that decay of the conduction band electron population is slow on the subnanosecond time scale. Measurements at longer probe delays (Figure 3.6) find that depletion of the 1Se state following the pump takes place over tens of nanoseconds, a rate similar to that of radiative recombination in emissive samples. Slow kinetics were seen for all samples investigated with no apparent connection between the rate of bleach recovery and the steady-state PL quantum yield of the sample. These data imply that electron trapping rates are similar, and negligible, in all samples. This is a surprising conclusion given that the PL quantum yields of the HF-treated samples are approximately 3 orders of magnitude greater than the as-synthesized QDs. These results imply that subnanosecond PL quenching in the nonluminescent samples can be attributed to hole trapping. To validate our interpretation of the pump-probe TA data as providing selective information about electron dynamics, we conducted an additional control experiment by repeating measurements with addition of an electron scavenger, methyl viologen dichloride (MV2+), to the nanocrystal solutions under investigation. Previous studies of carrier dynamics in QDs,[23, 24] have used MV2+ as a

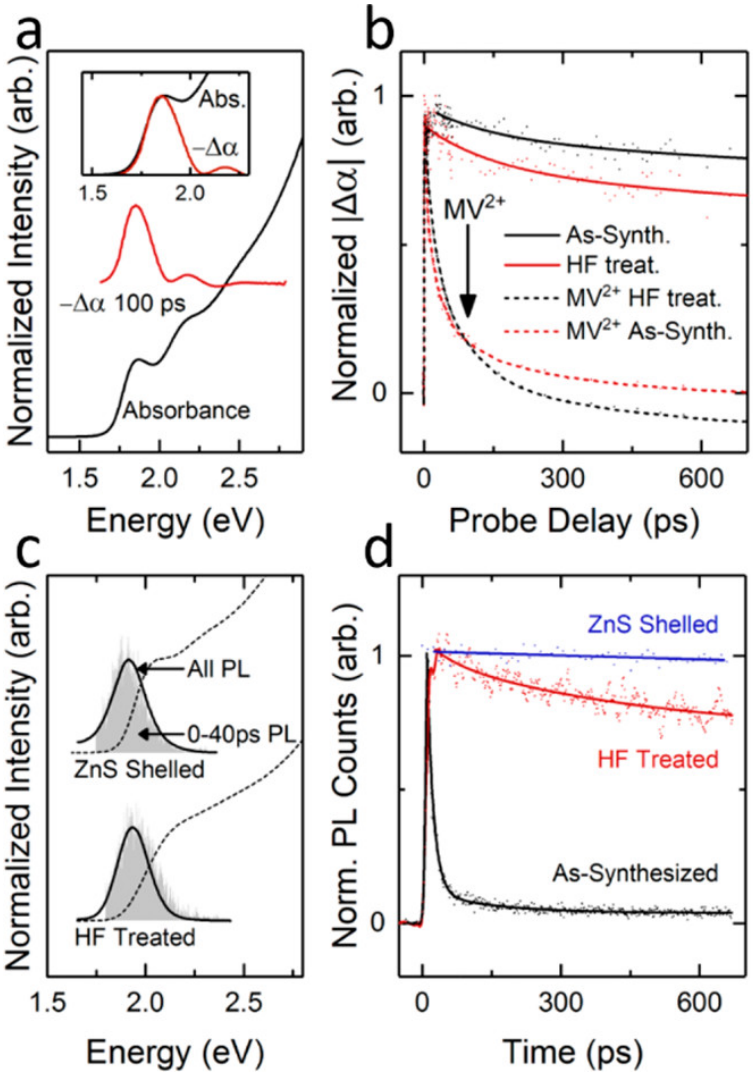

Figure 3.7: (a) Absorbance and 100 ps probe delay differential absorption spectra from InP without postsynthetic modifications. Inset compares the linear absorption lineto the ground state bleach of the first exciton. The pump energy is 3.0 eV. (b) Intensity of the first exciton bleach vs probe delay time for as-synthesized and HF-treated InP. Dashed lines show measurements where methyl viologen dichloride (MV2+), acting as the electron scavenger, was added to the sample. (c) Comparison of steady-state PL spectra, solid lines, and emission in the 40 ps following a pulsed excitation measured by streak camera, shaded gray. Dashed lines show the corresponding absorption spectra. (d) Spontaneous PL decay for three types of InP also by streak camera. Excitation is at 3.1 eV for the steady-state and pulsed PL measurements.

selective electron scavenger which undergoes rapid reduction by photogenerated conduction band electrons. Indeed, addition of MV2+ to the InP QD solutions results in rapid loss of the conduction band electron population following excited state electron transfer to MV2+ (Figure 3.7b). The spectroscopic signature of the singly reduced methyl viologen radical MV•+ appears concomitantly with the loss of the bleach signal from the QDs and decays negligibly slowly over the 2.5 ns time interval of the TA experiment. The long life of the radical indicates that there is no fast hole transfer following the initial electron transfer. Rather, the reduced MV•+ radical coexists with positively charged QDs. Additionally, there is not a strong differential absorption signature observed from the hole remaining on these positively charged InP quantum dots, an observation that agrees well with the prediction that the high valence band density of states will obscure the contribution of a single valence band hole to the absorbance. The conclusion is that, for all InP chemistries studied, electron trapping is negligible on subnanosecond scales unless an electron trapping species is intentionally introduced.

In contrast, measurements of photoluminescence show a strong relationship between surface chemistry and kinetics (Figure 3.7d). While luminescent HF-treated and ZnS-shelled quantum dots show a PL decay that matches the TA kinetics (Figure 3.8), for as-synthesized InP PL decay is quite fast. Given the long lifetime of electrons in the 1Se state, the observed PL decay kinetics on the subnanosecond time scale can be attributed to hole-trapping rates. PL decay dominated by hole trapping allows the kinetics in Figure 4d to be interpretable as tracking the hole population remaining in a state that can recombine radiatively with electrons in the 1Se state: IPL $\propto$ [h+]. This is in line with predictions made by previous studies of the photochemical mechanism of HF passivation[16, 25] and contradicts other reports[26, 27] which pointed to electron trapping at phosphorus vacancies as the predominant source of PL quenching in unmodified InP QDs. As InP QDs show PL decay rates which either match or greatly exceed the decay rate of the 1Se population, PL is expected to come from recombination of holes with these delocalized conduction band electrons. A question

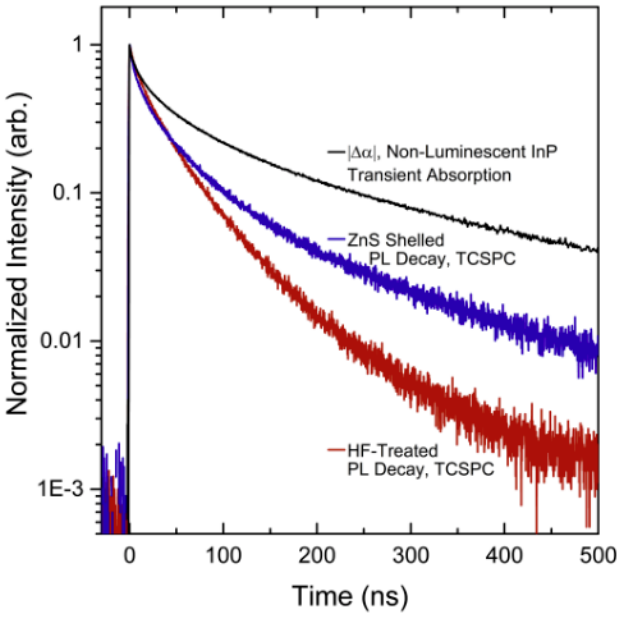

Figure 3.8: A comparison of bleach recovery and PL decay at the hundreds of nanoseconds timescale. The black trace shows the bleach recovery kinetics obtained from a transient absorption setup using an electronically delayed pump. The blue and red traces show PL lifetime data obtained from TCSPC for InP made luminescent by post–synthesis ZnS shelling or by HF treatment. Even for non–luminescent InP with PL decay on the timescale of tens of picoseconds, the bleach intensity decay in transient absorption takes place over tens to hundreds of nanoseconds. Further, this decay is slower than the PL decay of the passivated samples. This reinforces the evidence that hole trapping is the dominant PL quenching mechanism in colloidal InP and that electron trapping is slow even on the half microsecond timescale. However, trapping of electrons can be an important quenching mechanism when fast electron traps are present as they are upon addition of methyl viologen. All samples with MV2+ added exhibited total quenching of measurable PL from the nanocrystals, further supporting the interpretation of the TA results as rapid reduction of MV2+ by 1Se electrons in excited InP.

then arises as to whether the highly Stokes-shifted PL in luminescent InP QDs is a band to band process with a hole in the 1Sh state recombining with the 1Se electron. Alternatively, the low energy of the emission could be explained by a trap to band process in which the holes relax to a midgap state and subsequently recombine radiatively with the long-lived delocalized conduction band electrons. If this is the case, emission at early times may contain a significant higher-energy component from electrons combining with untrapped holes. The trapping process should then be resolvable as a shift in emission energy by spectrally resolved fast PL measurements. The result of integrating photon counts from streak camera measurements taken for samples with long PL lifetimes is shown in Figure 3.7c. Photons emitted in the time interval from 0 to 40 ps after excitation show spectral width and Stokes shift that are very similar to those collected in a steady-state PL measurement. The conclusion is that any population transfer of holes must occur faster than the tens of picoseconds time scale. Given the fast kinetics of excited state electron transfer to adsorbed MV2+ seen in sulfide-capped InP QDs, a hole relaxation rate that exceeds the time resolution of the streak camera measurement is plausible.

3.3.4 Femtosecond Excited Carrier Dynamics Accessed by Two-Dimensional Electronic Spectroscopy

To better understand the electronic structure and ultrafast dynamics of InP QDs, we performed two-dimensional electronic spectroscopy (2DES) on both ZnS-shelled InP QDs and as-synthesized InP dots. 2DES is a four-wave mixing technique analogous to TA spectroscopy, but the time difference between the two pump pulses can be controlled.[28, 29] Fourier transforming over this excitation time domain yields an additional axis that reports on the excitation frequency of the sample. With the resolved excitation and detection frequencies, 2DES can track the energy transfer dynamics of the sample from the initial excitation.[30–32] 2DES is also a unique tool to investigate electronic coupling, vibrational coupling, and coherent oscillations between excited states.[33–37] Here we examine the ori-

gin of the broad photoluminescence line shape in InP/ZnS QDs by comparing the spectral features and oscillatory waiting time dynamics of both ZnS-shelled and as-synthesized InP quantum dots using 2DES. Information from 2D spectra will report on the degree of inhomogeneity in the ensemble, reveal details of the excitonic structure of both InP/ZnS and as-synthesized InP QDs, and determine the degree of coupling between different electronic states or state-specific electronicvibrational couplings. Using a similar setup described previously in the literature,[38] we generate 12 fs fwhm laser pulses that we split into three beams arranged in a BOXCARS geometry to perform our 2DES measurements. The three beams are focused on a sample and overlapped at the sample position to produce a four-wave mixing signal that is emitted in a unique phase-matched direction and then heterodyne-detected on a CCD array camera. The first pulse creates a coherence between a ground and excited state, while the second pulse drives the system into a population state or a coherence between different states that locates either on the ground state or the excited state surface. As time is allowed to evolve during the waiting time (T, time difference between the second and the third pulses), this population state can undergo coherent oscillations and incoherent relaxation. Scanning the time delay between pulses 1 and 2, and Fourier transforming over this domain, produces a 2D spectrum. A 2D spectrum is then a frequency-frequency correlation map that relates the excitation pump energy absorbed by the sample with the emitted frequencies detected on the camera after a certain waiting time. Over the course of the 2D experiment the relative timing between pulses can drift slightly since each beam travels a different path in space and any changes, especially those related to beam pointing, can manifest as minute timing errors that impact the phase of the signal detected on the camera. In order to determine the proper phase to be able to assign the features in the 2D spectrum to ground state bleach (GSB), stimulated emission (SE), or excited state absorption (ESA) phenomena, we correct each 2D spectrum through fitting to a separately collected pump probe data set. This phasing process is explained in detail in Appendix A of this thesis.

Two-dimensional electronic spectroscopy provides spectral and dynamic details beyond

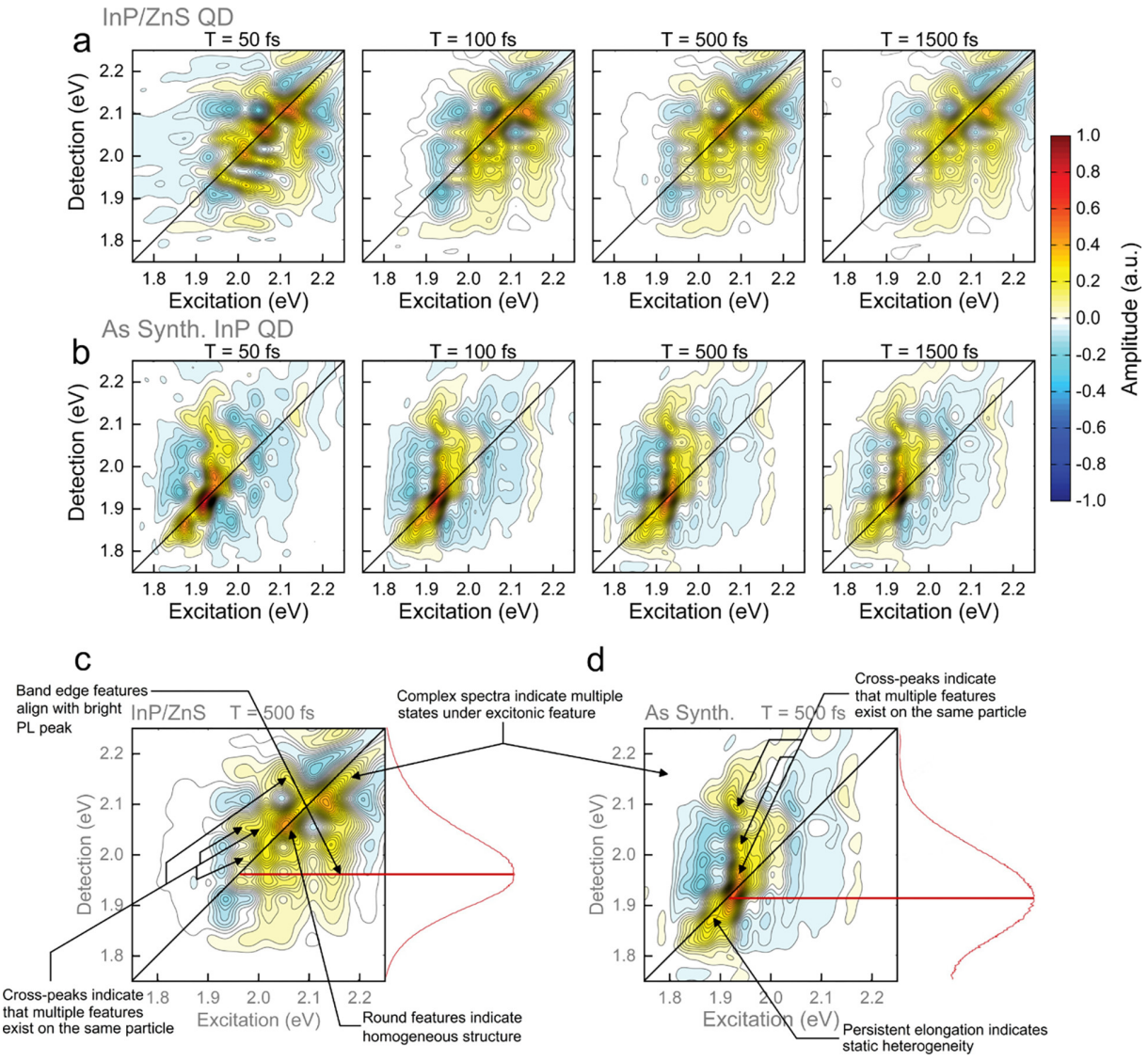

Figure 3.9: (a, b) Time evolution of the 2D spectrum of (a) InP/ZnS QDs and (b) as-synthesized InP QDs at various waiting times (T). (c, d) Annotated real-valued 2DES spectra of (c) InP/ZnS QDs and (d) as-synthesized InP QDs at waiting time T = 500 fs. Relevant points on and off the main diagonal are denoted by red circles and blue squares, respectively. The color map of each spectrum is normalized to the maximum value of each data set. The linear PL spectrum is included in red on the right-hand-side of each 2D spectrum along with a guiding line to illustrate which excitonic states are predominantly responsible for emission. Annotations are included for each spectrum that demonstrate significant features or observations about the spectra that inform our analysis.

that accessible through linear or transient absorption spectroscopies. While the linear absorption and photoluminescence spectra of InP/ZnS quantum dots are generally broad and nearly featureless, the 2D spectra reveal a rich underlying electronic structure, suggesting that there exist distinct electronic states within a complex, multistate exciton manifold (Figure 3.9). There are several contributing factors to this difference between the 2D spectra and the linear spectra. First, in a third order spectroscopy such as 2DES, the signal scales as the transition dipole moment (μ) to the fourth power rather than μ^2 inherent to all linear spectroscopies. Therefore, 2DES is able to resolve distinctive peaks that would be hidden in linear spectra. Additionally, greater resolution is obtained by spreading the signal over two frequency axes. Fast (<500 fs) dynamics in these materials will cause significant broadening in linear spectroscopies that are mitigated by our sub-20 fs time resolution in 2DES. Figure 3.9a,b shows the evolution of 2DES spectra from 50 to 1500 fs for InP/ZnS and as-synthesized InP quantum dots, respectively. In both samples, there is little evolution in spectral shape after the first 200 fs, suggesting that the carrier cooling and trapping occur on very short time scales. Additionally, the two-dimensional line shape of these excitonic features provides information about the degree of homogeneity of the states in the sample that carry the oscillator strength; with defect states, the homogeneity of the state can differ from what is expected on the basis of the nanocrystal size distribution. For example, in Figure 3.10c, many of the features along the main diagonal such as the positive feature at 2.05 eV are circular (Figure 3.9c), indicating a high degree of homogeneity. In contrast, the excitonic features on the main diagonal of the as-synthesized InP QD sample in Figure 3.9d at 1.86 and 1.92 eV are elongated on the diagonal, which is characteristic of static heterogeneity. The difference likely arises not from changes in the size distribution of the QDs but rather the local molecular definition of the bright trap state. Comparing the 2D spectra to the linear PL spectra (shown in red in Figure 3.9c,d), the band edge features in the 2D spectra are the same energy as the PL peak in both samples as expected. However, the as-synthesized InP QD sample has a much lower quantum yield than the InP/ZnS

core-shell sample. Thus, though there is significant amplitude in the as-synthesized InP 2D spectrum, most excitations undergo nonradiative recombination, while the radiative pathways in the InP/ZnS sample are able to outcompete non-radiative processes. Along with the shape and position of the main diagonal features, the presence of cross-peaks in the upper diagonal portion of the spectrum (Figure 3.9c) shows that many of these excitonic states are coupled.[34] This type of upper diagonal feature could be from intradot coupling or interdot (FRET-like) coupling. However, because the time scale of a FRET process is far longer than the waiting times where these crosspeaks occur, and because interdot coupling is expected to be very weak due to the ZnS shell, capping ligands, and nonpolar solvent, it can be concluded that these features are from the coupling of different electronic states within the same QD. Therefore, the broadness of the absorption feature in InP/ZnS quantum dots is primarily due to multiple closely spaced electronic states rather than size-dependent heterogeneity. This agrees with the work of Biadala et al., who proposed an electronic fine splitting structure for InP/ZnS quantum dots that consists of a dark excitonic state and multiple higher-lying bright states.[39] The features in the 2D spectrum of as-synthesized InP QDs show marked differences compared to those of InP/ZnS QDs. In the spectrum of the as-synthesized QDs, the amplitude is focused in two states near 1.88 and 1.93 eV (Figure 3.9d) rather than spread across many states throughout our laser bandwidth. Upper diagonal coupling features exist that are similar to those observed in the spectra of InP/ZnS dots, suggesting that higher-lying excited states similar to the InP/ ZnS sample exist in the as-synthesized InP QD sample; however, the transition dipole strength of these features is far weaker than in the InP/ZnS 2D spectrum. It is possible that lattice and surface defects introduced in the core-shell QDs reduce the symmetry of InP cores, revealing additional fine structure seen in InP/ZnS QDs, and could point toward a route for tuning the splitting in future synthetic work.[40] To study the effect of the shelling process on the InP QD electronic structure further, we turn to Raman spectroscopy and 2DES quantum-beating map analysis.

3.3.5 Structural Characterization by Raman and EXAFS

The increase in Stokes shift upon shelling or HF treatment could either originate from fast hole trapping and a "band to trap" type emission or from an increased degree of excited state reorganization resulting in effectively higher exciton-phonon coupling in the band to band emission.[41] In the case of fast trapping, the relationship between surface chemistry and Stokes shift could be explained by a hypothesis that PL enhancing treatments work by introducing a new radiative recombination route through states that are related to the chemical modification of the structure. If the emission red shift is from a large geometric reorganization in the excited state and a correspondingly large Huang-Rhys parameter, the effect of chemical modification may be to alter the deformation potential of the structure, perhaps by "softening" the crystal surface and introducing new geometric motions that couple to the electronic excitation. The importance of soft deformations in lead salt QDs has been highlighted previously.[42, 43] Because the electron is long-lived in a delocalized state, we should then consider that excited state geometric distortion will be most likely related to distortion of the lattice centered around a localized hole. To clarify the role of phonon coupling and lattice dynamics on the properties of InP QD emission, a Raman scattering study was undertaken. Analysis of the spectral line shapes and overtone intensities reveals that InP samples with broad PLE spectra and bright, red-shifted emission are also characterized by broadened features in their Raman spectra (Figure 3.10a). We further show that this broadening is not due to size effects, surface reconstruction, or appearance of impurity phases. Rather, the broadened Raman features of InP/ZnS core-shells and aerobically HF-treated InP are derived from internal lattice defects. The resulting reduction of crystal symmetry and associated effects on the electronic structure of the quantum dots are responsible for the changes to the Raman spectra and their behavior as emitters. Poorly luminescent InP QDs with no postsynthesis modification show a Raman spectrum that resembles that of bulk single crystals albeit with a size-dependent broadening. The Γ-valley longitudinal optical (LO) and transverse optical (TO) phonon resonances are assigned to

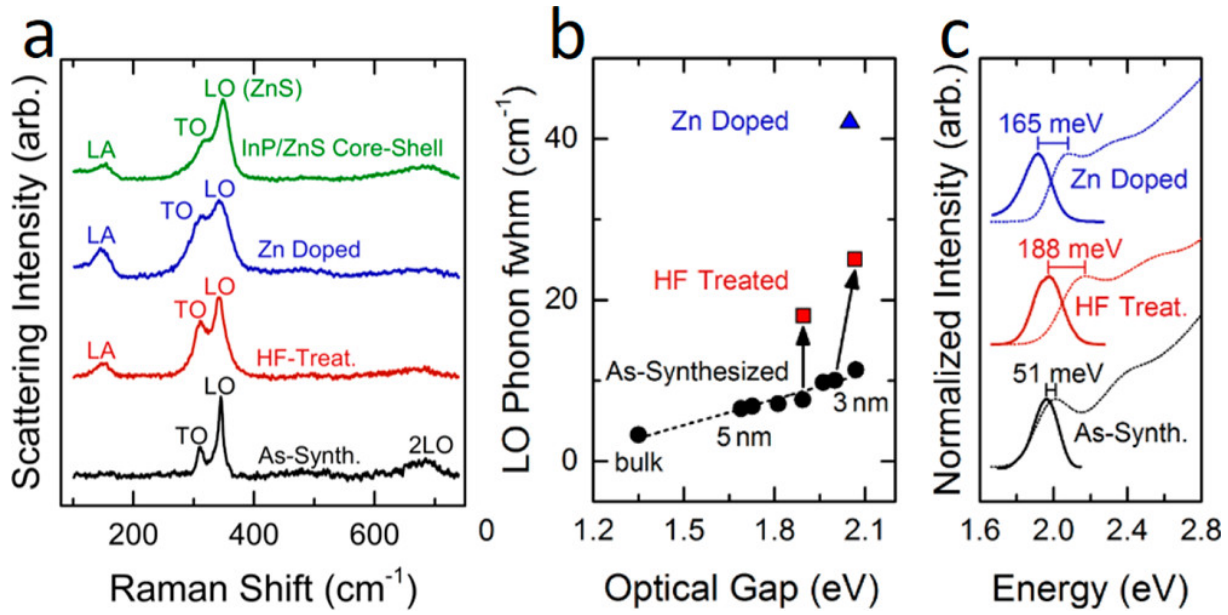

Figure 3.10: (a) Raman spectra of InP as-synthesized, with postsynthetic HF treatment, and Zn-doped from synthesis. Zn-doped and HFtreated material both show broadening of the optical phonon features as well as appearance of scattering from the longitudinal acoustic (LA) mode. (b) Comparison of the longitudinal optical (LO) phonon line widths for the undoped, as-synthesized material and for HFtreated and Zn-doped material. HF treatment and Zn doping by inclusion of ZnCl2 in the synthesis both account for a significant portion of the spectral broadening at a given size and optical gap. Black arrows connect measurements for the same material out of synthesis and after the postsynthesis treatment with HF. (c) Absorption spectra of the three classes of InP and PL under 2.8 eV excitation. Large apparent Stokes shifts are correlated with the lattice disorder related broadening seen in the Raman spectra and also with PLE spectra which show little narrowing compared to ensemble absorption.

the two prominent peaks around 310 and 340 cm^{-1} , respectively. At higher frequencies, spectra show an indistinct feature that can be attributed to three overtones, 2TO, TO + LO, and 2LO. These three features are well-resolved for single crystal InP but produce a single broad scattering signal in the nanocrystalline samples. Raman measurements were also made on luminescent chemically passivated InP samples. InP cores shelled with ZnS show a resonance at 350 cm^{-1} which corresponds to the LO phonon frequency of ZnS and which appears to overlap with the InP LO phonon resonance and obscure it (Figure 3.10a).

We analyze the InP/ZnS core-shell system further by also considering "Zn-doped" InP. For ZnS shelling of InP, it is a common practice to include a Zn precursor in the original InP

core synthesis mixture. Unshelled InP QDs grown from a mixed metal precursor of $InCl_3$ and $ZnCl_2$ are termed here Zn-doped InP. The red shift of PL spectra observed in Zn-doped InP is very similar to that in InP/ZnS core-shells and aerobically HF-treated InP QDs (cf., Figures 3.3a and 3.10c). Chemical analysis by ICP finds that, for our growth conditions with a 1:1 molar ratio of In:Zn, the final atomic ratio is 21:1. Raman spectra of as-synthesized, Zn-doped, and aerobically HF-treated InP QDs are compared in Figure 3.10a. For InP samples that are modified by HF phototreatment, ZnS shelling, or Zn doping, an additional low-frequency mode appears centered at 150 cm^{-1} . Because it appears for both HF phototreated particles and for Zn-doped material, it is highly unlikely that it can be attributed to a motion involving a specific impurity atom. If, for example, In-F bonds were responsible, then the same should not be seen in the ZnS core-shells; if Zn-P bonds were the cause then HF-treated particles with no Zn content should not show the peak in their Raman spectra. The possibility of oxidation resulting in modes from surface oxide phases such as In_2O_3 and $InPO_4$ also fails to account for the observations as no Raman features found in the spectra of these oxides match the 150 cm^{-1} peak seen from modified InP. Rather, the frequency of the new peak matches very well with that of longitudinal acoustic (LA) phonons of InP.[21] The assignment of the low-frequency feature around 150 cm^{-1} to scattering from longitudinal acoustic phonons has important implications. Inelastic scattering from acoustic phonons is not typically observed in nanocrystal samples and is only seen at very low frequencies in bulk crystals due to the acoustic phonon frequencies approaching zero at the Brillouin zone center. The acoustic phonon related feature in HF-phototreated or Zn-doped InP occurs at a frequency corresponding to the acoustic branch density of states maximum rather than near zero frequency.[44] The observed scattering must then be from the equivalent of non-Brillouin zone center modes. The translational symmetry of an ordered lattice imposes the requirement that one phonon scattering occurs from phonons very near the Brillouin zone center in order to satisfy momentum conservation. Without translational symmetry considerations, this selection rule does not apply as lattice motions will no longer be characterized by a definite

wavevector. Broadening of the Raman spectrum and appearance of scattering from modes far from the Brillouin zone center has been observed previously in bulk systems as a characteristic of lattice disorder. The effect of reduced lattice symmetry on Raman scattering is seen clearly in single crystal InP[45–47] and GaAs[45, 48] with ion implantation induced disorder. Ion bombarded samples show pronounced broadening of the optical phonon resonances as well as the appearance of new features. The new peaks originate from scattering involving the disordered material equivalent of what would, in the ordered case, be phonons that are far from the Brillouin zone center. In the limit of high disorder, the ion bombardment studies find a scattering intensity spectrum that closely resembles the total phonon density of states of the corresponding ordered material. The appearance of this "density-of-states-like" Raman spectrum indicates that a degree of lattice disorder that is sufficient to drastically alter Raman scattering behavior may not strongly perturb the phonon density of states. This type of disorder related activation of non-Brillouin zone center Raman scattering seems to describe the spectra of luminescent nanoparticles quite well. In a comparison of untreated and aerobically HF-treated InP, the Raman spectrum differs in four notable ways: the appearance of the LA phonon scattering feature, a relative increase in the intensity of the TO phonon peak, broadening of these features by a factor of 2 or more, and a lessening of the optical phonon overtone scattering intensity. All of these changes match those seen upon ion bombardment of single crystals including the weakened overtones. Concomitant with the shift to a density-of-states-like Raman spectrum, ion bombardment disordered III-V materials exhibit a decrease in overtone intensities with increasing ion dose.[47] This provides a ready explanation for the weakening of overtone intensity seen when comparing luminescent HF photoetched InP particles to untreated particles of the same size (Figure 3.11).

Rather than tracking strength of electron phonon coupling of the resonant excitation, the change to the overtone intensity indicates a reduced lattice symmetry. The degree of disorder required to produce such a suppression of a selection rule is apparently relatively small. Measurements of powder X-ray diffraction (PXRD) of InP QDs as-synthesized, HF-

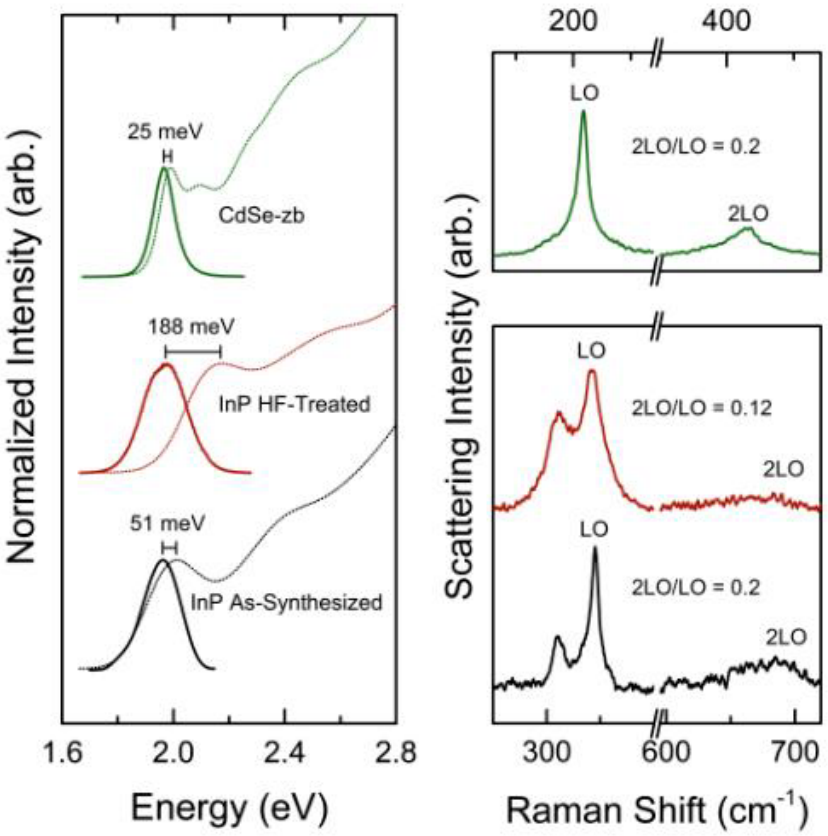

Figure 3.11: Left, absorption and PL spectra of InP and CdSe nanocrystals. The InP sample that is made luminescent by HF treatment has a substantially greater apparent Stokes shift of 188 meV compared to either the InP as– synthesized or to the CdSe. Right, a comparison of Raman fundamental to first LO phonon overtone for the same samples.

treated, or Zn-doped all yield very similar diffraction patterns. The PXRD peak widths and extracted Scherrer sizes for these different types of InP QDs are all comparable among particles with similar first exciton energy. Additionally, the PXRD data does not show evidence of impurity phases present above the detection limit of 1% in any of the measured samples. We might expect to find InF_3, $InPO_4$, In_2O_3, or $In(PO_3)_3$ phases in material that is illuminated in the presence of HF and air, but none are evident. Similarly, in Zn-doped InP there is no significant impurity phase of tetragonal Zn_3P_2. Only zinc blende InP is found, albeit with diffraction peaks shifted slightly to higher angles due to lattice contraction. Thus, the disorder observed in Raman spectroscopy likely originates from point defect sites such as vacancies, substitutions, and interstitials that result in an effectively reduced symmetry. A similar kind of disorder was seen in ion bombarded single crystals.[45–47] In the case of a nanocrystal, even if it is perfectly ordered within, there is no translational symmetry comparable to a bulk single crystal where the lattice extends approximately infinitely. Typical colloidal InP QDs have diameters of 3-5 nm compared with a lattice constant of 0.59 nm. As structures approach the scale of a unit cell, it is important to carefully consider size effects in interpreting nanocrystal Raman scattering. A size series of InP Raman spectra from material all from the same synthetic batch indeed shows the expected broadening of Raman features with decreasing crystal radius. Plotting the LO phonon line width vs optical gap for this series gives an empirical linear relation shown in Figure 3.10b. Here it can be clearly seen that treatment by illumination in the presence of HF and air results in a broadening of the LO phonon line that is far greater than what can be attributed to size effects resulting from a reduction of the radius. The quantum dots doped with Zn show even larger LO phonon line broadening at the same size. In both cases, the Raman line broadening is accompanied by a pronounced increase in Stokes shift of the emission (Figure 3.10c) pointing to a link between the vibrational properties of InP QDs and their properties as emitters. For Zn-doped QDs the apparent reduction of lattice symmetry is easily understandable; Zn^{2+} ions incorporated at substitutional or interstitial sites are expected to introduce internal disorder.

Phototreatment by HF, on the other hand, is expected on the basis of previous studies[16, 25, 26] to act on the crystal surface. This raises the question of whether the changes seen in Raman spectra of HF-treated InP can be explained by surface effects alone or if there is an implied role of disorder in the interior of the QDs. In the case of a surface localized effect of the treatment, we expect that surface phonon modes will be predominantly affected. Fitting of the optical phonon fundamental region reveals that the changes to the Raman spectra seen upon treatment extend to the bulk derived LO and TO motions and cannot be described by a change to the surface vibrational structure alone. The surface optical phonon (SO) scattering contribution is resolvable in the fits but does not show pronounced variation with chemical treatment. This implies that putative surface treatments affect vibrational structure of the quantum dots beyond the surface alone. We can gain some insight into the way that luminescence enhancing modifications can result in defected nanocrystal interiors by reducing them to their component parts and examining the effects of each individually. In the case of ZnS shelling, the process can be broken down into the effects of Zn and S separately. When as-synthesized InP cores are stirred at 270 C with trioctylphosphine sulfide (TOP-S), the sulfur precursor for shell growth, there is little observable change in the Raman spectrum. A more aggressive sulfidation of the surface is possible by exchange of the long chain organic ligands on as-synthesized InP QDs for compact S^{2-} ligands resulting in electrostatically stabilized colloids soluble in polar solvents. This ammonium sulfide treatment has been thoroughly investigated on surfaces of bulk InP where it has been found to induce surface reconstruction and alter surface electronic properties upon annealing.[49–52] Sulfide stabilized InP quantum dots show little change in the Raman spectrum even after a 350 C anneal. An analogous experiment to test the effect of surface Zn^{2+} yields a similar result: undoped InP cores that are exchanged to $ZnCl_2$ capping ligands also do not show significant broadening after annealing.

Figure 3.12 summarizes these results and also shows Zn-doped InP-capped with its native oleylamine ligands for comparison. Postsynthetic Zn^{2+} and S^{2-} treatments are both

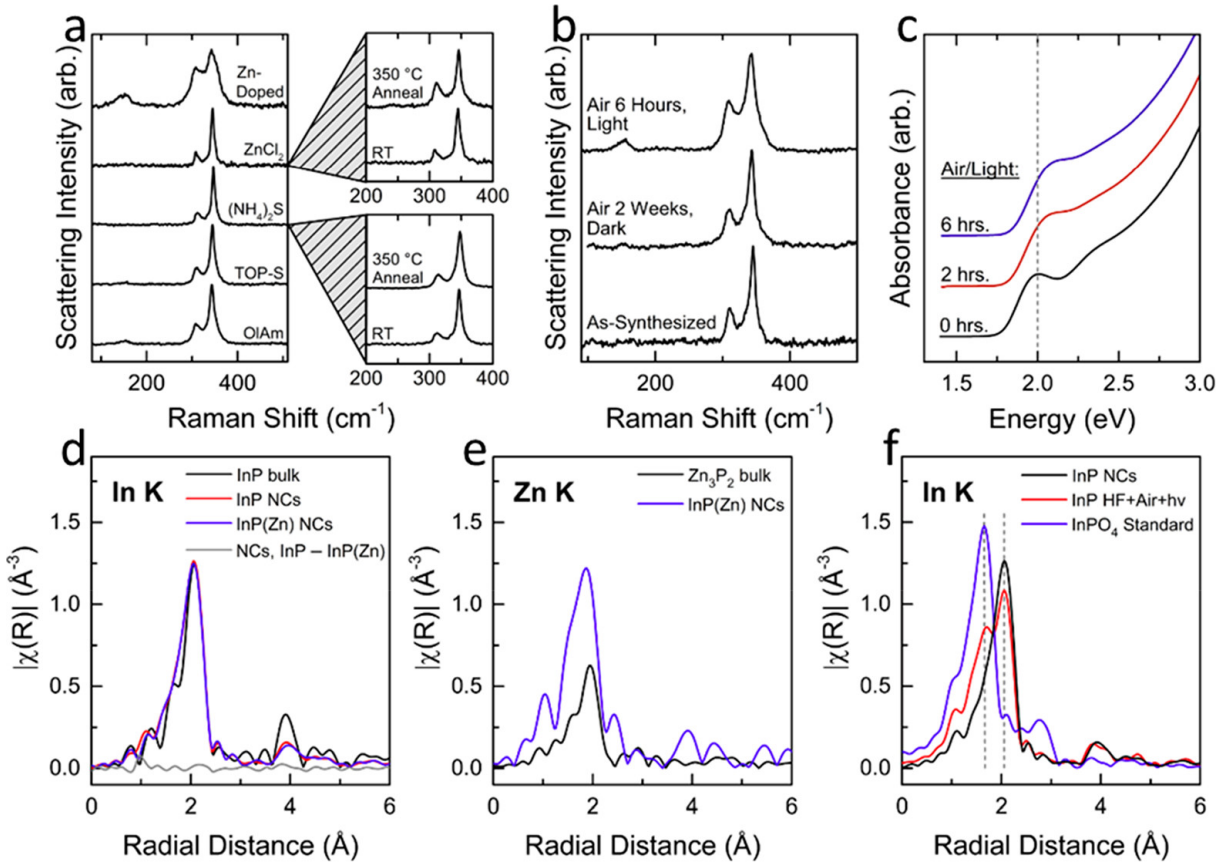

Figure 3.12: (a) Raman spectra for as-synthesized InP cores capped with native oleylamine ligands (OlAm), trioctylphosphine sulfide (TOP-S), ammonium sulfide, and zinc chloride. The Zn-doped spectrum shows data for oleylamine-capped InP QDs synthesized from a mixed InCl3/ZnCl2 precursor. (b) Raman spectra showing the same particles fresh and exposed to air with and without light. (c) Absorption spectra showing the effect of aerobic illumination of InP colloids. (d-f) R-space representations of In and Zn K-edge EXAFS.

expected to have pronounced effects on the nanocrystal surfaces but likely not on the interior. So, the small effect of surface treatments on the Raman spectrum is consistent with the hypothesis that internal disorder is a necessary condition to observe broadened phonon lines. That only the Zn-doped material shows significant changes to its Raman spectrum is strong evidence that the signatures of disorder are related to internal defects. While InP passivation by dilute HF and illumination in air has been previously considered as a treatment which affects only nanocrystal surfaces, the fact that signatures of internal disorder appear in Raman spectra of treated InP implies that the effect goes beyond the surface. Separating the HF, illumination, and air exposure elements of the treatment, we find that disorder appears when InP is exposed to light and air simultaneously (Figure 3.12b,c). This can be explained by a hypothesis that photo-oxidation induces intercalation of interstitial O^{2-} ions into the lattice to produce a structural change that goes beyond the surface. This idea is consistent with previous observations of photo-oxidation of InP nanowires[53] and supported by a computational study[54] which found that oxygen atoms favorably insert into the InP lattice to form In-O-P bridges. Studies of Zn-doped and HF-treated InP by extended X-ray absorption fine structure (EXAFS) corroborate the assignment of lattice disorder inducing species inferred by the Raman study. We find evidence for substitutional Zn^{2+} ions on In^{3+} sites in Zn-doped InP and interstitial O^{2-} in aerobically HF-treated InP. Data from the In K-edge represented in R-space, Figure 3.12d, shows identical coordination environments around In atoms in both doped and undoped InP. This indicates that Zn-doped material retains a tetrahedral four phosphorus atom coordination environment around indium and that there is no evidence of reduction in crystallinity upon Zn doping. It further argues that Zn inside the quantum dots should be on substitutional rather than interstitial sites as interstitial Zn^{2+} would appear in the first coordination sphere of neighboring In atoms. Data from the Zn K-edge, Figure 3.12e, shows that Zn dopant atoms are characterized by bonds to phosphorus atoms in their first coordination spheres. If Zn were significantly concentrated on the surface of the material, we would expect to see evidence in EXAFS of short Zn-N

bonds from coordination to the oleylamine capping ligands. This is not the case, and the observed Zn coordination provides strong support for the conclusion of the Raman study: Growth of InP in the presence of a Zn salt results in Zn trapped inside the crystallites. Examination of the indium K-edge data for aerobically HF-treated InP, Figure 3.12f, finds further support for the conclusions of the Raman study. Compared to untreated InP, the luminescent material is oxidized and shows that a significant amount of In-O bonds form as a result of the treatment. Fitting this data by considering In-P and In-O scattering paths finds that there are roughly two In-O bonds for every three In-P bonds. Given the large number of oxygen atoms, it is unlikely that oxidation is confined only to the surface. In agreement with the hypothesis motivated by the Raman data, EXAFS shows that photo-oxidation of InP leads to intercalation of O^{2-} ions deep into the quantum dots.

3.3.6 Exciton-Phonon Coupling Probed by 2DES Quantum-Beating Maps

To further investigate the broad PL from InP/ZnS QDs, we analyzed quantum-beating maps of our 2D spectra. Following a point in a 2D spectrum over the waiting time results in a trace that records both the relaxation dynamics and coherent oscillations (Figure 3.13). By subtracting a single exponential or multiexponential fitting function from the waiting time trace, we are able to isolate the coherent oscillatory dynamics. This residual is then Fourier transformed to yield a power spectrum. A quantum-beating map can be generated by performing this analysis on each point in a 2D spectrum, and plotting the intensity of the resultant power spectrum for a particular beating frequency (ωT), across the entire 2D spectrum. These beating maps depict where on the 2D spectrum a particular oscillatory mode is present, allowing us to link the system phonon modes with the electronic state(s) to which they are coupled.[55–57]

Figure 3.14a,b shows the quantum-beating maps for ZnS-capped InP QDs and as-synthesized InP QDs, respectively, taken at 43 meV, revealing the LO phonon energy of InP and ZnS. The beating map of InP/ZnS QDs at this energy has a prominent feature that

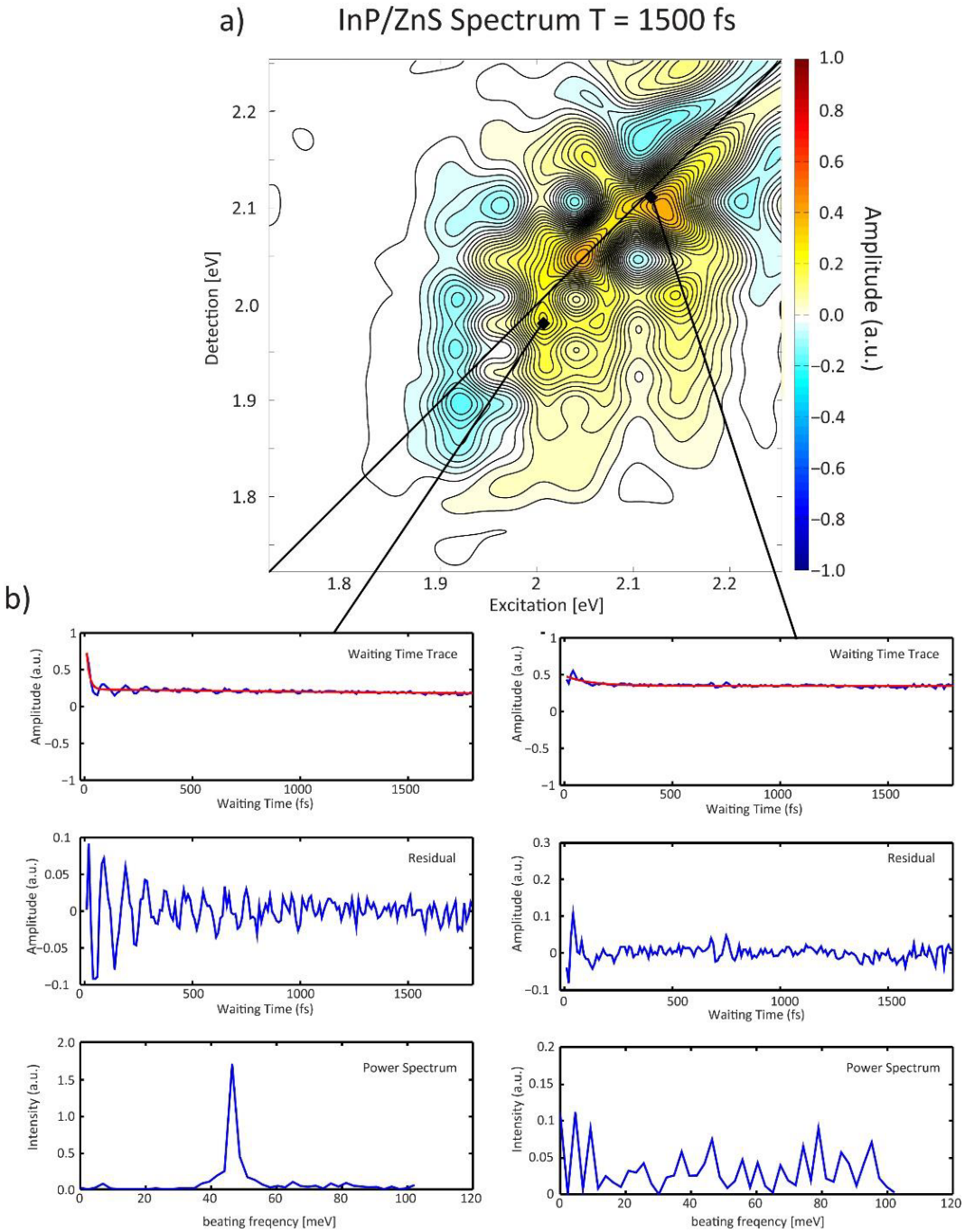

Figure 3.13: a) 2D spectrum of InP/ZnS QDs at a waiting time of 1500 fs. Two diamonds mark the points from which the waiting time traces in b) are taken. b) Top panel: Waiting time traces at two different points in the 2D spectrum (blue) and bi-exponential fits to the traces (red). Middle panel: Residual after subtracting the bi-exponential fit from the waiting time traces in the top panel of b). Bottom panel: Power spectra of the residuals in the middle panel showing oscillatory modes coupling to the given points in the 2D spectrum.

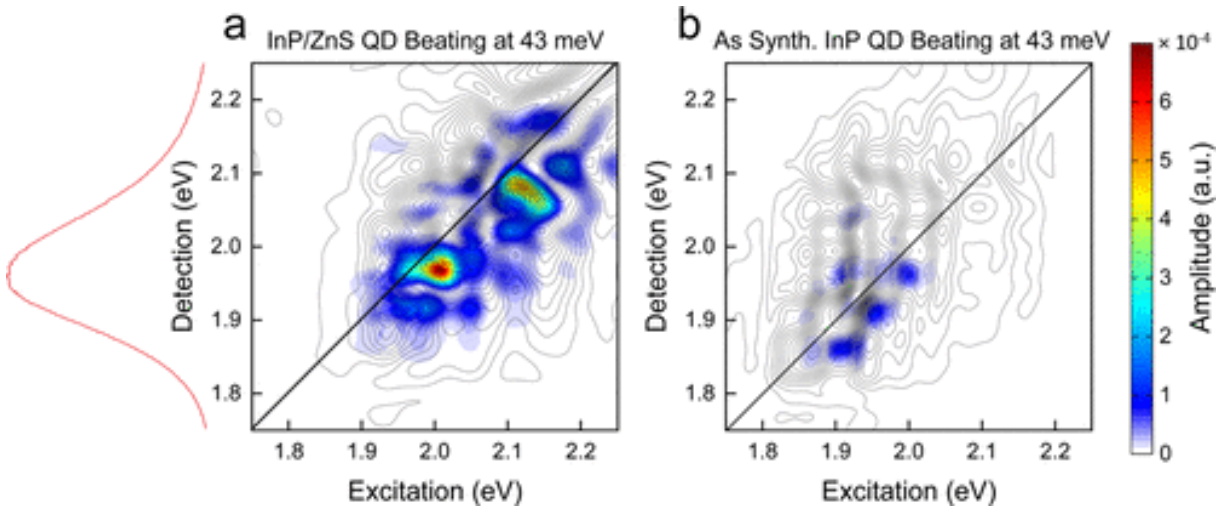

Figure 3.14: Quantum-beating maps of (a) InP/ZnS QDs and (b) as-synthesized InP QDs taken at 43 meV reveal exciton-LO-phonon coupling. Contour lines of the real-valued 2D spectrum for each sample at 750 fs are overlaid to guide the reader. Additionally, the linear PL spectrum of InP/ZnS QDs is plotted in red on the left-hand side of the InP/ZnS QD beating map to show that the maximum of the InP/ZnS beating map corresponds to the peak of the linear PL.

notably aligns with the peak of the PL band at 1.99 eV (Figure 3.14a includes the linear PL spectrum as a guide). Therefore, upon excitation into the bright electronic states of InP/ZnS QDs at 1.95 and 2.03 eV (main diagonal), the exciton couples to the lattice vibration which contributes to photoluminescence line broadening in colloidal quantum dots at room temperature.[58] As-synthesized InP (Figure 3.14b) does not show significant intensity in the 2D beating map, though a sharp LO feature appears in the Raman spectroscopy. This observation indicates that only the states arising from fine splitting by incorporating disorder into the lattice couple significantly to the LO phonon. It is possible that the coupling is influenced both by the ZnS phonon mode and the InP LO phonon mode; regardless, the dark band-edge states show no apparent coupling in the InP/ZnS 2D beating map. Finally, there is also a coupling peak at (2.12, 2.08 eV) on the InP/ZnS beating map. This may correspond to a secondary bright state as noted in the literature that further contributes to photoluminescence line broadening in InP/ZnS quantum dots.[39] Taken together, these 2D quantum-beating maps show that the bright electronic states of InP/ZnS quantum dots

couple more strongly to lattice vibrations than assynthesized InP QDs, which is expected for emission from localized defect states introduced during the shelling process, in turn leading to PL line broadening at room temperature.

3.3.7 Computational Insights into Electronic Structure and Impurity Levels of InP Quantum Dots

Combined, the spectroscopic, EXAFS, and Raman studies find that structural disorder in the form of impurity atom point defects is correlated with the appearance of broad red-shifted emission. The question then remains, how do these structural defects alter the electronic and optical properties of the material? We see from our spectroscopic investigations (Figure 3.7) that electrons remain in a delocalized 1Se state on the time scale of emission and that non-radiative recombination results from hole trapping. Further, we find from the 2DES study that the red-shifted radiative recombination in Zn-doped InP/ZnS core-shells occurs from a more strongly LO phonon-coupled state. Strengthened exciton coupling to the LO motion of InP suggests a spatial separation of electron and hole in the emissive state. Given the long lifetime of delocalized electrons, the plausible explanation is that the red-shifted and persistently broad emission occurs through a state with the hole localized in a defect atom related state that is ∼100 meV above the valence band edge. To further test this hypothesis, we carried out a series of DFT calculations on a model nanoparticle with an $In_{92}P_{68}$ core (∼1.9 nm; In/P ratio 1.35). The surface was passivated with 72 fluorine atoms providing a clean band gap with the density of electronic states (DOS) with band gap energy Eg = 0.92 eV. The magnitude of the band gap energy is underestimated here compared to the experimental value; hence, we focus on comparing trends in electronic structure under changing surface passivation or introduction of defects. As an example, we found qualitatively similar electronic structure for $In_{92}P_{68}$ cores passivated with a mixture of acetate and hydroxyl ligands. This result supports our experimental findings that defect related emission seen for aerobically HF-treated InP is not a result of surface fluorination but is caused by subsurface

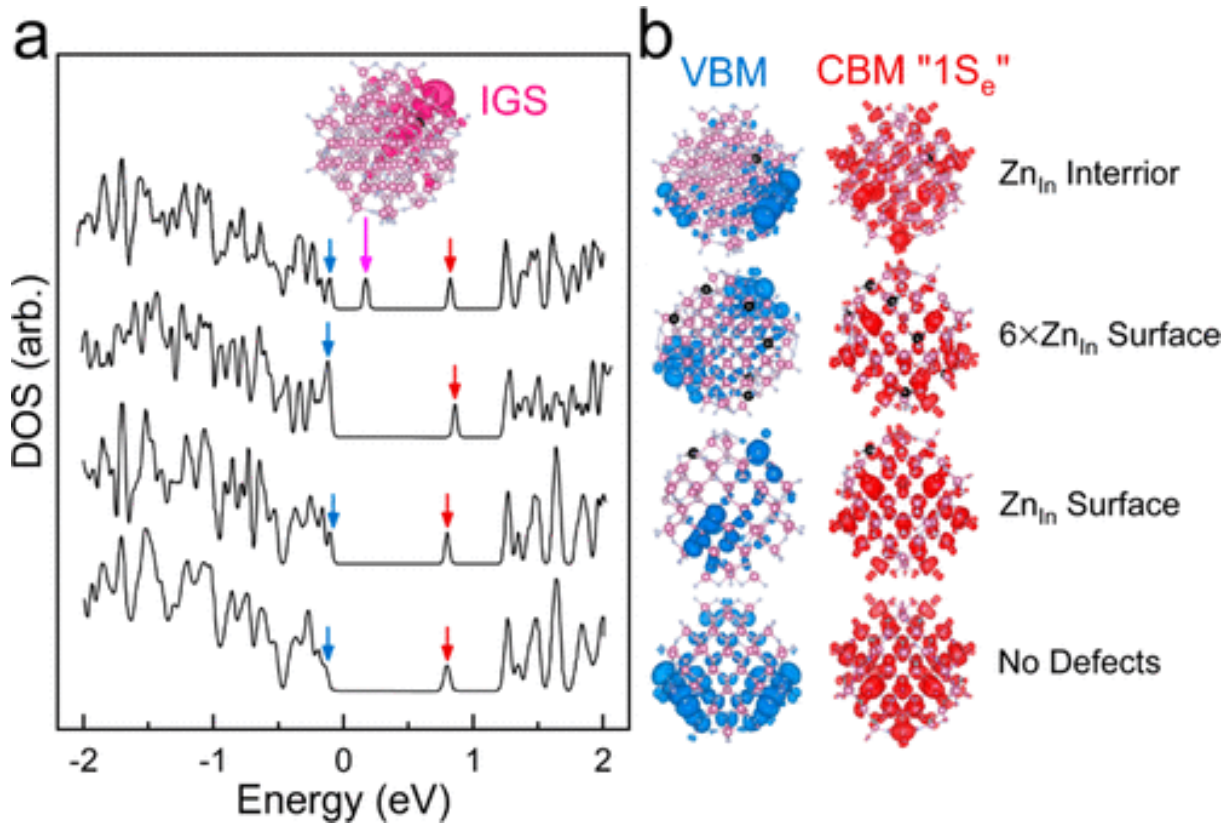

Figure 3.15: (a) Offset density of states traces calculated for $In_{92}P_{68}$ with the following substitutional ZnIn defects from top to bottom: single interior Zn, 6 Zn atoms on surface, single Zn on surface, and no substitutions. The valence band maxima (VBM) and conduction band minima (CBM) are marked with blue and red arrows. The "in-gapstate" generated by the interior Zn substitution is marked with a magenta arrow and depicted on the inset contour plot. (b) Contour plots visualizing the VBM and CBM states marked by blue and red arrows in part a. Atoms are colored according to type: In (pink), P (gray), F (blue), and Zn (black).

defects that are introduced during the passivation process. Next, we considered the effect of substitutional ZnIn defects in which selected In atoms in F-passivated $In_{92}P_{68}$ were replaced by Zn atoms. We studied the changes introduced by such substitutions to the energy and spatial probability density of CBM and VBM states of Zn-doped InP QDs (Figure 3.15).

Substitutions at both surface and interior sites have a minor effect on the CBM energy and preserve the delocalized 1Se state across different types of surface or internal ZnIn defects. However, valence band states are significantly perturbed by ZnIn substitutions with differing effects for surface and interior Zn dopants. Site-dependent effects are seen in Figure 3.15 in

both the DOS traces at energies near the VBM, and also in the contour plots of the VBM states. Generally, surface site Zn atoms increase the localization of the VBM and thus decrease VBM-CBM overlap in the QD interior, likely causing an increase in radiative emission lifetimes. The specific effects of surface ZnIn substitutions differ depending on which site was substituted meaning that an ensemble of Zn-doped InP will be composed of quantum dots which have differing absorption and emission profiles even in the absence of polydispersity in particle size. The resulting spectral broadening originates from chemical inhomogeneity and cannot be eliminated by synthetic optimizations to narrow size distribution. Interior ZnIn substitutions produce an additional form of electronic structure inhomogeneity. In addition to perturbing the valence band electronic structure, interior Zn dopants produce an in-gap-state (IGS) located above the VBM. As seen in the inset contour plot in Figure 3.15, this IGS has orbital density localized around the substituted Zn atom and an energy ranging between 50 and 250 meV above the VBM depending on which interior In atom is substituted. The appearance of such a state is expected given that Zn is a well-known p-type dopant used in commercial bulk InP wafers where it acts as an electron acceptor by introduction of a state above the valence band edge. For the purposes of quantum dot emitters, this variable energy IGS contributes further to broad ensemble emission by introducing a new radiative emission pathway. Following excitation of an electron-hole pair, the IGS can capture the hole, which subsequently recombines with the electron remaining in the 1Se-like CBM state. One effect of this CBM to IGS emission pathway can be to boost PL quantum yield by competing with nonradiative hole trapping at the quantum dot surface. Additionally, it provides an explanation for experimentally observed dot-to-dot variations of the apparent Stokes shift and strongly phonon-coupled emission.

3.4 Conclusions

In summary, the data point to an important role of chemical disorder in the optical properties of InP QDs. The apparent Stokes shift of the photoluminescence varies depending on chem-

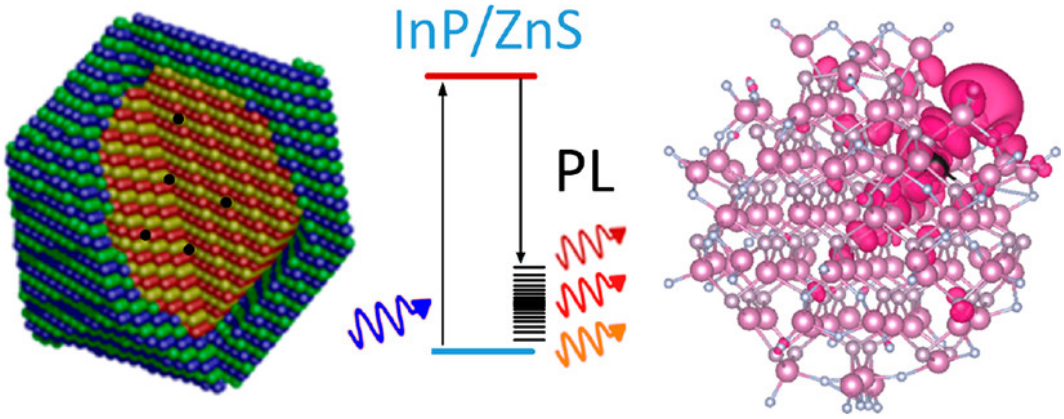

Figure 3.16: Lattice defects in the InP/ZnS quantum dot crystal lattice (left) introduce emissive shallow hole trap states in the electronic structure (center). These localized trap states (right) show electron-phonon coupling to lattice vibrations, which can help to explain the broad emissive lineshapes of InP/ZnS quantum dots.

istry suggesting that the electronic states that are active in emission also vary. Given that colloids with different emission red shifts show similar properties as absorbers, this implies that the emission red shift is due to an electronic relaxation following absorption of band-edge light. Photoluminescence excitation spectra show that the deeply red-shifted emission is coupled to a broad action spectrum with washed out features and with an absorption onset shifted substantially to the blue compared to the detected emission. Energy dissipation between absorption and emission in the form of electron relaxation to a sub-band-edge state was ruled out by a series of transient absorption experiments.

There are two likely remaining mechanisms to explain the red shift. One is energy loss by shallow trapping of the valence band holes to a state which can combine radiatively with delocalized conduction band electrons. A second is a large geometric reorganization of the excited state resulting in strengthened electron-phonon coupling and emission to a vibrationally hot electronic ground state. These two mechanisms are related in our model due to the electron-phonon copuling observed in the emissive shallow trap state in InP/ZnS quantum dots. Shallow trapping is likely to be accompanied by an increased degree of localization of the hole which would result in a spatial separation between it and the delocalized electron. The resulting electric dipole induces a geometric distortion along the optical phonon

coordinate of motion of the holetrapped excited state. Thus, localization of the hole due to trapping can produce a stronger electron-phonon coupling. Likely, the red shift in emission produced when InP nanoparticles are made brightly luminescent is due to a combination of the two effects which explains the persistently broad emission line width of typical high-quantum-yield InP samples. Raman experiments reveal disorder activated phonon modes and give us some clue as to the chemical nature of the lowered symmetry. A common property of interstitial O^{2-}, S^{2-}, and F^{-} and substitutional Zn^{2+} is that all will be expected to p-type dope III-V semiconductors by charge balance arguments. In a quantum dot, the doping effect of such impurities is likely to be compensated by the presence of other point defects such as vacancies rather than by the presence of free holes. The net effect is then to produce filled states above the valence band edge that are expected to act as exactly the shallow hole traps implied by the luminescence and transient absorption experiments. Given that HF-etched InP QD emitters behave similarly to the InP/ZnS core-shells in PL, PLE, and Raman measurements, we find it likely that there are multiple types of lattice defects that can all produce similar results. The hypothesis consistent with all of the data is that the PL enhancing modifications of doping InP with Zn^{2+}, shelling with II-VI materials, and etching with HF in aerobic conditions and illumination all play a double role of passivating surface sites and installing shallow hole traps. The radiative process combining free conduction band electrons with trapped holes then enhances PL quantum yield by providing an additional emissive recombination pathway competing with the expected band to band process. The end result is a red-shifted and persistently broad emission profile that complicates efforts to apply InP colloidal quantum dots, for example, as phosphors emitting saturated primary colors. In detailing the obstacles to achieving narrow emitting, stable, and bright InP, we also hope to point toward a future direction to overcome them. One class of disorder, substitutional Zn^{2+}, can be addressed by II-VI shelling of pure InP cores that are grown before addition of the Zn shelling precursor. This is unlikely to provide a complete solution to the problem as the large lattice mismatch between InP and ZnS makes

interfacial disorder likely, and strain related imperfections or diffusive mixing at a III-V/II-VI interface leads to doping and the appearance of carrier localizing states. Our studies of the HF etched InP system strengthen this point. In this system, there is no disorder related to Zn impurities and yet we observe outwardly similar behavior to ZnS shelled material. The most promising route to solving the problem would be to avoid the use of group II and group VI species altogether. InP quantum dots passivated by shells of higherband-gap III-V materials, an InP/InGaP/GaP type structure for example, should avoid the problem of emission through impurity atom related states. Developments in synthetic methods for the InP core that avoid oxidation during synthesis should also allow for a way to avoid oxide induced midgap states. With the correct synthetic protocol and passivation scheme, it should be possible for III-V-based quantum dots to emit from band to band recombination with reduced phonon coupling. Future steps in this direction may prove necessary for achieving comparable performance to CdSe in nontoxic III-V materials.

3.5 Acknowledgements

This work was supported by NSF under award number DMR1611371, by NSF DMREF Program under awards DMR1629601 and DMR-1629383, and by the Department of Defense (DOD) Air Force Office of Scientific Research under grant number FA9550-15-1-0099. M.H. was supported by the University of Chicago Materials Research Science and Engineering Center funded by NSF under award DMR1420709. D.V.T. acknowledges support from Samsung Global Research Outreach Program on New Materials. Sector 20 facilities at the Advanced Photon Source, and research at these facilities, are supported by the U.S. Department of EnergyBasic Energy Sciences, the Canadian Light Source, and its funding partners, and the Advanced Photon Source. MRCAT operations are supported by the Department of Energy and the MRCAT member institutions. Use of the Advanced Photon Source and Center for Nanoscale Materials, an Office of Science User Facilities operated for the U.S. Department of Energy (DOE) Office of Science by Argonne National Laboratory, was supported by the U.S.

DOE under Contract No. DE-AC02-06CH11357. The authors thank Dr. Karen Watters for scientific editing of the manuscript.

REFERENCES

[1] X. L. Dai, Y. Z. Deng, X. G. Peng, and Y. Z. Jin. "Quantum-Dot Light-Emitting Diodes for Large-Area Displays: Towards the Dawn of Commercialization". In: *Advanced Materials* 29.14 (2017). ISSN: 0935-9648.

[2] L. Protesescu, S. Yakunin, M. I. Bodnarchuk, F. Krieg, R. Caputo, C. H. Hendon, R. X. Yang, A. Walsh, and M. V. Kovalenko. "Nanocrystals of Cesium Lead Halide Perovskites (CsPbX3, X = Cl, Br, and I): Novel Optoelectronic Materials Showing Bright Emission with Wide Color Gamut". In: *Nano Letters* 15.6 (2015), pp. 3692–3696. ISSN: 1530-6984.

[3] J. S. Manser, J. A. Christians, and P. V. Kamat. "Intriguing Optoelectronic Properties of Metal Halide Perovskites". In: *Chemical Reviews* 116.21 (2016), pp. 12956–13008. ISSN: 0009-2665.

[4] S. Kim, T. Kim, M. Kang, S. K. Kwak, T. W. Yoo, L. S. Park, I. Yang, S. Hwang, J. E. Lee, S. K. Kim, and S. W. Kim. "Highly Luminescent InP/GaP/ZnS Nanocrystals and Their Application to White Light-Emitting Diodes". In: *Journal of the American Chemical Society* 134.8 (2012), pp. 3804–3809. ISSN: 0002-7863.

[5] J. Cui, A. P. Beyler, L. F. Marshall, O. Chen, D. K. Harris, D. D. Wanger, X. Brokmann, and M. G. Bawendi. "Direct probe of spectral inhomogeneity reveals synthetic tunability of single-nanocrystal spectral linewidths". In: *Nature Chemistry* 5.7 (2013), pp. 602–606. ISSN: 1755-4330.

[6] V. Chandrasekaran, M. D. Tessier, D. Dupont, P. Geiregat, Z. Hens, and E. Brainis. "Nearly Blinking-Free, High-Purity Single-Photon Emission by Colloidal InP/ZnSe Quantum Dots". In: *Nano Letters* 17.10 (2017), pp. 6104–6109. ISSN: 1530-6984.

[7] D. V. Talapin, S. Haubold, A. L. Rogach, A. Kornowski, M. Haase, and H. Weller. "A novel organometallic synthesis of highly luminescent CdTe nanocrystals". In: *Journal of Physical Chemistry B* 105.12 (2001), pp. 2260–2263. ISSN: 1520-6106.

[8] D. Franke, D. K. Harris, L. S. Xie, K. F. Jensen, and M. G. Bawendi. "The Unexpected Influence of Precursor Conversion Rate in the Synthesis of III-V Quantum Dots". In: *Angewandte Chemie-International Edition* 54.48 (2015), pp. 14299–14303. ISSN: 1433-7851.

[9] Y. Li, C. D. Pu, and X. G. Peng. "Surface activation of colloidal indium phosphide nanocrystals". In: *Nano Research* 10.3 (2017), pp. 941–958. ISSN: 1998-0124.

[10] L. S. Xie, Y. Shen, D. Franke, V. Sebastian, M. G. Bawendi, and K. F. Jensen. "Characterization of Indium Phosphide Quantum Dot Growth Intermediates Using MALDI-TOF Mass Spectrometry". In: *Journal of the American Chemical Society* 138.41 (2016), pp. 13469–13472. ISSN: 0002-7863.

[11] D. C. Gary, M. W. Terban, S. J. L. Billinge, and B. M. Cossairt. "Two-Step Nucleation and Growth of InP Quantum Dots via Magic-Sized Cluster Intermediates". In: *Chemistry of Materials* 27.4 (2015), pp. 1432–1441. ISSN: 0897-4756.

[12] O. I. Micic, C. J. Curtis, K. M. Jones, J. R. Sprague, and A. J. Nozik. "Synthesis and Characterization of InP Quantum Dots". In: *Journal of Physical Chemistry* 98.19 (1994), pp. 4966–4969. ISSN: 0022-3654.

[13] W. S. Song, H. S. Lee, J. C. Lee, D. S. Jang, Y. Choi, M. Choi, and H. Yang. "Amine-derived synthetic approach to color-tunable InP/ZnS quantum dots with high fluorescent qualities". In: *Journal of Nanoparticle Research* 15.6 (2013). ISSN: 1388-0764.

[14] R. Xie, D. Battaglia, and X. Peng. "Colloidal InP nanocrystals as efficient emitters covering blue to near-infrared". In: *Journal of the American Chemical Society* 129.50 (2007), pp. 15432–+. ISSN: 0002-7863.

[15] M. D. Tessier, D. Dupont, K. De Nolf, J. De Roo, and Z. Hens. "Economic and Size-Tunable Synthesis of InP/ZnE (E = S, Se) Colloidal Quantum Dots". In: *Chemistry of Materials* 27.13 (2015), pp. 4893–4898. ISSN: 0897-4756.

[16] D. V. Talapin, N. Gaponik, H. Borchert, A. L. Rogach, M. Haase, and H. Weller. "Etching of colloidal InP nanocrystals with fluorides: Photochemical nature of the process resulting in high photoluminescence efficiency". In: *Journal of Physical Chemistry B* 106.49 (2002), pp. 12659–12663. ISSN: 1520-6106.

[17] O. I. Micic, H. M. Cheong, H. Fu, A. Zunger, J. R. Sprague, A. Mascarenhas, and A. J. Nozik. "Size-dependent spectroscopy of InP quantum dots". In: *Journal of Physical Chemistry B* 101.25 (1997), pp. 4904–4912. ISSN: 1089-5647.

[18] L. Li and P. Reiss. "One-pot synthesis of highly luminescent InP/ZnS nanocrystals without precursor injection". In: *Journal of the American Chemical Society* 130.35 (2008), pp. 11588–+. ISSN: 0002-7863.

[19] S. Ithurria and D. V. Talapin. "Colloidal Atomic Layer Deposition (c-ALD) using Self-Limiting Reactions at Nanocrystal Surface Coupled to Phase Transfer between Polar and Nonpolar Media". In: *Journal of the American Chemical Society* 134.45 (2012), pp. 18585–18590. ISSN: 0002-7863.

[20] V. I. Klimov. "Spectral and dynamical properties of multilexcitons in semiconductor nanocrystals". In: *Annual Review of Physical Chemistry*. Vol. 58. Annual Review of Physical Chemistry. 2007, pp. 635–673. ISBN: 978-0-8243-1058-5.

[21] R. M. Feenstra and S. W. Hla. "Physics of Solid Surfaces". In: *Physics of Solid Surfaces*. Vol. 45A. Springer Materials. 2015. ISBN: 978-3-662-47735-9.

[22] A. A. Guzelian, J. E. B. Katari, A. V. Kadavanich, U. Banin, K. Hamad, E. Juban, A. P. Alivisatos, R. H. Wolters, C. C. Arnold, and J. R. Heath. "Synthesis of size-selected, surface-passivated InP nanocrystals". In: *Journal of Physical Chemistry* 100.17 (1996), pp. 7212–7219. ISSN: 0022-3654.

[23] L. Dworak, V. V. Matylitsky, V. V. Breus, M. Braun, T. Basche, and J. Wachtveitl. "Ultrafast Charge Separation at the CdSe/CdS Core/Shell Quantum Dot/Methylviologen

Interface: Implications for Nanocrystal Solar Cells". In: *Journal of Physical Chemistry C* 115.10 (2011), pp. 3949–3955. ISSN: 1932-7447.

[24] K. F. Wu, N. H. Song, Z. Liu, H. M. Zhu, W. Rodriguez-Cordoba, and T. Q. Lian. "Interfacial Charge Separation and Recombination in InP and Quasi-Type II InP/CdS Core/Shell Quantum Dot-Molecular Acceptor Complexes". In: *Journal of Physical Chemistry A* 117.32 (2013), pp. 7561–7570. ISSN: 1089-5639.

[25] S. Adam, D. V. Talapin, H. Borchert, A. Lobo, C. McGinley, A. R. B. de Castro, M. Haase, H. Weller, and T. Moller. "The effect of nanocrystal surface structure on the luminescence properties: Photoemission study of HF-etched InP nanocrystals". In: *Journal of Chemical Physics* 123.8 (2005). ISSN: 0021-9606.

[26] O. I. Micic, A. J. Nozik, E. Lifshitz, T. Rajh, O. G. Poluektov, and M. C. Thurnauer. "Electron and hole adducts formed in illuminated InP colloidal quantum dots studied by electron paramagnetic resonance". In: *Journal of Physical Chemistry B* 106.17 (2002), pp. 4390–4395. ISSN: 1520-6106.

[27] L. Langof, E. Ehrenfreund, E. Lifshitz, O. I. Micic, and A. J. Nozik. "Continuous-wave and time-resolved optically detected magnetic resonance studies of nonetched/etched InP nanocrystals". In: *Journal of Physical Chemistry B* 106.7 (2002), pp. 1606–1612. ISSN: 1520-6106.

[28] J. D. Hybl, A. A. Ferro, and D. M. Jonas. "Two-dimensional Fourier transform electronic spectroscopy". In: *Journal of Chemical Physics* 115.14 (2001), pp. 6606–6622. ISSN: 0021-9606.

[29] T. Brixner, T. Mancal, I. V. Stiopkin, and G. R. Fleming. "Phase-stabilized two-dimensional electronic spectroscopy". In: *Journal of Chemical Physics* 121.9 (2004), pp. 4221–4236. ISSN: 0021-9606.

[30] Y. C. Cheng and G. R. Fleming. "Dynamics of Light Harvesting in Photosynthesis". In: *Annual Review of Physical Chemistry*. Vol. 60. Annual Review of Physical Chemistry. 2009, pp. 241–262. ISBN: 978-0-8243-1060-8.

[31] G. D. Scholes, G. R. Fleming, A. Olaya-Castro, and R. van Grondelle. "Lessons from nature about solar light harvesting". In: *Nature Chemistry* 3.10 (2011), pp. 763–774. ISSN: 1755-4330.

[32] J. R. Caram, H. B. Zheng, P. D. Dahlberg, B. S. Rolczynski, G. B. Griffin, D. S. Dolzhnikov, D. V. Talapin, and G. S. Engel. "Exploring size and state dynamics in CdSe quantum dots using two-dimensional electronic spectroscopy". In: *Journal of Chemical Physics* 140.8 (2014). ISSN: 0021-9606.

[33] Y. C. Cheng and G. R. Fleming. "Coherence quantum beats in two-dimensional electronic spectroscopy". In: *Journal of Physical Chemistry A* 112.18 (2008), pp. 4254–4260. ISSN: 1089-5639.

[34] Y. C. Cheng, G. S. Engel, and G. R. Fleming. "Elucidation of population and coherence dynamics using cross-peaks in two-dimensional electronic spectroscopy". In: *Chemical Physics* 341.1-3 (2007), pp. 285–295. ISSN: 0301-0104.

[35] T. R. Calhoun, N. S. Ginsberg, G. S. Schlau-Cohen, Y. C. Cheng, M. Ballottari, R. Bassi, and G. R. Fleming. "Quantum Coherence Enabled Determination of the Energy Landscape in Light-Harvesting Complex II". In: *Journal of Physical Chemistry B* 113.51 (2009), pp. 16291–16295. ISSN: 1520-6106.

[36] D. B. Turner, R. Dinshaw, K. K. Lee, M. S. Belsley, K. E. Wilk, P. M. G. Curmi, and G. D. Scholes. "Quantitative investigations of quantum coherence for a light-harvesting protein at conditions simulating photosynthesis". In: *Physical Chemistry Chemical Physics* 14.14 (2012), pp. 4857–4874. ISSN: 1463-9076.

[37] J. R. Caram, H. Zheng, P. D. Dahlberg, B. S. Rolczynski, G. B. Griffin, A. F. Fidler, D. S. Dolzhnikov, D. V. Talapin, and G. S. Engel. "Persistent Interexcitonic Quantum

Coherence in CdSe Quantum Dots". In: *Journal of Physical Chemistry Letters* 5.1 (2014), pp. 196–204. ISSN: 1948-7185.

[38] H. B. Zheng, J. R. Caram, P. D. Dahlberg, B. S. Rolczynski, S. Viswanathan, D. S. Dolzhnikov, A. Khadivi, D. V. Talapin, and G. S. Engel. "Dispersion-free continuum two-dimensional electronic spectrometer". In: *Applied Optics* 53.9 (2014), pp. 1909–1917. ISSN: 1559-128X.

[39] L. Biadala, B. Siebers, Y. Beyazit, M. D. Tessier, D. Dupont, Z. Hens, D. R. Yakovlev, and M. Bayer. "Band-Edge Exciton Fine Structure and Recombination Dynamics in InP/ZnS Colloidal Nanocrystals". In: *Acs Nano* 10.3 (2016), pp. 3356–3364. ISSN: 1936-0851.

[40] E. Kadantsev and P. Hawrylak. "Theory of exciton fine structure in semiconductor quantum dots: Quantum dot anisotropy and lateral electric field". In: *Physical Review B* 81.4 (2010). ISSN: 1098-0121.

[41] A. M. Kelley. "Electron-Phonon Coupling in CdSe Nanocrystals from an Atomistic Phonon Model". In: *Acs Nano* 5.6 (2011), pp. 5254–5262. ISSN: 1936-0851.

[42] G. A. Nelson and X. Y. Zhu. "Reversible Surface Electronic Traps in PbS Quantum Dot Solids Induced by an Order-Disorder Phase Transition in Capping Molecules". In: *Journal of the American Chemical Society* 134.18 (2012), pp. 7592–7595. ISSN: 0002-7863.

[43] D. Bozyigit, N. Yazdani, M. Yarema, O. Yarema, W. M. M. Lin, S. Volk, K. Vuttivorakulchai, M. Luisier, F. Juranyi, and V. Wood. "Soft surfaces of nanomaterials enable strong phonon interactions". In: *Nature* 531.7596 (2016), pp. 618–622. ISSN: 0028-0836.

[44] J. Fritsch, P. Pavone, and U. Schroder. "Ab-Initio Calculation of the Phonon-Dispersion in Bulk InP and in the InP(110) Surface". In: *Physical Review B* 52.15 (1995), pp. 11326–11334. ISSN: 2469-9950.

[45] C. S. R. Rao, S. Sundaram, R. L. Schmidt, and J. Comas. "Study of Ion-Implantation Damage in GaAs-Be and InP-Be Using Raman-Scattering". In: *Journal of Applied Physics* 54.4 (1983), pp. 1808–1815. ISSN: 0021-8979.

[46] E. Bedel, G. Landa, R. Carles, J. P. Redoules, and J. B. Renucci. "Raman Investigation of the InP Lattice-Dynamics". In: *Journal of Physics C-Solid State Physics* 19.10 (1986), pp. 1471–1479. ISSN: 0022-3719.

[47] E. Bedel, G. Landa, R. Carles, J. B. Renucci, J. M. Roquais, and P. N. Favennec. "Characterization of Implantation and Annealing of the Zn-Implanted InP by Raman-Spectrometry". In: *Journal of Applied Physics* 60.6 (1986), pp. 1980–1984. ISSN: 0021-8979.

[48] P. S. Peercy. "Raman Scattering of Ion-Implanted GaAs". In: *Applied Physics Letters* 18.12 (1971), pp. 574–&. ISSN: 0003-6951.

[49] D. Gallet and G. Hollinger. "Chemical, Structural, and Electronic-Properties of Sulfur-Passivated InP(001) (2x1) Surfaces Treated with (NH4)2SX". In: *Applied Physics Letters* 62.9 (1993), pp. 982–984. ISSN: 0003-6951.

[50] R. W. M. Kwok, G. Jin, B. K. L. So, K. C. Hui, L. Huang, W. M. Lau, C. C. Hsu, and D. Landheer. "Sulfide-Assisted Reordering at the InP Surface and SInX/InP Interface". In: *Journal of Vacuum Science & Technology a-Vacuum Surfaces and Films* 13.3 (1995), pp. 652–657. ISSN: 0734-2101.

[51] R. Iyer, R. R. Chang, A. Dubey, and D. L. Lile. "The Efect of Phosphorus and Sulfur Treatment on the Surface-Properties of InP". In: *Journal of Vacuum Science & Technology B* 6.4 (1988), pp. 1174–1179. ISSN: 1071-1023.

[52] W. M. Lau, S. Jin, X. W. Wu, and S. Ingrey. "Studies on Type-Inversion of Sulfide-Treated p-InP". In: *Journal of Vacuum Science & Technology a-Vacuum Surfaces and Films* 9.3 (1991), pp. 994–997. ISSN: 0734-2101.

[53] F. Wang, H. Yu, J. Li, Q. Hang, D. Zemlyanov, P. C. Gibbons, L. W. Wang, D. B. Janes, and W. E. Buhro. "Spectroscopic properties of colloidal indium phosphide quantum wires". In: *Journal of the American Chemical Society* 129.46 (2007), pp. 14327–14335. ISSN: 0002-7863.

[54] M. Sluydts, K. De Nolf, V. Van Speybroeck, S. Cottenier, and Z. Hens. "Ligand Addition Energies and the Stoichiometry of Colloidal Nanocrystals". In: *Acs Nano* 10.1 (2016), pp. 1462–1474. ISSN: 1936-0851.

[55] F. D. Fuller, J. Pan, A. Gelzinis, V. Butkus, S. S. Senlik, D. E. Wilcox, C. F. Yocum, L. Valkunas, D. Abramavicius, and J. P. Ogilvie. "Vibronic coherence in oxygenic photosynthesis". In: *Nature Chemistry* 6.8 (2014), pp. 706–711. ISSN: 1755-4330.

[56] M. L. Flanagan, P. D. Long, P. D. Dahlberg, B. S. Rolczynski, S. C. Massey, and G. S. Engel. "Mutations to R. sphaeroides Reaction Center Perturb Energy Levels and Vibronic Coupling but Not Observed Energy Transfer Rates". In: *Journal of Physical Chemistry A* 120.9 (2016), pp. 1479–1487. ISSN: 1089-5639.

[57] L. L. Wang, G. B. Griffin, A. Zhang, F. Zhai, N. E. Williams, R. F. Jordan, and G. S. Engel. "Controlling quantum-beating signals in 2D electronic spectra by packing synthetic heterodimers on single-walled carbon nanotubes". In: *Nature Chemistry* 9.3 (2017), pp. 219–225. ISSN: 1755-4330.

[58] M. R. Salvador, M. W. Graham, and G. D. Scholes. "Exciton-phonon coupling and disorder in the excited states of CdSe colloidal quantum dots". In: *Journal of Chemical Physics* 125.18 (2006). ISSN: 0021-9606.

CHAPTER 4

SCALABLE LIGAND-MEDIATED TRANSPORT SYNTHESIS OF ORGANIC-INORGANIC HYBRID PEROVSKITE NANOCRYSTALS WITH RESOLVED ELECTRONIC STRUCTURE AND ULTRAFAST DYNAMICS

4.1 Abstract

Colloidal perovskite nanocrystals support bright, narrow PL tunable over the visible spectrum. However, bandgap tuning of these materials remains limited to laboratory-scale syntheses. In this work, we present a polar-solvent-free ligand-mediated transport synthesis of high-quality organic-inorganic perovskite nanocrystals under ambient conditions with photoluminescence quantum yields up to 97%. Our synthesis employs a ligand-mediated transport mechanism that circumvents the need for exquisite external control (e.g., temperature control, inert-gas protection, dropwise addition of reagents) required by other methods due to extremely fast reaction kinetics. In the ligand-mediated transport mechanism, multiple equilibria cooperatively dictate reaction rates and enable precise control over NC size. These small nanocrystals exhibit high photoluminescence quantum yields due to quantum confinement. Nanosecond transient absorption spectroscopy experiments reveal a fluence-independent PL decay originating from exciton recombination. Two-dimensional electronic spectroscopy resolves multiple spectral features reflecting the electronic structure of the

nanocrystals. The resolved features exhibit size-dependent spectral positions, further indicating the synthesized nanocrystals are quantum-confined.

4.2 Introduction

Organic-inorganic lead-halide hybrid perovskite materials have recently attracted extensive research attention due to their extraordinary photophysical properties and performance in optoelectronic applications. Previous studies have demonstrated that perovskite microcrystals and bulk single crystals exhibit characteristics including large absorption coefficients,[1] small exciton binding energies,[2] efficient photogeneration of free carriers,[3, 4] high charge carrier mobility,[5, 6] and bimolecular charge recombination dynamics.[7, 8] Solar cells using organolead halide perovskite thin films as their active layer have achieved certified power conversion efficiencies up to 23%.[9–13] Perovskites have also shown promise for applications in low-threshold optically pumped lasers[14–16] and light-emitting diodes (LEDs).[17] In perovskite microcrystals and bulk single crystals, excitons spontaneously dissociate into free carriers due to the weak binding energy, which is ideal for solar cell devices. However, nonradiative recombination of the carriers limits the light-emitting performance of perovskites.[18] Increasing the exciton binding energy through quantum confinement has recently been explored to overcome the relatively weak photoluminescence (PL) of perovskite microcrystals and bulk single crystals by fabricating nanostructured materials.[19–23] Perovskite nanocrystals (NCs), both organic-inorganic (typically incorporating methylammonium, MA+) and purely inorganic (typically incorporating cesium ions), demonstrate high defect tolerance, low density of detrimental midgap trap states, and high photoluminescence quantum yield (PLQY) at room temperature without additional surface passivation.[19, 21, 24–26] The narrow PL of these perovskite NCs is tunable over the entire visible range (from 410 to 700 nm) by adjusting the size and halide composition,[20, 22, 27, 28] making these materials applicable to lasers,[19, 28] optical sensing,[29] and color-tuning displays.[21] Although perovskite NCs exhibit remarkable properties, bandgap tuning of these NCs is usually realized

via composition tuning subsequent to synthesis of pure perovskite NCs by hot injection[19, 30] or ligand-assisted reprecipitation (LARP)[18, 21, 24, 25, 31] methods. These methods are not readily adaptable to industrial scale preparations. These syntheses demand delicate external control over reaction conditions due to the extremely fast kinetics of NC formation and require the use of polar solvents (e.g., DMF), which are detrimental to the long-term colloidal stability and structural integrity of the NCs.[26, 27, 32] Moreover, mixed-halide or iodide-based perovskite NCs are synthesized either under inert atmosphere[21, 26] or via indirect postsynthetic anion exchange.[20, 22] The postsynthetic anion exchange introduces an extra synthetic step and requires pure NCs[20, 22] (usually bromide based) as a starting material. Here, we present an atmospheric, room-temperature, ligand-mediated transport method in nonpolar solvent to prepare perovskite NCs with bright and spectrally narrow emission. We focus on the synthesis of organic-inorganic perovskite NCs ($MAPbX_3$, X = Br, I, mixed halide). The ligand-mediated transport synthesis employs nonpolar solvents (hexane or toluene) containing a trace capping ligand (octylamine, protonated by oleic acid), which are added to the mixed solid precursors (PbX_3 and MAX, X = Br, I, or mixed halide). Then, through vigorous stirring, the colloidal NCs are formed as the ligands solvate the lead salt and carry it into the solution phase. This strategy allows the direct synthesis of mixed-halide and iodide-based perovskite NCs without inert atmosphere protection and yields colloidal NC solutions at high concentrations. The resultant NCs demonstrate good colloidal stability even at high sample concentration, enabling spectroscopic investigations of their ultrafast dynamics by techniques including two-dimensional electronic spectroscopy (2DES), which typically requires $10^2 - 10^3$ times more concentrated solutions (about 0.2 OD in a 200 μm path length) than fluorescence measurements. Our broadband femtosecond 2DES experiments on $MAPbI_3$ NCs resolve multiple spectral features that shift with NC sizes, reflecting the electronic structure of these NCs as well as ultrafast dynamics (including relaxation and quantum-beating signals) after the initial excitation. Nanosecond transient absorption (TA) spectroscopy experiments reveal a PL decay that is independent of radiation

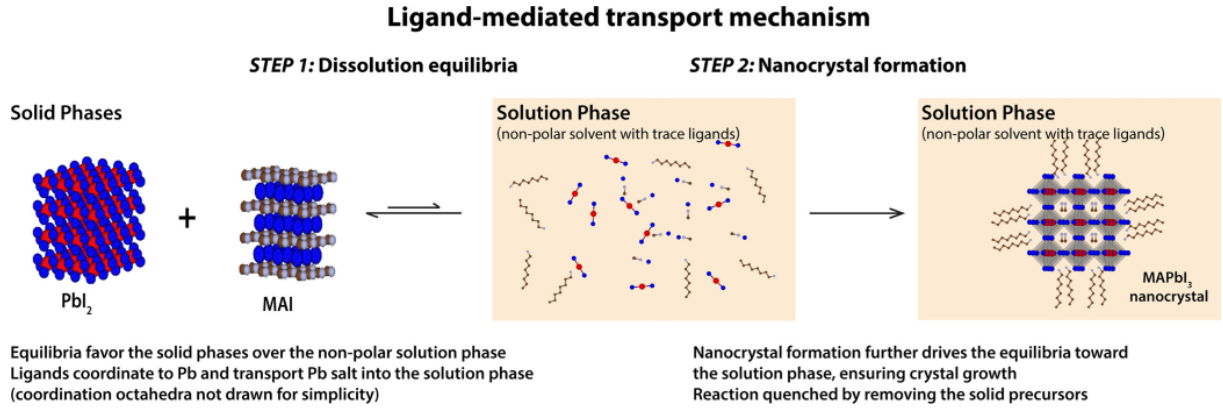

Figure 4.1: Illustrative reaction mechanism of the ligand-mediated transport strategy (using the synthesis of MAPbI3 NCs as an example). Red, blue, brown, and white spheres represent Pb, I, C, and N atoms, respectively. The first mechanistic step (Step 1) involves the dissolution equilibria of the two precursors (PbI_2 and MAI) between the solid and solution phases. The equilibria strongly favor the solid phases over the nonpolar solution phase. However, the trace ligands help dissolve the PbI_2 by coordinating to the Pb center and transport the Pb salt into solution phase to initiate the reaction. (Coordination octahedra are not drawn in the figure for simplicity.) Step 2 presents the NC formation from the dissolved precursors and ligands in the solution phase. The NC formation further drives the dissolution equilibria toward the solution phase, ensuring NC growth. The reactions can then be quenched by removal of the solid precursors via centrifugation or filtration.

fluence, indicating that the PL originates from exciton recombination.

4.3 Materials and Methods

4.3.1 Materials

40 wt % methylamine (CH_3NH_2) in methanol (TCI America), 48 wt % hydrobromic acid (HBr) in water (Sigma-Aldrich), 57 wt % hydriodic acid (HI) in water (Sigma-Aldrich), $PbBr_2$ (≥98%, Sigma-Aldrich), PbI_2 (99%, Sigma-Aldrich), octylamine (99%, SigmaAldrich), and oleic acid (technical grade, 90%, Sigma-Aldrich).

4.3.2 Preparation of CH_3NH_3Br

CH_3NH_3Br was synthesized by the reaction between 40 wt % CH_3NH_2 in methanol and 48 wt % HBr in water. An equimolar amount of HBr was added dropwise to the CH_3NH_2

solution under an ice bath and stirred for 2 h. The solvent was removed on a rotovap. The resulting solid was recrystallized in ethanol to yield snow-white CH_3NH_3Br crystals. CH_3NH_3Br crystals were dried under vacuum to remove residual ethanol.

4.3.3 Preparation of CH_3NH_3I

CH_3NH_3I was synthesized by the reaction between 40 wt % CH_3NH_2 in methanol and 57 wt % HI in water. An equimolar amount of HI was added dropwise to the CH_3NH_2 solution under ice bath and stirred for 2 h. The solvent was removed on a rotovap. The resulting solid was recrystallized in ethanol to yield snow-white CH_3NH_3I crystals. CH_3NH_3I crystals were dried under vacuum to remove residual ethanol.

4.3.4 Synthesis of $MAPbBr_3$ Nanocrystals

17.9 mg (0.16 mmol) CH_3NH_3Br and 73.4 mg (0.20 mmol) $PbBr_2$ were added into a 4 mL scintillation vial. One mL toluene, 20 μL octylamine, and 40 μL oleic acid were added to the solid precursors. The resulting mixture was stirred vigorously under ambient conditions for 1 h, followed by centrifugation for 5 min at 6000 rpm to remove the remaining solid precursors. A solution of $MAPbBr_3$ NCs with an average size of 3.0 nm (PLQY 92%) was obtained. Similarly, the same amount of solid precursors in 1 mL toluene with 5 μL octylamine and 10 μL oleic acid reacting for 3 h at ambient condition yielded $MAPbBr_3$ NCs with an average size of 5.0 nm (PLQY 70%). The as-synthesized NC solutions were stored at room temperature without further purification.

4.3.5 Synthesis of $MAPb(Br/I)_3$ Nanocrystals

17.9 mg (0.16 mmol) CH_3NH_3Br, 36.7 mg (0.10 mmol) $PbBr_2$, and 46.0 mg (0.10 mmol) PbI_2 were added into a 4 mL scintillation vial. One mL solvent (1:1 v/ v toluene/hexane), 20 μL octylamine, and 40 μL oleic acid were added to the solid precursors. The resulting mixture

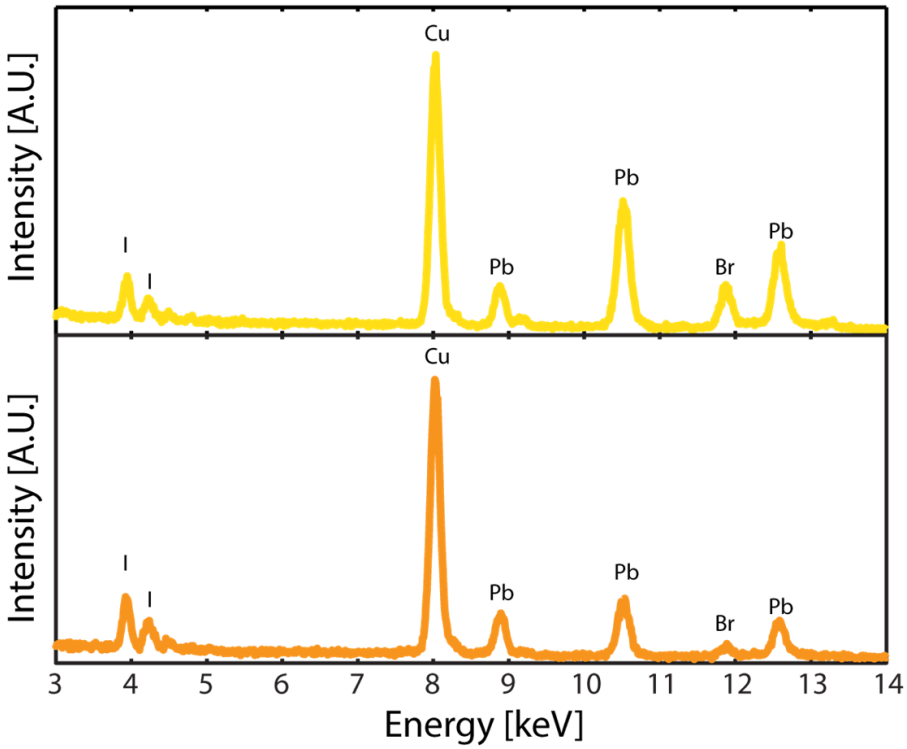

Figure 4.2: EDX spectra of $MAPb(Br/I)_3$ nanocrystals. Upper: Mixed-halide nanocrystals with PL centered at 550 nm. Lower: Mixed-halide nanocrystals with PL centered at 580 nm.

was stirred vigorously under ambient conditions for 45 min, followed by centrifugation for 5 min at 6000 rpm to remove the remaining solid precursors. A solution of $MAPb(Br/I)_3$ NCs with an average size of 3.6 nm (PL centered at 550 nm with fwhm of 29 nm) was obtained. Similarly, 17.9 mg (0.16 mmol) CH_3NH_3Br and 92.0 mg (0.20 mmol) PbI_2 in 1 mL solvent (1:1 v/v toluene/hexane), 20 μL octylamine, and 40 μL oleic acid reacting for 45 min at ambient condition yielded $MAPb(Br/I)_3$ with an average size of 2.6 nm (PL centered at 580 nm with fwhm of 28 nm). The as-synthesized NC solutions were stored at room temperature without further purification. The presence of both Br and I in the mixed-halide perovskite NCs has been confirmed by energy-dispersive X-ray spectroscopy (EDX) (Figure 4.2).

The NCs with PL centered at 580 nm contain significantly higher composition of I compared to the NCs with PL centered at 550 nm.

4.3.6 Synthesis of $MAPbI_3$ Nanocrystals

19.0 mg (0.12 mmol) CH_3NH_3I and 69.0 mg (0.15 mmol) PbI_2 were added into a 4 mL scintillation vial. One mL hexane, 20 μL octylamine, and 40 μL oleic acid were added to the solid precursors. The resulting mixture was stirred vigorously under ambient conditions for 1 h, followed by centrifugation for 5 min at 6000 rpm to remove the remaining solid precursors. A solution of $MAPbI_3$ NCs with an average size of 2.6 nm (PLQY 97%) was obtained. Similarly, 25.4 mg (0.16 mmol) CH_3NH_3I and 92.0 mg (0.20 mmol) PbI_2 in 1 mL hexane, 20 μL octylamine, and 40 μL oleic acid reacting for 3 h at ambient condition yielded $MAPbI_3$ with an average size of 5.0 nm (PLQY 52%). The assynthesized NC solutions were stored at room temperature without further purification.

4.3.7 Powder X-ray Diffraction

PXRD data were measured at 293 K on a Bruker D8 Discover GADDS using a Cu-α source (40 kV, 40 mA) with a Vantec-2000 2D detector. The as-synthesized perovskite NCs (with no postsynthetic purification) were

4.3.8 Photoluminescence Measurements

The steady-state PL spectra of the perovskite NCs were measured by a Horiba Fluorolog-3 spectrofluorometer. The PLQYs were measured by the same spectro-fluorometer with a calibrated integrating sphere (Quanta-phi, Horiba). The PL lifetimes were measured by a TCSPC fluorescence lifetime spectrometer (ISS chronosBH).

4.3.9 Transmission Electron Microscopy

TEM images were obtained by a FEI Tecnai F30 transmission electron microscope operating at 300 kV. The as-synthesized NCs were further diluted in hexane. A few drops of the resulting solution were drop-casted onto a Formvarcoated lacy carbon grid and further dried

in air for the measurements

4.3.10 Transient Absorption Spectroscopy

Transient absorption spectroscopy was performed on a home-built apparatus with a narrowband pump (Ekspla Pl2210 Nd:YAG and OPO with a pulse duration of 50 ps, centered at 600 nm) and a broadband super continuum fiber laser probe (Leukos STM with a pulse duration of 700 ps, 500-700 nm). Time delays were achieved using a delay generator (SRS DG535) externally synchronized to a 1 kHz master clock from the pump laser. The signal was spectrally resolved via a spectrometer (Acton Research Corporation Spectra Pro 2150i) and recorded with a line scan camera (Teledyne Dalsa Spyder3 1k) at 1 kHz.

4.3.11 Two-Dimensional Electronic Spectroscopy

2D electronic spectra were measured with a home-built passively phase-stabilized four-wave mixing apparatus. A Ti:sapphire regenerative amplifier (Legend Elite, Coherent) was seeded with the output of a Ti:sapphire oscillator (Micra, Coherent) to give 35 fs pulses at a repetition rate of 5 kHz and energy of 540 μJ/pulse. The output from the regenerative amplifier was then focused into a tube filled with argon gas (length: 2 m, pressure: 15 psi) to generate broadband white light. A cold mirror was used to filter the white light, yielding a spectrum with fwhm from 550 to 680 nm. Multiphoton intrapulse interference phase scan method (MIIPS) and a spatial light modulator (Biophotonic Solutions) were used to correct for dispersion and further compress the pulses to 12 fs at the sample position.[33] Three ultrashort laser pulses (incident power of 10 nJ/pulse onto a 100 μm diameter spot) interacted with the sample and generated a third-order signal in the phase-matched direction. The signal was heterodyne detected with a local oscillator pulse and recorded on a CCD (Andor Newton) thermoelectrically cooled to -50 C. The time delay between the first two pulses is coherence time (τ). The time delay between pulse 2 and pulse 3 is referred as waiting time (T), similar to the time delay in a typical TA measurement. The time delay between pulse 3 and the

third-order signal is rephasing time (t). Fourier transforms over both coherence time (τ) and rephasing time (t) domains yield 2D electronic spectra in the frequency-frequency domain. In the 2DES measurements on MAPbI3 NCs, the coherence time was scanned from -90 to 90 fs with a step size of 1.5 fs. Two sets of waiting time were scanned to capture the ultrafast dynamics: one from -20 to 1000 fs with a step size of 10 fs and the other from -20 to 200 fs with a step size of 2 fs. All 2DES measurements were conducted at room temperature. The perovskite NCs are measured with a concentration about 0.2 OD in 200 μm path length (Starna Cell, fused quartz) and are stable for at least 2 weeks experimental time under illumination.

4.4 Results and Discussion

Besides the practical advantages of performing NC synthesis at room temperature and under ambient conditions, our ligandmediated transport strategy offers improved NC size control compared to the hot-injection and LARP methods, due to slower nucleation and crystal growth. In our synthesis, multiple equilibria cooperatively control NC nucleation kinetics and growth rates, circumventing the high-temperature kinetics of hot injection and the prompt solubility changes in LARP that result in rapid product formation.[24, 25] The reaction mechanism of ligand-mediated transport is illustrated in Figure 4.1 (with comparison to hot injection and LARP shown in Figure 4.3).

In our synthesis, the mechanism first involves the dissolution equilibria of the two precursors. Because nonpolar solvents are used, these equilibria strongly favor the solid phases. Trace ligands in the nonpolar solvents transport Pb into the solution phase (Step 1) through coordination, initiating nucleation and subsequent NC growth (Step 2). The formation of these NCs in return drives the dissolution equilibria to the solution phase, ensuring further NC growth. Because the same ligands cap the NCs as aid dissolution of the lead, the kinetics become, to some degree, self-limiting. Thus, the crystal growth can be finely controlled by reaction time and quenched by removing the solid precursors. These equilibria

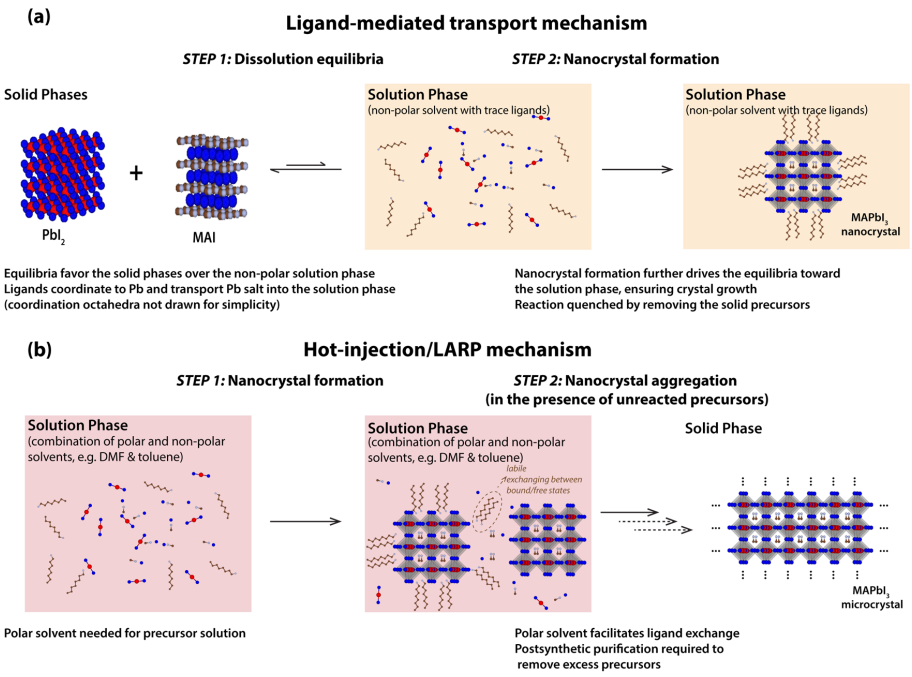

Figure 4.3: Comparison between reaction mechanisms of the solid-extraction strategy versus other strategies (using the synthesis of $MAPbI_3$ nanocrystals as an example). (a) Illustrative reaction mechanism of the solid-extraction strategy (same as shown in Fig. 1). Red, blue, brown, and white spheres represent Pb, I, C, and N atoms, respectively. The first mechanistic step (Step 1) involves the dissolution equilibria of the two precursors (PbI_2 and MAI) between the solid and solution phases. The equilibria strongly favor the solid phases over the non-polar solution phase. However, the trace ligands help dissolve the PbI_2 by coordinating to the Pb center and transport the Pb salt into the solution phase to initiate the reaction. (Coordination octahedra are not drawn in the figure for simplicity.) Step 2 presents the nanocrystal formation from the dissolved precursors and ligands in the solution phase. The NC formation further drives the dissolution equilibria toward the solution phase, ensuring NC growth. The reactions can then be quenched by removal of the solid precursors via centrifugation or filtration. (b) Illustrative reaction mechanism of the other strategies (hot-injection and LARP). Step 1: In hot-injection or LARP method, precursors are usually prepared in polar solvents (such as DMF) and the reaction starts in the solution phase (combination of both polar and non-polar solvents). Size control is more difficult in these methods due to the extremely fast reaction dynamics; in LARP, crystal growth is driven by the prompt solubility change induced by solvent mixing, while in hot injection, the formation rate is determined by the underlying ionic metathesis reaction at high temperature. Step 2: In the presence of unreacted precursors in the solution, the nanocrystals will slowly aggregate to form microcrystals and eventually precipitate from the solution phase. For colloidal perovskite nanocrystals, the capping ligands exchange between bound and free states on the nanocrystal surfaces, dynamically stabilizing the nanocrystals. The remaining MA+, if any, will replace the capping ligand and cause nanocrystal aggregation. Polar solvents will quickly desorb the capping ligands and further facilitate the exchange reaction. Hence, postsynthetic purification removing excess precursors is required to improve colloidal stability.

cooperatively dictate reaction rates and enable precise control over NC size, making the size distribution highly reproducible. In addition to the benefits mentioned above, the ligandmediated transport method improves colloidal stability by allowing unreacted solid precursors to be easily removed via filtration or centrifugation. Recent 2D-NMR studies have suggested that capping ligands dynamically stabilize perovskite NCs synthesized via hot injection or LARP, exhibiting fast exchange between bound and free states.[34] Thus, any unreacted MA+ would replace the capping ligands, causing further, undesirable aggregation. In our ligand-mediated transport synthesis, removal of solid precursors and exclusive use of nonpolar solvents significantly suppress the presence of excess MA+ in solution. Without excess MA+ , the replacement of capping ligands with MA+ is suppressed, enhancing the colloidal stability of the resulting NCs. The linear absorption and PL spectra of ligand-mediated transport synthesized NCs are shown in Figure 4.4a, with detailed synthetic protocols provided in the Materials and Methods section. These NCs exhibit spectrally narrow (fwhm of 12-50 nm) and remarkably bright (QY up to 97% measured with an integrating sphere) PL that is tunable across the visible spectrum.

We attribute the bright PL to increased exciton binding resulting from quantum confinement. Powder X-ray diffraction (PXRD) patterns demonstrate the crystallinity and phase purity of these NCs (Figure 4.4b). The PXRD pattern of the $MAPbBr_3$ NCs matches their reference pattern (top panel in Figure 4.4b), which is simulated from the bulk, cubic single-crystal structure at room temperature (a = 5.9334(5) $\AA$, space group Pm-3m). The PXRD pattern of $MAPbI_3$ matches their simulated spectra (bottom panel in Figure 2b) as well, but the simulated pattern is obtained from the bulk, pseudocubic single-crystal structure at high temperature (400 K, a = 6.3115(2) $\AA$, c = 6.3161(2) $\AA$, space group P4mm), as opposed to the room-temperature tetragonal phase (a = 8.8922(1) $\AA$, c = 12.635(3) $\AA$, space group I4/m). As shown in Figure 4.4, the PXRD pattern shifts continuously and deviates incrementally from the cubic phase toward the pseudocubic phase with the composition change from Br- to I -, due to the larger radius of I- versus Br-. The size distributions of these NCs

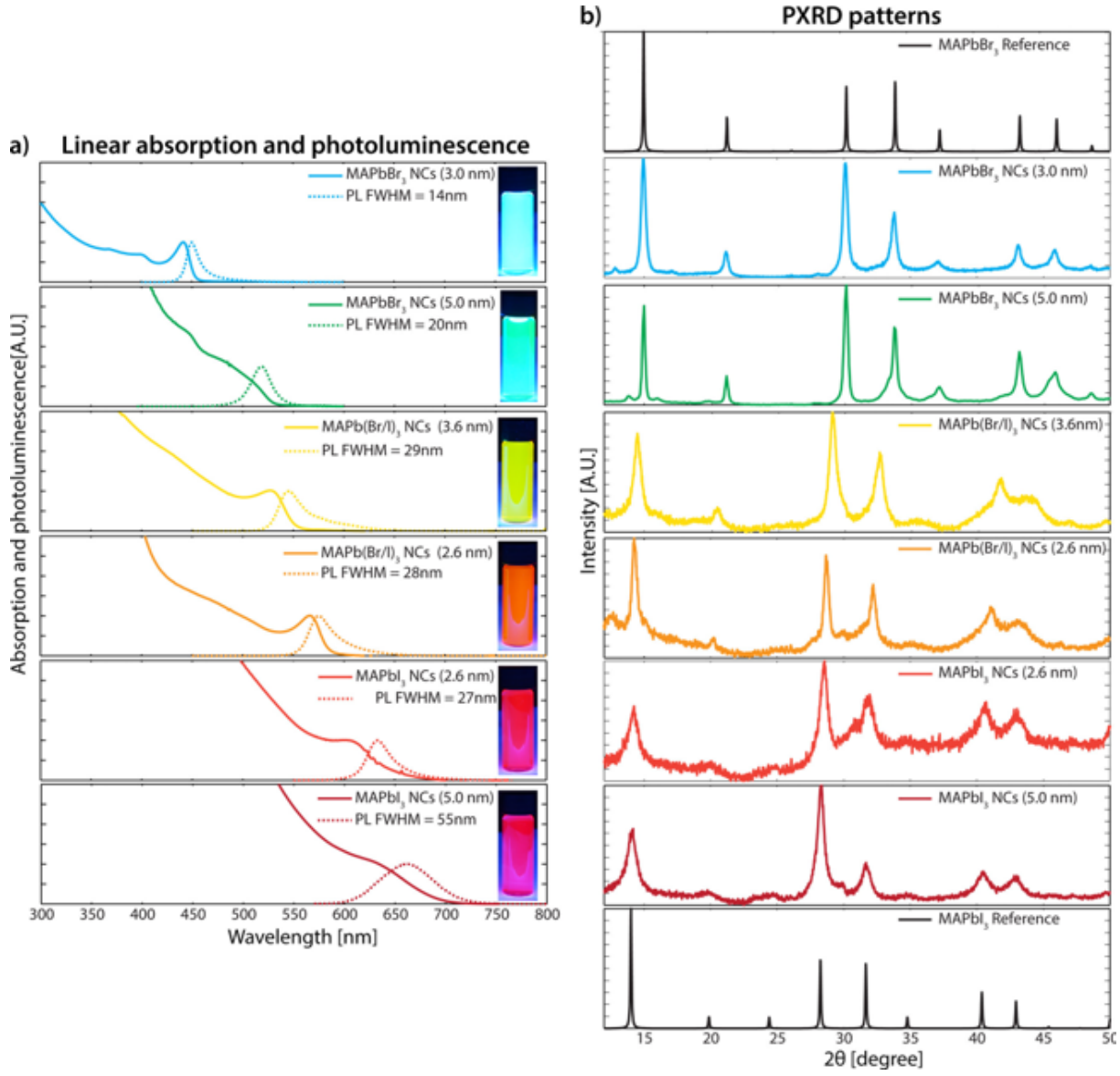

Figure 4.4: Characterization of the as-synthesized organic-inorganic perovskite NCs. (a) Linear absorption and PL spectra. (b) PXRD patterns. The top and bottom panels are reference patterns simulated from the single-crystal structures of $MAPbBr_3$ and $MAPbI_3$, respectively.

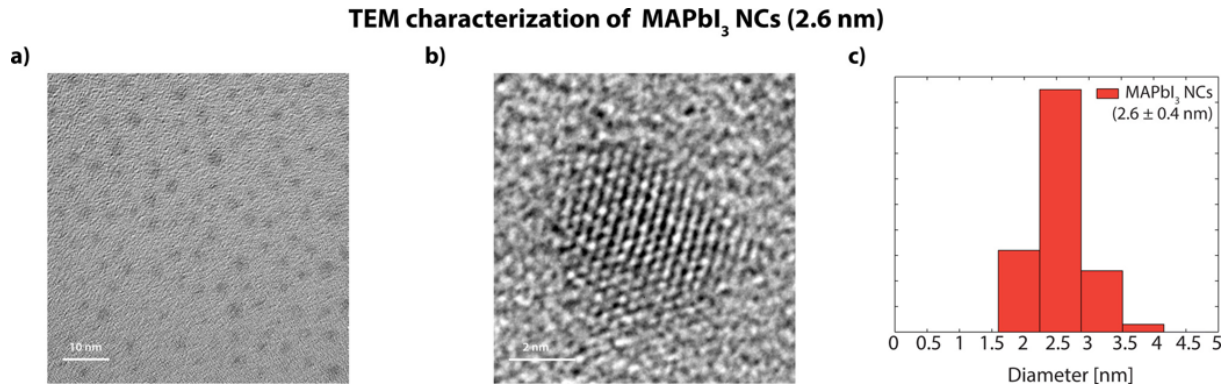

Figure 4.5: TEM characterization on $MAPbI_3$ NCs (average size 2.6 nm). (a) TEM image of the $MAPbI_3$ NCs. (b) Magnified TEM image confirms crystallinity of these NCs. (c) Size distribution of the $MAPbI_3$ NCs shows an average size of 2.6 nm

were characterized by high-resolution TEM.

Figure 4.5 shows the TEM images of $MAPbI_3$ NCs with PL centered around 635 nm and an average size of 2.6 ± 0.4 nm. The magnified TEM image demonstrates well-defined lattice patterns and further confirms the crystallinity of these samples. We investigated the photophysical dynamics of our perovskite NCs using nanosecond TA and broadband femtosecond 2DES. Results from nanosecond TA spectroscopy on $MAPbI_3$ NCs (2.6 nm) are shown in Figure 4.6. Two features are observed in the TA spectrum (Figure 4.6a, plotted in transmitted light ΔT): a negative feature due to excited-state absorption and a positive feature corresponding to stimulated emission from the PL state. The time traces of these features (extracted at 570 and 635 nm, respectively) exhibit the same decay dynamics (Figure 4.6b), suggesting that both features arise from the same PL state. Single exponential fitting of the decay shows a lifetime of 12.6 ± 0.6 ns, consistent with the PL lifetime obtained from time-correlated single photon counting (TCSPC) measurement (Figure 4.7).

The decay of the PL state exhibits no radiation fluence dependence (Figure 4.6c), indicating that the PL is due to the radiative recombination of excitons. In contrast, the dim PL of bulk perovskites is power-dependent and caused by charge-carrier recombination.[8] The calculated Bohr radius for an exciton in $MAPbI_3$ is 2.8 nm (5.6 nm in diameter),[35] larger than the size of measured $MAPbI_3$ NCs. Therefore, the observed radiation fluence-

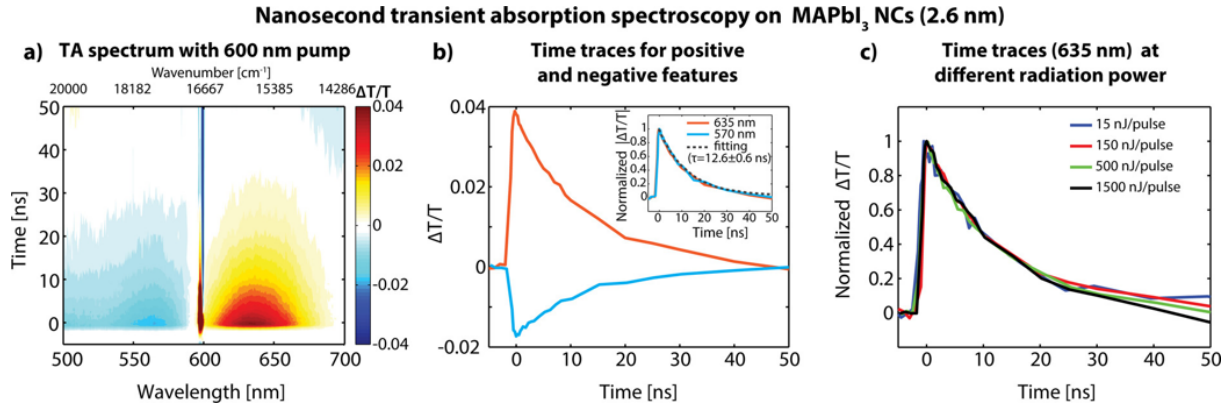

Figure 4.6: Nanosecond TA spectroscopy on MAPbI3 NCs (average size 2.6 nm). (a) TA spectrum of MAPbI3 (2.6 nm). (b) Time traces extracted from the negative feature (570 nm) and the positive feature (635 nm). Absolute-valued normalized traces are shown in the inset and demonstrate the same decay dynamics for both features. (c) Normalized time traces of the positive feature under varied radiation fluences reveal power-independent decay dynamics.

independent PL (excitonic in nature) is most likely due to the increased binding energy generated by quantum confinement of the exciton within the NC.

The nanosecond TA measurements can only capture the dynamics of the PL state. Better temporal resolution is required to investigate other phenomena after initial photoexcitation. We therefore performed femtosecond 2DES measurements on these NCs. 2DES can be viewed as simultaneously performing multiple spectrally resolved TA measurements with different excitation wavelengths in a single experiment. Displaying signals as 2D frequency-frequency correlation maps as a function of time delay (T), 2DES can reveal couplings between different electronic states, ultrafast coherent dynamics, and detailed energy transfer pathways. In a 2D spectrum, the horizontal axis (excitation frequency) indicates the energy absorbed by the sample, while the vertical axis (detection frequency) indicates the energy emitted (or absorbed) by the sample after a certain waiting time (T). The 2D representation permits improved resolution of the underlying electronic structure. For example, ground-state bleach signals will usually stay stationary, while the stimulatedemission features will shift downward and appear as lowerdiagonal crosspeaks as energy transfer occurs. This separation resolves different features that would otherwise overlap spectrally in TA measurements. The 2D

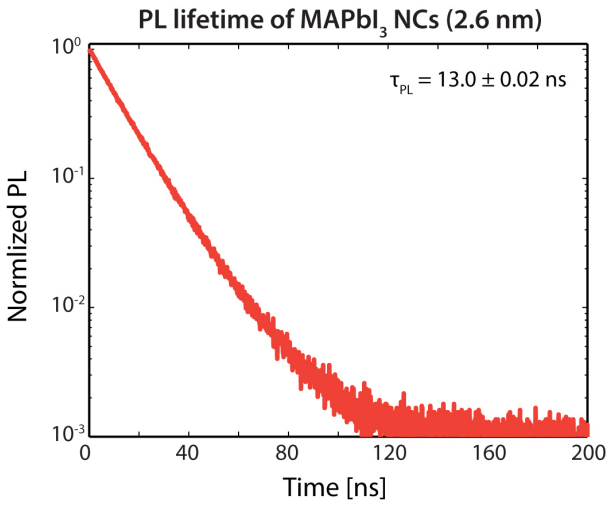

Figure 4.7: TCSPC measurement of MAPbI3 nanocrystals (2.6 nm) yielding a PL lifetime of 13 ns.

spectra at T = 1000 fs of MAPbI3 NCs with average sizes of 2.6 and 5.0 nm are shown, respectively, in Figure 4.8. Three resolved spectral features are observed in the 2D spectra of $MAPbI_3$ NCs with both sizes. The spectral position of the lowest energy feature within each spectrum is consistent with the corresponding PL state. Horizontal slices from each 2D spectrum are shown in Figure 4.8b. The excitation energies of these spectral features shift with NC size, indicating that the probed NCs are quantum-confined, and these three spectral features reflect the inherent electronic structures of the NCs instead of vibronic progressions.[36]

Figure 4.9 shows a series of 2D spectra of $MAPbI_3$ NCs (2.6 nm) at different waiting times (10, 30, 50, 100, 500, and 1000 fs, respectively), the time traces extracted from three lower diagonal crosspeaks exhibiting sub-50 fs relaxation dynamics and quantum-beating signals observed from the upper diagonal excited state absorption features. At T = 10 fs, the elongated lineshapes of the main diagonal features show that the system maintains memory of its initial excitation frequency on the timescale of the pulse duration (12 fs). Such elongated lineshapes at early waiting times may arise from probing a system that has either a complex electronic structure or an inhomogeneous distribution. To differentiate and determine the origin of the features, we examine the longer waiting time spectra. As

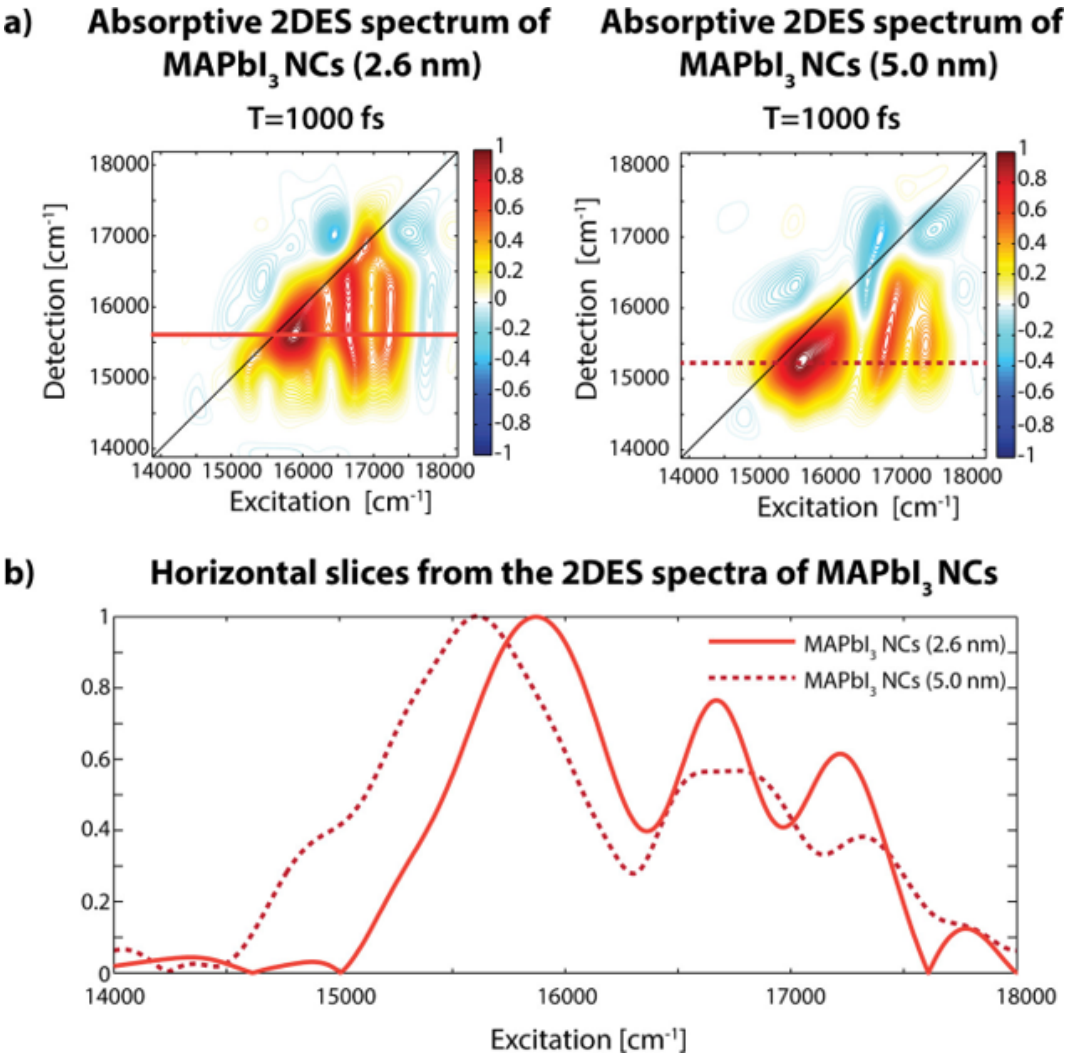

Figure 4.8: 2DES spectra of $MAPbI_3$ NCs with different sizes demonstrate the electronic nature of the probed states. (a) Left: Absorptive 2DES spectrum of $MAPbI_3$ NCs (2.6 nm) at T = 1000 fs. Right: Absorptive 2DES spectrum of $MAPbI_3$ NCs (5.0 nm) at T = 1000 fs. (b) Horizontal slices from the 2DES spectra of $MAPb_I3$ NCs shown in panel (a). Both slices show three spectral features. The spacing between these spectral features shifts with NC sizes, indicating that the probed NCs are quantum-confined, and the three spectral features reflect the electronic structure of the NCs.

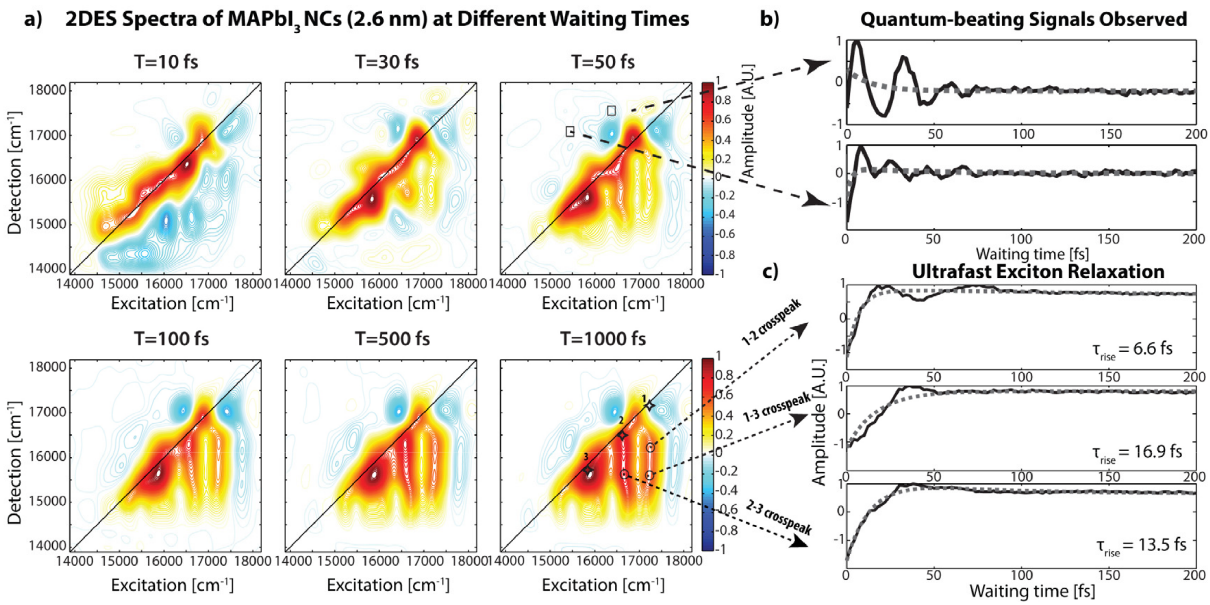

Figure 4.9: (a) 2D spectra of $MAPbI_3$ at different waiting times. (b) Upper diagonal crosspeaks show quantum-beating signals. (c) Lower diagonal crosspeaks reveal sub-50 fs relaxation.

the waiting time evolves, the elongated feature evolves into three features (marked as labels 1-3 in Figure 4.9). The spectral position of feature 3 is consistent with the PL state. The stimulated emission of features 1 and 2 clearly moves down as energy is transferred, resulting in three crosspeaks (1-2, 1-3, and 2-3) on the 2D spectra. After T = 100 fs, the 2D spectra remain almost unchanged. The growth of the lower diagonal crosspeaks indicates clearly that these features all exist on the same NC. Thus, this crosspeak pattern demonstrates that all the features shown on the main diagonal of the 2D spectrum at T = 10 fs are due to the electronic structure of the NCs rather than an inhomogeneous distribution.

The upper-diagonal cross peaks of the spectrum also feature interesting quantum beating signatures that increase in frequency the further away from the diagonal the spectrum is probed. This could be due to a number of different sources, but it seems likely to be due to coherence between excited states that decoheres on the order of 50 fs in these systems. However, this is not definitive as electron-phonon coupling could produce similar effects, but because of the very fast dephasing rate and the change in frequency with the gap between the probed excited states, it would be very interesting to study these materials at low

temperature to determine the origin of these oscillatory features.

4.5 Conclusions

We have developed a ligand-mediated transport synthesis of quantum-confined organic-inorganic perovskite ($MAPbX_3$) NCs that operates under ambient conditions. Due to its robust reaction conditions and convenient external controls, this ligand-mediated transport method moves this material closer to industrial realization. The dissolution equilibria involved in the reaction allow precise control of size and composition, yielding quantum-confined NCs with high PLQY. Nanosecond TA spectra reveal an excitonic PL decay that is independent of radiation fluence, indicating direct radiative excitonic recombination. Femtosecond 2DES spectra resolve spectral features that shift with NC size, reflecting the inherent electronic structure of the NCs. These observations confirm that our NCs are quantum-confined. Additionally, we observe sub-50 fs excitonic relaxation and quantum-beating signals that dephase with lifetimes of about 40 fs. Further investigation is required to assign these ultrafast dynamics and to understand the mechanisms of relaxation to the PL state. Of particular interest would be whether energy relaxes to the PL state through a coherent or incoherent mechanism.

4.6 Acknowledgements

The authors gratefully thank Justin Jureller for suggestions regarding PL measurements; Igor Fedin for suggestions regarding PXRD measurements; and Feng Zhai and Dmitri Talapin for useful discussions. D.H. is supported by the Joseph J. Katz Postdoctoral Fellowship at Argonne National Laboratory. We thank DTRA (grant no. HDTRA1-10-0091), AFOSR (grant no. FA9550-14-1-0367), NSF MRSEC Program (grant no. DMR 14-20709), the DoD NSSEFF program (grant no. N00014-16-1-2513), the Alfred P. Sloan Foundation, and the Camille and Henry Dreyfus Foundation for support. Funding for this research was provided

in part by Qatar National Research Foundation (QNRF), NPRP X-107-010027. N.E.W. acknowledges support from the NSF GRFP program, and R.E.W. acknowledges support from the DoD NDSEG fellowship program.

REFERENCES

[1] M. A. Green, A. Ho-Baillie, and H. J. Snaith. "The emergence of perovskite solar cells". In: *Nature Photonics* 8.7 (2014), pp. 506–514. ISSN: 1749-4885.

[2] V. D'Innocenzo, G. Grancini, M. J. P. Alcocer, A. R. S. Kandada, S. D. Stranks, M. M. Lee, G. Lanzani, H. J. Snaith, and A. Petrozza. "Excitons versus free charges in organo-lead tri-halide perovskites". In: *Nature Communications* 5 (2014). ISSN: 2041-1723.

[3] A. Marchioro, J. Teuscher, D. Friedrich, M. Kunst, R. van de Krol, T. Moehl, M. Gratzel, and J. E. Moser. "Unravelling the mechanism of photoinduced charge transfer processes in lead iodide perovskite solar cells". In: *Nature Photonics* 8.3 (2014), pp. 250–255. ISSN: 1749-4885.

[4] C. S. Ponseca, T. J. Savenije, M. Abdellah, K. B. Zheng, A. Yartsev, T. Pascher, T. Harlang, P. Chabera, T. Pullerits, A. Stepanov, J. P. Wolf, and V. Sundstrom. "Organometal Halide Perovskite Solar Cell Materials Rationalized: Ultrafast Charge Generation, High and Microsecond-Long Balanced Mobilities, and Slow Recombination". In: *Journal of the American Chemical Society* 136.14 (2014), pp. 5189–5192. ISSN: 0002-7863.

[5] G. C. Xing, N. Mathews, S. Y. Sun, S. S. Lim, Y. M. Lam, M. Gratzel, S. Mhaisalkar, and T. C. Sum. "Long-Range Balanced Electron- and Hole-Transport Lengths in Organic-Inorganic $CH_3NH_3PbI_3$". In: *Science* 342.6156 (2013), pp. 344–347. ISSN: 0036-8075.

[6] S. D. Stranks, G. E. Eperon, G. Grancini, C. Menelaou, M. J. P. Alcocer, T. Leijtens, L. M. Herz, A. Petrozza, and H. J. Snaith. "Electron-Hole Diffusion Lengths Exceeding 1 Micrometer in an Organometal Trihalide Perovskite Absorber". In: *Science* 342.6156 (2013), pp. 341–344. ISSN: 0036-8075.

[7] F. Deschler, M. Price, S. Pathak, L. E. Klintberg, D. D. Jarausch, R. Higler, S. Huttner, T. Leijtens, S. D. Stranks, H. J. Snaith, M. Atature, R. T. Phillips, and R. H. Friend. "High Photoluminescence Efficiency and Optically Pumped Lasing in Solution-Processed Mixed Halide Perovskite Semiconductors". In: *Journal of Physical Chemistry Letters* 5.8 (2014), pp. 1421–1426. ISSN: 1948-7185.

[8] J. S. Manser and P. V. Kamat. "Band filling with free charge carriers in organonietal halide perovskites". In: *Nature Photonics* 8.9 (2014), pp. 737–743. ISSN: 1749-4885.

[9] B. Chen, Y. Bai, Z. S. Yu, T. Li, X. P. Zheng, Q. F. Dong, L. Shen, M. Boccard, A. Gruverman, Z. Holman, and J. S. Huang. "Efficient Semitransparent Perovskite Solar Cells for 23.0%-Efficiency Perovskite/Silicon Four-Terminal Tandem Cells". In: *Advanced Energy Materials* 6.19 (2016). ISSN: 1614-6832.

[10] D. Q. Bi, C. Y. Yi, J. S. Luo, J. D. Decoppet, F. Zhang, S. M. Zakeeruddin, X. Li, A. Hagfeldt, and M. Gratzel. "Polymer-templated nucleation and crystal growth of perovskite films for solar cells with efficiency greater than 21%". In: *Nature Energy* 1 (2016). ISSN: 2058-7546.

[11] H. P. Zhou, Q. Chen, G. Li, S. Luo, T. B. Song, H. S. Duan, Z. R. Hong, J. B. You, Y. S. Liu, and Y. Yang. "Interface engineering of highly efficient perovskite solar cells". In: *Science* 345.6196 (2014), pp. 542–546. ISSN: 0036-8075.

[12] W. S. Yang, J. H. Noh, N. J. Jeon, Y. C. Kim, S. Ryu, J. Seo, and S. I. Seok. "High-performance photovoltaic perovskite layers fabricated through intramolecular exchange". In: *Science* 348.6240 (2015), pp. 1234–1237. ISSN: 0036-8075.

[13] W. Y. Nie, H. H. Tsai, R. Asadpour, J. C. Blancon, A. J. Neukirch, G. Gupta, J. J. Crochet, M. Chhowalla, S. Tretiak, M. A. Alam, H. L. Wang, and A. D. Mohite. "High-efficiency solution-processed perovskite solar cells with millimeter-scale grains". In: *Science* 347.6221 (2015), pp. 522–525. ISSN: 0036-8075.

[14] G. C. Xing, N. Mathews, S. S. Lim, N. Yantara, X. F. Liu, D. Sabba, M. Gratzel, S. Mhaisalkar, and T. C. Sum. "Low-temperature solution-processed wavelength-tunable perovskites for lasing". In: *Nature Materials* 13.5 (2014), pp. 476–480. ISSN: 1476-1122.

[15] H. M. Zhu, Y. P. Fu, F. Meng, X. X. Wu, Z. Z. Gong, Q. Ding, M. V. Gustafsson, M. T. Trinh, S. Jin, and X. Y. Zhu. "Lead halide perovskite nanowire lasers with low lasing thresholds and high quality factors". In: *Nature Materials* 14.6 (2015), 636–U115. ISSN: 1476-1122.

[16] B. R. Sutherland, S. Hoogland, M. M. Adachi, C. T. O. Wong, and E. H. Sargent. "Conformal Organohalide Perovskites Enable Lasing on Spherical Resonators". In: *Acs Nano* 8.10 (2014), pp. 10947–10952. ISSN: 1936-0851.

[17] Z. K. Tan, R. S. Moghaddam, M. L. Lai, P. Docampo, R. Higler, F. Deschler, M. Price, A. Sadhanala, L. M. Pazos, D. Credgington, F. Hanusch, T. Bein, H. J. Snaith, and R. H. Friend. "Bright light-emitting diodes based on organometal halide perovskite". In: *Nature Nanotechnology* 9.9 (2014), pp. 687–692. ISSN: 1748-3387.

[18] J. Xing, F. Yan, Y. W. Zhao, S. Chen, H. K. Yu, Q. Zhang, R. G. Zeng, H. V. Demir, X. W. Sun, A. Huan, and Q. H. Xiong. "High-Efficiency Light-Emitting Diodes of Organometal Halide Perovskite Amorphous Nanoparticles". In: *Acs Nano* 10.7 (2016), pp. 6623–6630. ISSN: 1936-0851.

[19] S. Yakunin, L. Protesescu, F. Krieg, M. I. Bodnarchuk, G. Nedelcu, M. Humer, G. De Luca, M. Fiebig, W. Heiss, and M. V. Kovalenko. "Low-threshold amplified spontaneous emission and lasing from colloidal nanocrystals of caesium lead halide perovskites". In: *Nature Communications* 6 (2015). ISSN: 2041-1723.

[20] G. Nedelcu, L. Protesescu, S. Yakunin, M. I. Bodnarchuk, M. J. Grotevent, and M. V. Kovalenko. "Fast Anion-Exchange in Highly Luminescent Nanocrystals of Cesium Lead Halide Perovskites ($CsPbX_3$, X = Cl, Br, I)". In: *Nano Letters* 15.8 (2015), pp. 5635–5640. ISSN: 1530-6984.

[21] F. Zhang, H. Z. Zhong, C. Chen, X. G. Wu, X. M. Hu, H. L. Huang, J. B. Han, B. S. Zou, and Y. P. Dong. "Brightly Luminescent and Color-Tunable Colloidal $CH_3NH_3PbX_3$ (X = Br, I, Cl) Quantum Dots: Potential Alternatives for Display Technology". In: *Acs Nano* 9.4 (2015), pp. 4533–4542. ISSN: 1936-0851.

[22] D. M. Jang, K. Park, D. H. Kim, J. Park, F. Shojaei, H. S. Kang, J. P. Ahn, J. W. Lee, and J. K. Song. "Reversible Halide Exchange Reaction of Organometal Trihalide Perovskite Colloidal Nanocrystals for Full-Range Band Gap Tuning". In: *Nano Letters* 15.8 (2015), pp. 5191–5199. ISSN: 1530-6984.

[23] D. D. Zhang, S. W. Eaton, Y. Yu, L. T. Dou, and P. D. Yang. "Solution-Phase Synthesis of Cesium Lead Halide Perovskite Nanowires". In: *Journal of the American Chemical Society* 137.29 (2015), pp. 9230–9233. ISSN: 0002-7863.

[24] S. B. Sun, D. Yuan, Y. Xu, A. F. Wang, and Z. T. Deng. "Ligand-Mediated Synthesis of Shape-Controlled Cesium Lead Halide Perovskite Nanocrystals via Reprecipitation Process at Room Temperature". In: *Acs Nano* 10.3 (2016), pp. 3648–3657. ISSN: 1936-0851.

[25] H. L. Huang, F. C. Zhao, L. G. Liu, F. Zhang, X. G. Wu, L. J. Shi, B. S. Zou, Q. B. Pei, and H. Z. Zhong. "Emulsion Synthesis of Size-Tunable $CH_3NH_3PbBr_3$ Quantum Dots: An Alternative Route toward Efficient Light-Emitting Diodes". In: *Acs Applied Materials & Interfaces* 7.51 (2015), pp. 28128–28133. ISSN: 1944-8244.

[26] Y. Bekenstein, B. A. Koscher, S. W. Eaton, P. D. Yang, and A. P. Alivisatos. "Highly Luminescent Colloidal Nanoplates of Perovskite Cesium Lead Halide and Their Oriented Assemblies". In: *Journal of the American Chemical Society* 137.51 (2015), pp. 16008–16011. ISSN: 0002-7863.

[27] I. Lignos, S. Stavrakis, G. Nedelcu, L. Protesescu, A. J. Demello, and M. V. Kovalenko. "Synthesis of Cesium Lead Halide Perovskite Nanocrystals in a Droplet-Based Mi-

crofluidic Platform: Fast Parametric Space Mapping". In: *Nano Letters* 16.3 (2016), pp. 1869–1877. ISSN: 1530-6984.

[28] Y. Q. Xu, Q. Chen, C. F. Zhang, R. Wang, H. Wu, X. Y. Zhang, G. C. Xing, W. W. Yu, X. Y. Wang, Y. Zhang, and M. Xiao. "Two-Photon-Pumped Perovskite Semiconductor Nanocrystal Lasers". In: *Journal of the American Chemical Society* 138.11 (2016), pp. 3761–3768. ISSN: 0002-7863.

[29] F. R. Hu, H. C. Zhang, C. Sun, C. Y. Yin, B. H. Lv, C. F. Zhang, W. W. Yu, X. Y. Wang, Y. Zhang, and M. Xiao. "Superior Optical Properties of Perovskite Nanocrystals as Single Photon Emitters". In: *Acs Nano* 9.12 (2015), pp. 12410–12416. ISSN: 1936-0851.

[30] L. C. Schmidt, A. Pertegas, S. Gonzalez-Carrero, O. Malinkiewicz, S. Agouram, G. M. Espallargas, H. J. Bolink, R. E. Galian, and J. Perez-Prieto. "Nontemplate Synthesis of $CH_3NH_3PbBr_3$ Perovskite Nanoparticles". In: *Journal of the American Chemical Society* 136.3 (2014), pp. 850–853. ISSN: 0002-7863.

[31] S. Q. Huang, Z. C. Li, L. Kong, N. W. Zhu, A. D. Shan, and L. Li. "Enhancing the Stability of $CH_3NH_3PbBr_3$ Quantum Dots by Embedding in Silica Spheres Derived from Tetramethyl Orthosilicate in "Waterless" Toluene". In: *Journal of the American Chemical Society* 138.18 (2016), pp. 5749–5752. ISSN: 0002-7863.

[32] Y. Kim, E. Yassitepe, O. Voznyy, R. Comin, G. Walters, X. W. Gong, P. Kanjanaboos, A. F. Nogueira, and E. H. Sargent. "Efficient Luminescence from Perovskite Quantum Dot Solids". In: *Acs Applied Materials & Interfaces* 7.45 (2015), pp. 25007–25013. ISSN: 1944-8244.

[33] Vadim V Lozovoy, Igor Pastirk, and Marcos Dantus. "Multiphoton intrapulse interference IV Ultrashort laser pulse spectral phase characterization and compensation". EN. In: *Optics Letters* 29.7 (Apr. 2004), p. 775. ISSN: 0146-9592.

[34] J. De Roo, M. Ibanez, P. Geiregat, G. Nedelcu, W. Walravens, J. Maes, J. C. Martins, I. Van Driessche, M. V. Koyalenko, and Z. Hens. "Highly Dynamic Ligand Binding and Light Absorption Coefficient of Cesium Lead Bromide Perovskite Nanocrystals". In: *Acs Nano* 10.2 (2016), pp. 2071–2081. ISSN: 1936-0851.

[35] K. Tanaka, T. Takahashi, T. Ban, T. Kondo, K. Uchida, and N. Miura. "Comparative study on the excitons in lead-halide-based perovskite-type crystals $CH_3NH_3PbBr_3$ $CH_3NH_3PbI_3$". In: *Solid State Communications* 127.9-10 (2003), pp. 619–623. ISSN: 0038-1098.

[36] A. Halpin, P. J. M. Johnson, R. Tempelaar, R. S. Murphy, J. Knoester, T. L. C. Jansen, and R. J. D. Miller. "Two-dimensional spectroscopy of a molecular dimer unveils the effects of vibronic coupling on exciton coherences". In: *Nature Chemistry* 6.3 (2014), pp. 196–201. ISSN: 1755-4330.

CHAPTER 5

TWO-DIMENSIONAL ELECTRONIC SPECTROSCOPY OF CDSE NANOPLATELETS THIN FILMS

5.1 Introduction

Colloidal semiconductor nanocrystals have been extensively researched for the past three decades because their unique optical properties can transform modern technologies from consumer displays to biomedical imaging. These materials are quantum confined, and their optical properties are dependent on their size and shape, as well as their chemical composition. CdSe Nanoplatelets (NPLs) are colloidal nanocrystals that are quantum confined in one dimension and have garnered recent interest for their ability to act as a low-threshold lasing gain medium.[1–6] CdSe NPLs have extremely narrow absorption and emission lines because the confined height of the material is synthetically controllable with atomic precision. This drastically reduces inhomogeneous broadening compared to other types of nanocrystal preparations, with single particle studies showing that the linewidths of single nanoplatelets and the ensemble are nearly identical. Additionally, the excitons that are formed after light absorption do not couple strongly to phonon modes, reducing their homogeneous linewidths compared to material such as 0D CdSe or InP quantum dots.[7] While these extremely narrow features make CdSe NPLs excellent candidates for a number of optoelectronic applications, the lateral dimensions of NPLs are large enough to accommodate many excitons on a single platelet, facilitating population inversion and making NPLs an excellent lasing gain medium with low amplified stimulated emission thresholds as well.[2, 3] Since their development in 2008, NPLs with heights of 2-5 monolayers (MLs) and recently 6 monolayers of CdSe have been reported as well as heterostructured NPLs.[8–14] The different ML thicknesses of various NPL syntheses produce emission lines at 396 nm (2 ML), 463 nm (3 ML), 513 nm (4 ML), 553 nm (5 ML), and 583 nm (6 ML). Previous studies of these materials have revealed that CdSe NPLs preferentially form coupled electron-hole pairs called excitons rather than form-

ing free charge carriers after being excited. Additioanlly, these excitons exhibit second order decay kinetics from the band-edge states, even at type-II heterojunction interfaces.[6] CdSe NPLs also show second order kinetics during Auger recombination, which is usually a three-body process involving an electron-hole pair and a free carrier, but here proceeds through a biexciton mechanism.[15, 16] The band-edge exciton consists of a bright and dark state separated by a few meV, which is an order of magnitude larger than epitaxial quantum well systems of II-VI materials, and the recombination times of the bright and dark excitons are an order of magnitude faster than colloidal CdSe quantum dots.[17] Finally, two-dimensional electronic spectroscopy (2DES) studies have shown that CdSe NPLs exhibit electronic coherence at room temperature between the two lowest lying excitonic states, making this material very interesting to easily observe the nature of quantum coherence in a model system.[18, 19] In this work, 2DES is used to examine the electronic structure of 6 ML CdSe NPLs to first determine if their ultrafast behavior is similar to other realizations of CdSe NPLs and to identify power and temperature-dependent trends on the carrier dynamics and electronic coherences of excitons in these core-only nanoplatelet systems. This will help to reveal early time dynamics between bright and dark band edge states and learn more about the nature of excitonic coherences in materials systems with relatively simple electronic structure to inform our characterization of quantum beating in most complex environments such as bacterial photosynthetic complexes.

5.2 Methods

5.2.1 Synthesis of 6 ML CdSe Nanoplatelets

The 6 ML core-only CdSe nanoplatelets for this experiment were prepared according to the synthetic procedures described in Cho et al.[11] 170 mg of cadmium myristate and 14 mL of 1-octadecene (ODE) are combined in a 100 mL three-neck round-bottom flask and degassed under vacuum at 85 C for 30 min. Then, after heating to 250 C under nitrogen, 12 mg of Se

powder dispersed in 1 mL of ODE is injected into the reaction flask and stirred vigorously for 20 s. At this point, 60 mg of cadmium acetate hydrate is added to the flask and stirred for another 60 s. Next, 0.15 mL of 0.5 M cadmium chloride aqueous solution is slowly added into the flask dropwise over 2 minutes. After another 3 minutes, the flask is rapidly cooled to room temperature using compressed air. Once the reaction flask has cooled to about 150 C, a solution of 2 mL of oleic acid in 15 mL of methylcyclohexane (MCH) is injected into the flask. The solution is then centrifuged and dispersed in MCH and smaller particles are removed via size-selective precipitation. To be prepared for the 2DES experiments, the resulting 6 ML CdSe NPLs were spin-coated onto a glass substrate to a thickness that yielded an approximately 0.1 OD absorbance for the band-edge exciton at 583 nm.

5.2.2 Two-Dimensional Electronic Spectroscopy

2D Electronic Spectra were obtained using a home-built four wave mixing apparatus that has been described previously.[20] A Ti:sapphire regenerative amplifier (Legend Elite, Coherent) was seeded by the output of a Ti:sapphire oscillator (Micra, Coherent), producing 35 fs pulses centered at 805 nm, with an average power of 640 uJ/pulse. This output was focused to a 2 m long, closed tube filled with Ar gas at 13 psi, with a 1 m focal length lens, and recollimated at the tube's output. Through a self-phase modulation process, the light was broadened in the tube to approximately 100 nm bandwidth FWHM supercontinuum centered at 770 nm, with tails stretching from 400 nm to 900 nm. This spectrum was turned using a cold mirror to block light red of 710 nm, resulting in a final output spectrum centered at 620 nm with a bandwidth of 150 nm FWHM. After exiting the tube, the beam is sent to a pair of chirped mirrors to compensate for higher order dispersion introduced by the white light generation process. Since the CdSe NPL samples considered in the experiment do not absorb or emit light red of 600 nm, the spectrum was further cut using a mask placed after a diffractive grating to give a soft edge at 600 nm, aiding in compression. The dispersion is then corrected further, and the pulses are compressed to 12 fs at the sample

position using a multiphoton intrapulse interference phase scan (MIIPS)[21] method and a spatial light modulator (MIIPSBox 640, Biophotonics Solutions). In our BOXCARS 2DES measurements, three pulses interact with the sample, in this case a spin coated thin film of 6 ML CdSe NPLs on a glass substrate, with an average pulse power ranging between 100 pJ/pulse and 10 nJ/pulse, focused to a 100 um spot size. The resulting third order signal is generated in a phase-matched direction and heterodyne detected with a weak fourth pulse, called the local oscillator, and recorded on a CCD camera (Andor Newton) thermoelectrically cooled to -50 C. The time delay between the first and second pulse is called the coherence time (tau). The delay between the second and third pulses is called the waiting time (T). Finally, the delay between the third pulse and the third-order signal is the rephasing time (t). By Fourier transforming over the tau and t time domains, a frequency-frequency map relating the excitation energy to the detected frequency axis as a function of T, which is the 2D electronic spectrum. In these measurements the coherence time delay was scanned from -90 fs to 90 fs in step sizes of 1.5 fs. However, it should be noted that for experiments involving materials like CdSe NPLs, with potentially long-lasting electronic coherences at low temperatures, it may be necessary to extend this time range to avoid artifacts caused by truncating the time-domain signal. In these experiments, we use multiple pump fluences, ranging from 200 pJ/pulse to 2 nJ/pulse. These powers should all be lower than the fluence necessary to excite multiple excitons onto a single platelet,[15] which will allow us to examine the power dependent relaxation dynamics while avioiding many-body interactions that will complicate the analysis. Each 2DES experiment was performed at both room temperature and at 77K in a continuous flow cryostat (Cryo Industries), and room temperature experiements were taken under a nitrogen atmosphere to prevent oxidative photodamage.

5.3 Results and Discussion

The electronic structure of the 6 ML CdSe NPLs resembles a quantum well system, with heavy hole, light hole, and split-off valence sub-bands as well as multiple conduction sub-

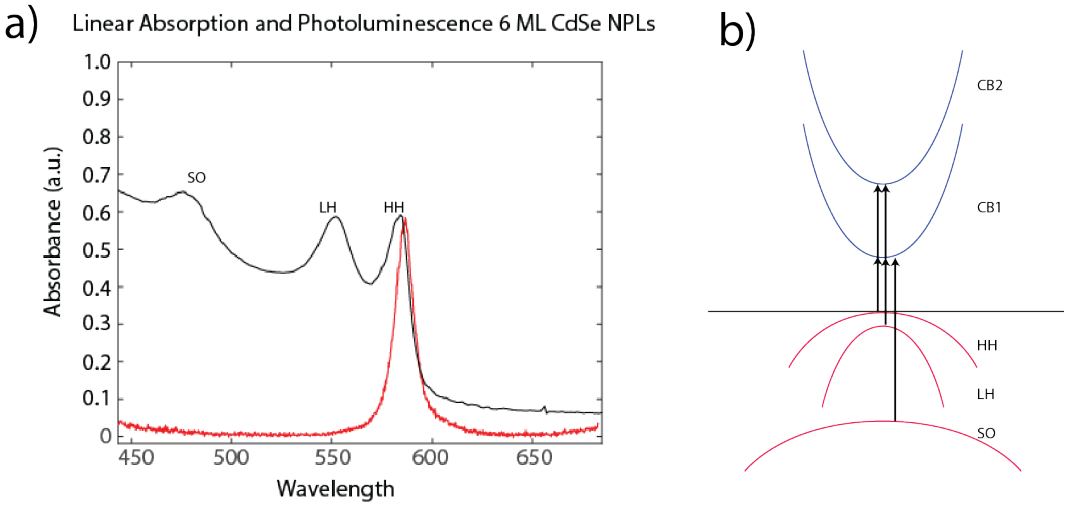

Figure 5.1: a) Absorption (black) and emission (red) spectra of a thin film of 6 ML CdSe nanoplatelets. The three lowest-lying transitions can be seen, and are labelled as the heavy hole (HH), light hole (LH), and split-off (SO) states. b) An illustrative band diagram of CdSe nanoplatelets is shown with relevant bands and transitions. There are two conduction bands, CB1 and CB2. The valence bands include the heavy hole band (HH), the light hole band (LH), and the split-off band (SO).

bands (Figure 5.1b). Three excitonic states arise from transitions to the lowest conduction sub-band and occur at 583 nm (HH), 551 nm (LH), 477 nm (SO), 392 nm (HH2), and 364 nm (LH2). Due to the spectral range of our 2DES setup, we will focus on the HH and LH transitions as well as the photoluminescence band at 590 nm, slightly Stokes shifted from the HH transition. Two-dimensional electronic spectroscopy is an excellent technique for studying these types of quantum well systems due to it ability to gain higher frequency resolution than transient absorption techniques by spreading the nonlinear signal onto two axes, and by tracking state-to-state coupling and energy transfer dynamics with sub-10 fs time resolution.[22–26] Multidimensional optical spectroscopies have been successfully used previously to probe two-dimensional semiconductor systems and their interesting multiexciton interactions[27–30] and room temperature electronic coherences,[18, 19].

CdSe nanoplatelets synthesized by the methods above were used for two-dimensional electronic spectroscopy experiments. Figure 5.1a shows the linear absorption and emission spectra for 6 ML CdSe NPLs at room temperature after spin-coating the particles onto a glass

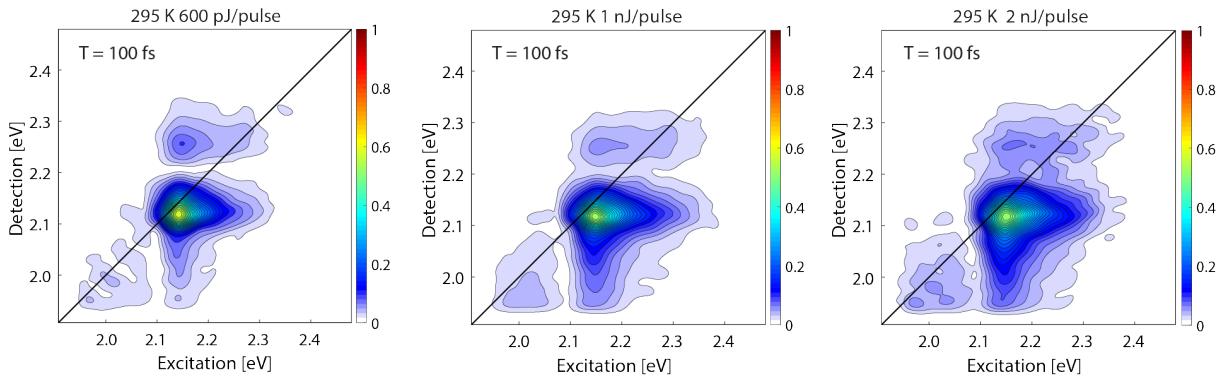

Figure 5.2: Absolute-valued 2D spectra of a thin film of 6 ML CdSe nanoplatelets at room temperature and at 100 fs with different pump laser fluences. a) 600 pJ/pulse b) 1 nJ/pulse c) 2 nJ/pulse. Each spectrum is normalized to the maximum value of their respective data sets.

substrate. Very sharp heavy hole (HH) and light hole (LH) states occur at approximately 585 nm and 550 nm, respectively, with little noticeable impurities, which would appear as spectral features below the bandgap. The photoluminescence band is very sharp and occurs slightly Stokes shifted from the absorption maximum.

Two-dimensional electronic spectroscopy (2DES) measurements were performed on the thin film samples both at room temperature and 77K in a continuous flow cryostat. All spectra were obtained for short time scales (-20 fs to 200 fs) to better study the ultrafast dynamics such as electronic coherences and the initial carrier relaxation after excitation. The laser spectrum is well temporally compressed from 650 nm to 550 nm, providing access to the HH and LH excitons. In Figure 5.2, room temperature 2D spectra of 6 ML CdSe nanoplatelets are shown. The spectra are taken with different pulse powers ranging from 600 pJ/pulse (3 μW average power) to 2 nJ/pulse (10 μW average power), which even at our high power range should be below the peak fluence required to produce multiple excitons per platelet, eliminating potential artifacts from higher order nonlinear signals.[15]

In all three of these spectra, the HH feature at 2.13 eV (585 nm) is clearly resolved. In addition, the LH state appears as a weak feature on the diagonal due to fast energy transfer to the band edge. This energy transfer concurrently results in a lower-diagonal cross-peak feature that grows in at an excitation energy of 2.27 eV and a detection energy of 2.13

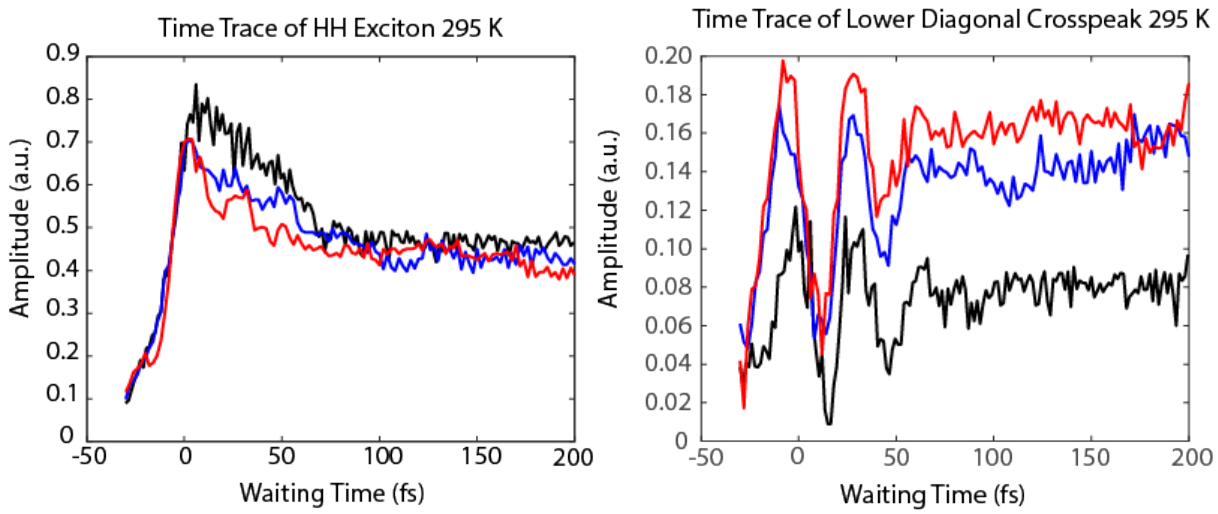

Figure 5.3: Waiting time traces of excitonic features in the 2D spectra of 6 ML CdSe nanoplatelets at room temperature. a) Traces of the decay at the heavy hole excitonic feature [black - 600 pJ/pulse, blue - 1 nJ/pulse, red - 2 nJ/pulse] b) Traces of the lower diagonal crosspeak between the heavy hole and light hole states [black - 600 pJ/pulse, blue - 1 nJ/pulse, red - 2 nJ/pulse]. All traces are normalized to the maximum value of the 2D spectrum across all waiting times for each data set.

eV. The final prominent peak in the spectrum is an upper-diagonal feature (2.13 eV, 2.27 eV), which indicates coupling between the HH and LH excitons. Along with these spectra features, a tail extends along the detection axis to the red of the HH exciton. This indicates that some amplitude is being absorbed into the HH state, and over the course of just 100 fs, relaxing likely into mid-gap trap states. Also, direct absorption into these trap states is observed by the presence of amplitude on the diagonal, but red of the HH exciton energy. The spectra also clearly show slight differences as a function of the pump power. The most noticeable change is an increased transfer from the HH exciton into mid-gap trap states.

Figure 5.3 shows the waiting time traces for both the HH exciton and the lower diagonal cross-peak, which represents energy transfer from the LH state to the HH state for the three powers mentioned above (600 pJ/pulse – black, 1 nJ/pulse – blue, 2 nJ/pulse – red). For all three samples, there is a biexponential decay of the HH exciton amplitude with a sub-40 fs time constant, followed by a much longer decay from the photoluminescent state. The three powers do not vary by a significant amount, although it seems that the initial decay

occurs more rapidly for higher fluences. The lower diagonal cross-peak shows electronic coherence at room temperature, similar to previous 2DES studies on CdSe NPLs.[18, 19] In the first 50 fs, very prominent oscillations occur with a frequency of approximately 125 meV, near the electronic energy gap between the HH and LH states. This coherence persists throughout the lower diagonal, shifting from lower to higher frequency as the energy gap changes. Additionally, the intensity of the coherence appears to increase at higher pump fluences.

For the samples at 77K (Figure 5.4), the spectral features maintain the same four peak pattern as the room temperature data, but with a blue-shifted band gap, due to temperature-dependent lattice dilation and changes in the electron-lattice interaction.[31] The HH exciton shifts to 2.20 eV (563 nm) at 77K, while the LH excitonic features shifts to 2.32 eV (534 nm). Compared to room temperature scans, these spectra are much noisier. This is due to both the spectral features approaching upper frequency limit of what this current 2DES setup can probe, and minute fluctuations in the sample position due to the nature of the continuous flow cryostat. The latter issue is exacerbated by using thin films, since the path length and hence the phase-matched volume is very small, allowing slight changes to have large impacts on the signal-to-noise of the resulting spectra.

Another issue that arose working with the films at low temperature was apparent photobleaching. This is a common issue with these materials when working in the solution phase or in air. These point-by-point 2DES experiments take on the order of 8 hours for a single run. We found that if the NPL sample is simply suspended in toluene at 0.3 OD in a 200 μm sample cell, aggregation and photobleaching will occur over the course of a single run even while using low fluences (500 pJ/pulse).[32] Similarly, if thin film samples are left in air, photobleaching will occur quickly after beginning the experiments under low fluences. Therefore, as mentioned earlier, all room temperature data was taken under a nitrogen environment in the cryostat to circumvent these issues. However, when taking 77K data, we once again observe apparent bleaching at all powers above 200 pJ/pulse. Figure 5.5 shows the waiting

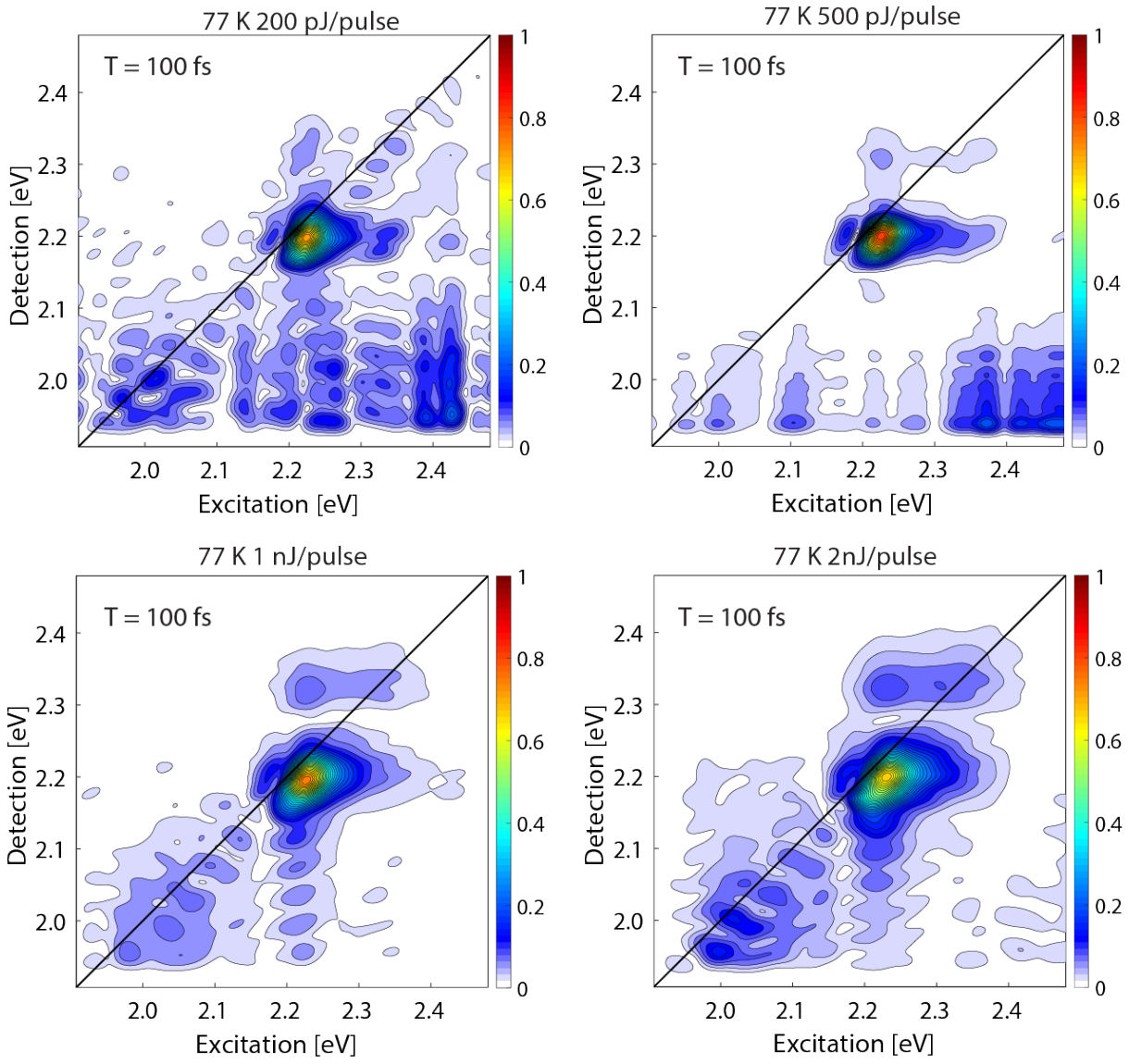

Figure 5.4: Absolute-valued 2D spectra of a thin film of 6 ML CdSe nanoplatelets at 77 K and at 100 fs with different pump laser fluences. a) 200 pJ/pulse b) 500 pJ/pulse c) 1 nJ/pulse d) 2 nJ/pulse. Each spectrum is normalized to the maximum value of their respective data sets

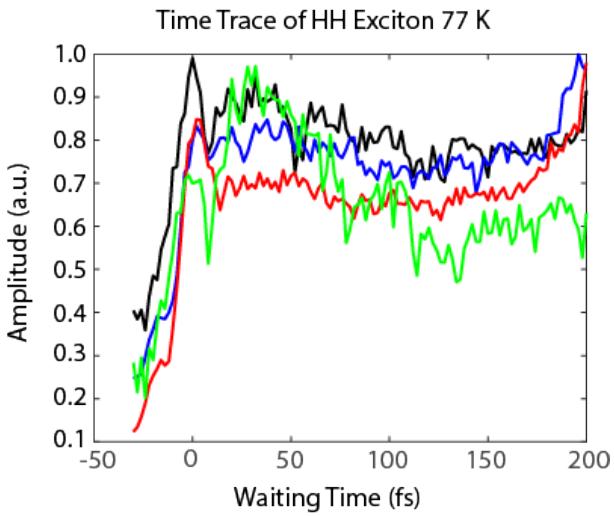

Figure 5.5: Waiting time traces of the heavy hole excitonic feature in the 2D spectra of 6 ML CdSe nanoplatelets at 77 K [green - 200 pJ/pulse, black - 500 pJ/pulse, blue - 1 nJ/pulse, red - 2 nJ/pulse]

time traces for the HH exciton. These traces are obtained by scanning backwards in time. Therefore, the last time point (200 fs) is the first one to be scanned, and the waiting time is scanned backwards with step sizes of 2 fs until -20 fs. A telltale sign of photobleaching is a degradation in the signal amplitude over the course of the experiment, which is not so obvious to detect when taking a normal scan. However, if the waiting time is scanned backwards, the later time points will be the highest amplitude, producing an a-physical time trace in the 2D spectrum. This effect is clearly seen in Figure 5.5, comparing the 200 pJ/pulse, which rises and then decays, with the three higher power scans that peak at the beginning of the experiment and longer waiting times. This behavior is fairly counterintuitive and though it may be simply a result of photodegredation, it is also possible that the system remains in an excited state and we are observing a hole-burning effect. This could happen for example if some excited state population relaxes to a very long lived dark exciton state at low temperatures that is not thermally able to easily relax back to the photoluminescent state on the order of our shot-to-shot laser delays. It will be very interesting to observe the photophysics of this material and more experiments should be carried out at a series of temperatures from room temperature to 77K to determine if this effect switches on at a certain point.

5.4 Conclusion

CdSe Nanoplatelets are a promising material for low-threshold lasing applications. Much recent progress has been made in both synthesis of novel platelet thicknesses and architectures. This work used two-dimensional electronic spectroscopy to probe the electronic structure and ultrafast relaxation dynamics of excitons in 6 ML CdSe NPL thin films. Spectra were obtained for various powers, all below the multi-exciton regime and at both room temperature and 77K. The spectra show interesting behavior such as room temperature electronic coherences, and very fast decay dynamics on the order of 50 fs. Spectra taken at cold temperature show good signal and well-defined spectral features, however scatter from the thin films, laser bandwidth, and photobleaching at relatively low pump fluences remain issues that should be explored in future work.

REFERENCES

[1] Mickael D Tessier, Louis Biadala, Cecile Bouet, Sandrine Ithurria, Benjamin Abecassis, and Benoit Dubertret. "Phonon Line Emission Revealed by Self-Assembly of Colloidal Nanoplatelets". In: *Acs Nano* 7.4 (2013), pp. 3332–3340. ISSN: 1936-0851.

[2] Chunxing She, Igor Fedin, Dmitriy S Dolzhnikov, Arnaud Demortiere, Richard D Schaller, Matthew Pelton, and Dmitri V Talapin. "Low-Threshold Stimulated Emission Using Colloidal Quantum Wells". In: *Nano Letters* 14.5 (2014), pp. 2772–2777. ISSN: 1530-6984.

[3] Chunxing She, Igor Fedin, Dmitriy S Dolzhnikov, Peter D Dahlberg, Gregory S Engel, Richard D Schaller, and Dmitri V Talapin. "Red, Yellow, Green, and Blue Amplified Spontaneous Emission and Lasing Using Colloidal CdSe Nanoplatelets". In: *Acs Nano* 9.10 (2015), pp. 9475–9485. ISSN: 1936-0851.

[4] Matthew Pelton, Sandrine Ithurria, Richard D Schaller, Dmitriy S Dolzhnikov, and Dmitri V Talapin. "Carrier Cooling in Colloidal Quantum Wells". In: *Nano Letters* 12.12 (Dec. 2012), pp. 6158–6163. ISSN: 1530-6984.

[5] Michel Nasilowski, Benoit Mahler, Emmanuel Lhuillier, Sandrine Ithurria, and Benoit Dubertret. "Two-Dimensional Colloidal Nanocrystals". In: *Chemical Reviews* 116.18 (Sept. 2016), pp. 10934–10982. ISSN: 0009-2665.

[6] Riccardo Scott, Sebastian Kickhoefel, Oliver Schoeps, Artsiom Antanovich, Anatol Prudnikau, Andrey Chuvilin, Ulrike Woggon, Mikhail Artemyev, and Alexander W Achtstein. "Temperature dependent radiative and non-radiative recombination dynamics in CdSe-CdTe and CdTe-CdSe type II hetero nanoplatelets". In: *Physical Chemistry Chemical Physics* 18.4 (2016), pp. 3197–3203. ISSN: 1463-9076.

[7] Alexander W Achtstein, Andrei Schliwa, Anatol Prudnikau, Marya Hardzei, Mikhail V Artemyev, Christian Thomsen, and Ulrike Woggon. "Electronic Structure and Exciton–Phonon Interaction in Two-Dimensional Colloidal CdSe Nanosheets". In: *Nano Letters* 12.6 (June 2012), pp. 3151–3157. ISSN: 1530-6984.

[8] Sandrine Ithurria and Benoit Dubertret. "Quasi 2D Colloidal CdSe Platelets with Thicknesses Controlled at the Atomic Level". In: *Journal of the American Chemical Society* 130.49 (2008), pp. 16504–+. ISSN: 0002-7863.

[9] S Ithurria, M D Tessier, B Mahler, R P S M Lobo, B Dubertret, and Al L Efros. "Colloidal nanoplatelets with two-dimensional electronic structure". In: *Nature Materials* 10.12 (2011), pp. 936–941. ISSN: 1476-1122.

[10] Cecile Bouet, Benoit Mahler, Brice Nadal, Benjamin Abecassis, Mickael D Tessier, Sandrine Ithurria, Xiangzhen Xu, and Benoit Dubertret. "Two-Dimensional Growth of CdSe Nanocrystals, from Nanoplatelets to Nanosheets". In: *Chemistry of Materials* 25.4 (2013), pp. 639–645. ISSN: 0897-4756.

[11] Wooje Cho, Siyoung Kim, Igor Coropceanu, Vishwas Srivastava, Benjamin T. Diroll, Abhijit Hazarika, Igor Fedin, Giulia Galli, Richard D. Schaller, and Dmitri V. Talapin. "Direct Synthesis of Six-Monolayer (1.9 nm) Thick Zinc-Blende CdSe Nanoplatelets Emitting at 585 nm". In: *Chemistry of Materials* 30.20 (Oct. 2018), pp. 6957–6960. ISSN: 0897-4756.

[12] Benoit Mahler, Brice Nadal, Cecile Bouet, Gilles Patriarche, and Benoit Dubertret. "Core/Shell Colloidal Semiconductor Nanoplatelets". In: *Journal of the American Chemical Society* 134.45 (2012), pp. 18591–18598. ISSN: 0002-7863.

[13] Mickaël D. Tessier, Piernicola Spinicelli, Dorian Dupont, Gilles Patriarche, Sandrine Ithurria, and Benoit Dubertret. "Efficient Exciton Concentrators Built from Colloidal Core/Crown CdSe/CdS Semiconductor Nanoplatelets". In: *Nano Letters* 14.1 (Jan. 2014), pp. 207–213. ISSN: 1530-6984.

[14] Yijie Yang, Chaojian Zhang, Xiangwei Qu, Wenda Zhang, Mikita Marus, Bing Xu, Kai Wang, and Xiaowei Sun. "High quantum yield colloidal semiconducting nanoplatelets and high color purity nanoplatelet QLED". In: *IEEE Transactions on Nanotechnology* (2019), pp. 1–1. ISSN: 1536-125X.

[15] Lucas T. Kunneman, Mickael D. Tessier, Hadrien Heuclin, Benoit Dubertret, Yaroslav V. Aulin, Ferdinand C. Grozema, Juleon M. Schins, and Laurens D.A. Siebbeles. "Bimolecular auger recombination of electron-hole pairs in two-dimensional CdSe and CdSe/CdZnS core/shell nanoplatelets". In: *Journal of Physical Chemistry Letters* 4.21 (Nov. 2013), pp. 3574–3578. ISSN: 19487185.

[16] Clare E Rowland, Igor Fedin, Hui Zhang, Stephen K Gray, Alexander O Govorov, Dmitri V Talapin, and Richard D Schaller. "Picosecond energy transfer and multiexciton transfer outpaces Auger recombination in binary CdSe nanoplatelet solids". In: *Nature Materials* 14.5 (2015), pp. 484–489. ISSN: 1476-1122.

[17] Louis Biadala, Feng Liu, Mickael D. Tessier, Dmitri R. Yakovlev, Benoit Dubertret, and Manfred Bayer. "Recombination Dynamics of Band Edge Excitons in Quasi-Two-Dimensional CdSe Nanoplatelets". In: *Nano Letters* 14.3 (Mar. 2014), pp. 1134–1139. ISSN: 1530-6984.

[18] Elsa Cassette, Ryan D. Pensack, Benoît Mahler, and Gregory D. Scholes. "Room-temperature exciton coherence and dephasing in two-dimensional nanostructures". In: *Nature Communications* 6.1 (Dec. 2015), p. 6086. ISSN: 2041-1723.

[19] E. Cassette, S. Pedetti, B. Mahler, S. Ithurria, B. Dubertret, and G. D. Scholes. "Ultrafast exciton dynamics in 2D in-plane hetero-nanostructures: delocalization and charge transfer". In: *Physical Chemistry Chemical Physics* 19.12 (Mar. 2017), pp. 8373–8379. ISSN: 1463-9076.

[20] Haibin Zheng, Justin R Caram, Peter D Dahlberg, Brian S Rolczynski, Subha Viswanathan, Dmitriy S Dolzhnikov, Amir Khadivi, Dmitri V Talapin, and Gre-

gory S Engel. “Dispersion-free continuum two-dimensional electronic spectrometer”. In: *Applied Optics* 53.9 (2014), pp. 1909–1917. ISSN: 1559-128X.

[21] Vadim V Lozovoy, Igor Pastirk, and Marcos Dantus. “Multiphoton intrapulse interference IV Ultrashort laser pulse spectral phase characterization and compensation”. EN. In: *Optics Letters* 29.7 (Apr. 2004), p. 775. ISSN: 0146-9592.

[22] T Brixner, T Mancal, I V Stiopkin, and G R Fleming. “Phase-stabilized two-dimensional electronic spectroscopy”. In: *Journal of Chemical Physics* 121.9 (2004), pp. 4221–4236. ISSN: 0021-9606.

[23] Yuan-Chung Cheng and Graham R Fleming. “Coherence Quantum Beats in Two-Dimensional Electronic Spectroscopy”. In: *The Journal of Physical Chemistry A* 112.18 (May 2008), pp. 4254–4260. ISSN: 1089-5639.

[24] Minhaeng Cho. “Coherent Two-Dimensional Optical Spectroscopy”. en. In: *Chemical Reviews* 108.4 (Apr. 2008), pp. 1331–1418. ISSN: 0009-2665.

[25] Minhaeng Cho, Tobias Brixner, Igor Stiopkin, Harsha Vaswani, and Graham R Fleming. “Two Dimensional Electronic Spectroscopy of Molecular Complexes”. In: *Journal of the Chinese Chemical Society* 53.1 (2006), pp. 15–24.

[26] Minhaeng Cho, Harsha M Vaswani, Tobias Brixner, Jens Stenger, and Graham R. Fleming. “Exciton Analysis in 2D Electronic Spectroscopy”. en. In: *The Journal of Physical Chemistry B* 109.21 (June 2005), pp. 10542–10556. ISSN: 1520-6106.

[27] Katherine W Stone, Kenan Gundogdu, Daniel B Turner, Xiaoqin Li, Steven T Cundiff, and Keith A Nelson. “Two-quantum 2D FT electronic spectroscopy of biexcitons in GaAs quantum wells.” In: *Science (New York, N.Y.)* 324.5931 (May 2009), pp. 1169–73. ISSN: 1095-9203.

[28] Daniel B. Turner and Keith A. Nelson. “Coherent measurements of high-order electronic correlations in quantum wells”. In: *Nature* 466.7310 (Aug. 2010), pp. 1089–1092. ISSN: 0028-0836.

[29] Tianhao Zhang, Irina Kuznetsova, Torsten Meier, Xiaoqin Li, Richard P Mirin, Peter Thomas, and Steven T Cundiff. "Polarization-dependent optical 2D Fourier transform spectroscopy of semiconductors." In: *Proceedings of the National Academy of Sciences of the United States of America* 104.36 (Sept. 2007), pp. 14227–32. ISSN: 0027-8424.

[30] Xiaoqin Li, Tianhao Zhang, Camelia N. Borca, and Steven T. Cundiff. "Many-Body Interactions in Semiconductors Probed by Optical Two-Dimensional Fourier Transform Spectroscopy". In: *Physical Review Letters* 96.5 (Feb. 2006), p. 057406. ISSN: 0031-9007.

[31] Y. P. Varshni. "Temperature dependence of the energy gap in semiconductors". In: *Physica* 34.1 (1967), pp. 149–154.

[32] Santanu Jana, Trang N T Phan, Cecile Bouet, Mickael D Tessier, Patrick Davidson, Benoit Dubertret, and Benjamin Abecassis. "Stacking and Colloidal Stability of CdSe Nanoplatelets". In: *Langmuir* 31.38 (2015), pp. 10532–10539. ISSN: 0743-7463.

CHAPTER 6

PROPOSED DIRECTIONS FOR FUTURE RESEARCH

Semiconductor nanocrystals are a fascinating group of functional materials that can have profound impacts on the development of all sorts of optoelectronic devices due to their unique chemistry. In these materials, chemists aim to engineer an electronic wavefunction by changing the size, shape, and environment of the nanocrystal, while not changing the underlying chemical composition of the material. This creates a wide array of potential opportunities to create novel device architectures but has the drawback that it is difficult to measure these mesoscale materials themselves. Nanocrystals are very small, but also contain thousands more atoms than small molecules, which have well-optimized analytical techniques for compound development and discovery. Several techniques have been used in this thesis to understand the size, shape, composition, crystal structure, and optoelectronic properties of these materials, however we have also shown that small, difficult to detect defect states can have major implications for the material behavior. Additionally, no two nanocrystals are identical, and it can be very difficult to segment the nanocrystal ensemble by the proper type of inhomogeneity, whether it is size and shape, or defect type, placement, and concentration. Also, other sources of inhomogeneity related to the environment, particularly in thin film materials that have substrate grain boundaries and complex interfacial carrier dynamics are a difficult challenge in developing functional devices from nanocrystals.

The work presented in this thesis focuses on using multidimensional spectroscopic techniques like two-dimensional electronic spectroscopy (2DES), exactly because they are an excellent way to segment sources of spectral broadening and inhomogeneity. Through our experiments, we have shown that 2DES is a powerful technique that can complement other spectroscopic tools and microscopy experiments to characterize nanocrystals and understand the design principles that could lead to more efficient device technologies. However, there are many more problems that relate to interesting types of inhomogeneity that 2DES and our group would be well suited to solve. In this section, I present possible directions that our

group could explore that could be fruitful for understanding and developing nanocrystalline materials for lighting, display, and solar cell applications. In the first part of this chapter, I describe possible extensions to the studies that we performed in chapters 3 and 4. In these chapters we perform 2DES experiments on solution-phase InP and lead-halide perovskite quantum dots (QDs). However, extending these studies to thin films will give data on how these materials will respond in an environment similar to real devices. Then, in the second half of this chapter, I will talk about the potential in studying I-III-VI QDs, which share similar problems to the one explored in chapter 3. Materials like $CuInSe_2$ QDs have broad emission spectra due to recombination via dopant-related trap states, and the capabilities of 2DES to differentiate the types and properties of these defect states and how they effect the electronic structure and carrier dynamics should prove to provide an exciting research direction for our group.

6.1 Further studies of InP Quantum Dots

InP quantum dots (QDs) are a promising competitor to CdSe as a material for consumer lighting and display devices due to its structural similarity to CdSe and its relatively lower biotoxicity. In chapter 3 of this thesis, we studied InP QDs to understand their broad emission spectra using two-dimensional electronic spectroscopy (2DES). Our experiments were carried out using InP QDs solubilized in toluene with a concentration of 0.3 OD in a 200 μm sample cell. However, while studying colloidal solutions of InP QDs is useful at a fundamental level, these QDs will ultimately be used in real devices and solution-phase spectroscopy may not adequately describe how the QDs will respond in a thin film environment. It is probable that in transitioning from the solution phase to a thin film, the electronic structure and coupling between QDs could change significantly since this removes the low dielectric constant solvent and decreases the average inter-particle distance. It has been shown that InP quantum dots in a thin film environment can couple strongly to one another, allowing for efficient inter-particle energy transfer from smaller dots to larger ones.[1]

This phenomenon along with other potential changes in the InP coupling and electronic structure could be elucidated with great detail using 2DES, which is very useful for isolating energy transfer pathways and couplings between electronic states even in highly scattering, multi-chromophoric systems.[2, 3] We have explored using thin film samples for 2DES during our experiments on CdSe nanoplatelet thin films and know from previous studies on a variety of thin film semiconductor systems that for a sample with relatively a relatively low scatter/absorbance ratio it should be possible to collect high quality 2D spectra.[4–6] An added advantage gained by using thin films in our experiments is that it makes low temperature studies of these nanomaterials more accessible. Typical solvents used in nanomaterial synthesis like hexane, toluene, and even water are difficult to perform solution-phase low temperature 2DES studies on because it is difficult to form very good glasses with these solvents, producing high scatter samples. Thin films circumvent this issue by eliminating the solvent and multiple 2DES studies including our own in chapter 5 have shown that it is possible to obtain very good signal to noise. Low temperature studies of InP QD thin films would be very useful as they could not only describe differences between solution phase and thin film carrier dynamics, coupling, and electronic structure, but studies near 10 K would provide an outlet to study the interaplay between carrier relaxation and excitonic fine structure, particularly when bright-dark splittings at the conduction band edge are present.[7] Unlike the studies of CdSe nanoplatelets, low temperature studies of InP quantum dots are also much more accessible by our current 2DES setup since the band edge is much redder than the 6 ML NPLs, allowing us to capture the spectral shape and dynamics of the band-edge excitons and photoluminescence peak after cooling.

6.2 Electronic Structure and Femtosecond Dynamics of Cd-Free Quantum Dots

Along with InP QDs, other Cd-free and Pb-free QDs have seen increased academic and industrial interest in past years due to their relatively low toxicity compared with materials like CdSe, CdTe, and PbS QDs. The lack of toxic heavy metals is an important market driver in the development of novel consumer display and solar cell technologies as well as fluorescent markers for biological imaging. Examples of nontoxic materials that have been identified as viable candidates for environmentally-friendly quantum dots are Carbon and Silicon-based QDs, I-III-VI nanomaterials, and transition-metal doped ZnSe quantum dots.[8] In this section of the thesis I will focus on the family of I-III-VI QDs and ZnSe QDs due to their similarities in both synthetic procedures and chemical properties to other nanomaterials that our group has studied. Also, our group's proven capabilities to explore the photophysical properties of materials with broad emission and absorption spectra match well with current issues in these two fields. Here I will describe the current state of synthetic efforts toward creating devices with I-III-VI QDs, ways that the Engel Group can contribute to the field, and methods for improving our capabilities to meet the challenges of aiding nanomaterials discovery in the future.

A non-toxic alternative to Cd and Pb-based quantum dots that has gained traction for use in solar and light-emitting devices due to its high tunability, high quantum yield, small bulk bandgap, and promising photovoltaic properties in the bulk phase are the family of I-III-VI quantum dots. Popular examples of this group include $CuInSe_{(x)}S_{(2-x)}$ (CISeS),[9–14] $CuIn_{(x)}Ga_{(1-x)}Se_2$ (CIGS),[15–17] and their Ag-based alternatives (i.e. $AgInSe_2$)[9, 18–20]. These materials, particularly CIGS, are effective semiconducting materials as solid solution based thin films used for lightweight, flexible solar panel applications due to their high absorption coefficients.[21–23] $CuInS_2$ (CIS) quantum dots have a comparable crystal structure, similar excitonic oscillator strength, and slightly smaller bulk band gap than CdSe.

Therefore, both CIS and CdSe QDs are expected to have similar optical properties, with CIS QDs potentially acting as an effective non-toxic replacement for CdSe in LED and biological imaging devices, while also avoiding the use of harmful precursors used in the development of III-V QDs. However, the optoelectronic properties of CIS and CdSe QDs differ dramatically. CIS QDs have very broad absorption and emission features with ensemble photoluminescence (PL) linewidths on the order of 300 meV for core-shell CIS/ZnS particles.[12] Reminiscent with our findings with InP/ZnS quantum dots, studies by the Klimov group have shown that CIS quantum dots emit via recombination at a deep trap state, presumably a Cu defect with a variable oxidation state.[24] This causes single dot emission to be very narrow (<60 meV), while the ensemble PL linewidth is inhomogeneously broadened by emission from defects localized at different sites in the crystal. Though healing the surface dangling bond defects by coating the particles with a shell of ZnS aids in improving the PL quantum yield, the emission remains much broader than current CdSe core-shell nanomaterials. The principle challenge for both InP QDs and I-III-VI QDs is therefore a means to engineer defect or dopant states so that emission can only occur via a controllable subset of sites and types of defects.

The quantum dot materials in this family are particularly interesting because of their modularity. Unlike materials such as CdSe, ternary I-III-VI quantum dots can be made using non-stochiometric alloys of various atoms in the respective groups, which offers a new parameter space to optimize other than altering the size, shell composition, solvent, or capping ligands. For example, making materials like CIS with a deficiency of Cu atoms improves the PL quantum yield.[11] This is a common motif even in the bulk phase where CIGS thin film solar cells are often made to be Cu deficient, which improves power conversion efficiency by affecting the carrier mobility near the interface of the device. Also, in bulk CIGS, the band gap can be adjusted continuously between the $CuInSe_2$ band gap and the $CuGaSe_2$ gap by changing the relative amounts of In and Ga in the material.[25] This methodology translates into the nanophase, where modulating the stoichiometry of materials like CIGS

quantum dots offers an extra control over the band gap and other optoelectronic properties rather than controlling just the size and shape of the nanocrystals, like our studies of hybrid perovskite QDs.[26] In addition to adjusting the stoichiometry of the nanocrystalline material, dopant atoms can be added (most commonly Mn) to further alter the emission profile of I-III-VI quantum dots and have enabled white fluorescence with up to 75% quantum yield.[27]

The effect of incorporating dopant ions like Cu^{+}, Ag^{+}, and Mn^{2+} is also an important tool in the design of devices made using ZnSe/S QDs.[8, 28–30] ZnSe/S QDs are nontoxic materials that have tunable emission in the near UV. By controllably adding Cu, Ag, and Mn dopants into the nanocrystals, along with the intrinsic emission from ZnSe/S, broad green emission from Cu^{+} or Ag^{+} hole traps and sharper red/orange emission from Mn^{2+} centers can produce high quality white light LEDs.[31, 32] While emission from Mn centers doped into ZnSe/S quantum dots are independent of the nanocrystal size and shape, emission from Cu and Ag centers is tunable, offering a similar modular behavior to I-III-VI quantum dots. By tuning the concentrations of various dopants in the nanocrystal as well as the synthetic procedure, a tunable white light emission spectrum can be obtained, varying from cool to warm white light. Finally, another benefit that ZnSe/S quantum dots have over other technologies are the lack of spectral overlap between absorption and emission spectra. This is ideal for applications like LEDs whose performance can be affected by reabsorption of emissive photons by the material.

Two-dimensional electronic spectroscopy (2DES) is a powerful tool for investigating the electronic structure and quantum dynamics of systems with highly congested linear or transient absorption spectra. By spreading the third-order signal across two dimensions, it is possible to gain better state-to-state clarity in both spectral shape and energy transfer dynamics for complex systems. In I-III-VI QD materials, 2DES can be a valuable method to gain insight into defect-based emission for multiple reasons. First, both the absorption and emission spectra of CIS QDs are very broad. Using 2DES, it should be possible, especially

near 10 K, to resolve individual electronic states that are transferring energy into the photoluminescent state. Next, with better resolution and identification of the states that are participating in the emission, 2DES can pinpoint which states are coupled to other electronic states or the lattice via electron-phonon coupling, and whether there are optimal intra-gap defects or energy transfer pathways based on state specific lifetime measurements. Finally, the energy transfer events from exciton formation to hole trapping by vacancies and dopant impurities (as well as unwanted defects such as surface dangling bonds) happens on the time scale of a few hundred fs. Because of our broadband capabilities, it is possible for us to obtain sub-10 fs pulses, allowing for the investigation of these very fast energy transfer dynamics particularly for systems such as Mn:ZnSe that absorbs in the near-UV spectral range and emits near 700 nm after undergoing ultrafast charge transfer between the semiconductor electron-hole pairs and the metal centers embedded in the crystal lattice.

REFERENCES

[1] Olga I. Mićić, Kim M. Jones, Andrew Cahill, and Arthur J. Nozik. "Optical, Electronic, and Structural Properties of Uncoupled and Close-Packed Arrays of InP Quantum Dots". In: (1998).

[2] Minhaeng Cho, Tobias Brixner, Igor Stiopkin, Harsha Vaswani, and Graham R Fleming. "Two Dimensional Electronic Spectroscopy of Molecular Complexes". In: *Journal of the Chinese Chemical Society* 53.1 (2006), pp. 15–24.

[3] Peter D. Dahlberg, Po-Chieh Ting, Sara C. Massey, Marco A. Allodi, Elizabeth C. Martin, C. Neil Hunter, and Gregory S. Engel. "Mapping the ultrafast flow of harvested solar energy in living photosynthetic cells". In: *Nature Communications* 8.1 (Dec. 2017), p. 988. ISSN: 2041-1723.

[4] Artem A. Bakulin, Sarah E. Morgan, Tom B. Kehoe, Mark W. B. Wilson, Alex W. Chin, Donatas Zigmantas, Dassia Egorova, and Akshay Rao. "Real-time observation of multiexcitonic states in ultrafast singlet fission using coherent 2D electronic spectroscopy". In: *Nature Chemistry* 8.1 (Jan. 2016), pp. 16–23. ISSN: 1755-4330.

[5] Antonietta De Sio, Franco V. d. A. Camargo, Katrin Winte, Ephraim Sommer, Federico Branchi, Giulio Cerullo, and Christoph Lienau. "Ultrafast relaxation dynamics in a polymer: fullerene blend for organic photovoltaics probed by two-dimensional electronic spectroscopy". In: *The European Physical Journal B* 91.10 (Oct. 2018), p. 236. ISSN: 1434-6028.

[6] Daniele M. Monahan, Liang Guo, Jia Lin, Letian Dou, Peidong Yang, and Graham R. Fleming. "Room-Temperature Coherent Optical Phonon in 2D Electronic Spectra of CH_3 NH_3 PbI_3 Perovskite as a Possible Cooling Bottleneck". In: *The Journal of Physical Chemistry Letters* 8.14 (July 2017), pp. 3211–3215. ISSN: 1948-7185.

[7] Annalisa Brodu, Mariana V. Ballottin, Jonathan Buhot, Elleke J. van Harten, Dorian Dupont, Andrea La Porta, P. Tim Prins, Mickael D. Tessier, Marijn A. M. Versteegh, Val Zwiller, Sara Bals, Zeger Hens, Freddy T. Rabouw, Peter C. M. Christianen, Celso de Mello Donega, and Daniel Vanmaekelbergh. "Exciton Fine Structure and Lattice Dynamics in InP/ZnSe Core/Shell Quantum Dots". In: *ACS Photonics* 5.8 (Aug. 2018), pp. 3353–3362. ISSN: 2330-4022.

[8] Adita Das and Preston T. Snee. "Synthetic Developments of Nontoxic Quantum Dots". In: *ChemPhysChem* 17.5 (Mar. 2016), pp. 598–617. ISSN: 14394235.

[9] Peter M. Allen and Moungi G. Bawendi. "Ternary I-III-VI Quantum Dots Luminescent in the Red to Near-Infrared". In: *Journal of the American Chemical Society* 130.29 (July 2008), pp. 9240–9241. ISSN: 0002-7863.

[10] J. Scott Niezgoda, Eugene Yap, Joseph D. Keene, James R. McBride, and Sandra J. Rosenthal. "Plasmonic Cu_x In_yS_2 Quantum Dots Make Better Photovoltaics Than Their Nonplasmonic Counterparts". In: *Nano Letters* 14.6 (June 2014), pp. 3262–3269. ISSN: 1530-6984.

[11] P. Ilaiyaraja, Pavana S. V. Mocherla, T. K. Srinivasan, and C. Sudakar. "Synthesis of Cu-Deficient and Zn-Graded Cu–In–Zn–S Quantum Dots and Hybrid Inorganic–Organic Nanophosphor Composite for White Light Emission". In: *ACS Applied Materials & Interfaces* 8.19 (May 2016), pp. 12456–12465. ISSN: 1944-8244.

[12] Huidong Zang, Hongbo Li, Nikolay S. Makarov, Kirill A. Velizhanin, Kaifeng Wu, Young-Shin Park, and Victor I. Klimov. "Thick-Shell $CuInS_2$ /ZnS Quantum Dots with Suppressed "Blinking" and Narrow Single-Particle Emission Line Widths". In: *Nano Letters* 17.3 (Mar. 2017), pp. 1787–1795. ISSN: 1530-6984.

[13] Liang Li, T. Jean Daou, Isabelle Texier, Tran Thi Kim Chi, Nguyen Quang Liem, and Peter Reiss. "Highly Luminescent $CuInS_2$ /ZnS Core/Shell Nanocrystals: Cadmium-

Free Quantum Dots for In Vivo Imaging". In: *Chemistry of Materials* 21.12 (June 2009), pp. 2422–2429. ISSN: 0897-4756.

[14] Haizheng Zhong, Zhibin Wang, Enrico Bovero, Zhenghong Lu, Frank C. J. M. van Veggel, and Gregory D. Scholes. "Colloidal $CuInSe_2$ Nanocrystals in the Quantum Confinement Regime: Synthesis, Optical Properties, and Electroluminescence". In: *The Journal of Physical Chemistry C* 115.25 (June 2011), pp. 12396–12402. ISSN: 1932-7447.

[15] Matthew G. Panthani, Vahid Akhavan, Brian Goodfellow, Johanna P. Schmidtke, Lawrence Dunn, Ananth Dodabalapur, Paul F. Barbara, and Brian A. Korgel. "Synthesis of $CuInS_2$, $CuInSe_2$, and $Cu(In_xGa_{x-1})Se_2$ (CIGS) Nanocrystal "Inks" for Printable Photovoltaics". In: *Journal of the American Chemical Society* 130.49 (Dec. 2008), pp. 16770–16777. ISSN: 0002-7863.

[16] Dae-Yeon Jo, Daekyoung Kim, Jong-Hoon Kim, Heeyeop Chae, Hyo Jin Seo, Young Rag Do, and Heesun Yang. "Tunable White Fluorescent Copper Gallium Sulfide Quantum Dots Enabled by Mn Doping". In: *ACS Applied Materials & Interfaces* 8.19 (May 2016), pp. 12291–12297. ISSN: 1944-8244.

[17] Jinjin Zhao, Jiangbin Zhang, Wenna Wang, Peng Wang, Feng Li, Deliang Ren, Huanyan Si, Xiuguo Sun, Fengqiu Ji, and Yanzhong Hao. "Facile synthesis of $CuInGaS_2$ quantum dot nanoparticles for bilayer-sensitized solar cells". In: *Dalton Trans.* 43.44 (Oct. 2014), pp. 16588–16592. ISSN: 1477-9226.

[18] Meng T. Ng, Chris B. Boothroyd, and Jagadese J. Vittal. "One-Pot Synthesis of New-Phase AgInSe2 Nanorods". In: (2006).

[19] Yasushi Hamanaka, Tetsuya Ogawa, Masakazu Tsuzuki, and Toshihiro Kuzuya. "Photoluminescence Properties and Its Origin of $AgInS_2$ Quantum Dots with Chalcopyrite Structure". In: *The Journal of Physical Chemistry C* 115.5 (Feb. 2011), pp. 1786–1792. ISSN: 1932-7447.

[20] Michelle D. Regulacio, Khin Yin Win, Seong Loong Lo, Shuang-Yuan Zhang, Xinhai Zhang, Shu Wang, Ming-Yong Han, and Yuangang Zheng. "Aqueous synthesis of highly luminescent AgInS2–ZnS quantum dots and their biological applications". In: *Nanoscale* 5.6 (Mar. 2013), p. 2322. ISSN: 2040-3364.

[21] Adrian Chirilă, Stephan Buecheler, Fabian Pianezzi, Patrick Bloesch, Christina Gretener, Alexander R. Uhl, Carolin Fella, Lukas Kranz, Julian Perrenoud, Sieghard Seyrling, Rajneesh Verma, Shiro Nishiwaki, Yaroslav E. Romanyuk, Gerhard Bilger, and Ayodhya N. Tiwari. "Highly efficient Cu(In,Ga)Se2 solar cells grown on flexible polymer films". In: *Nature Materials* 10.11 (Nov. 2011), pp. 857–861. ISSN: 1476-1122.

[22] Yu-Kuang Liao, Maël Brossard, Dan-Hua Hsieh, Tzu-Neng Lin, Martin D. B. Charlton, Shun-Jen Cheng, Chyong-Hua Chen, Ji-Lin Shen, Lung-Teng Cheng, Tung-Po Hsieh, Fang-I Lai, Shou-Yi Kuo, Hao-Chung Kuo, Pavlos G. Savvidis, and Pavlos G. Lagoudakis. "Highly Efficient Flexible Hybrid Nanocrystal-Cu(In,Ga)Se_2 (CIGS) Solar Cells". In: *Advanced Energy Materials* 5.2 (Jan. 2015), p. 1401280. ISSN: 16146832.

[23] F. Kessler, D. Herrmann, and M. Powalla. "Approaches to flexible CIGS thin-film solar cells". In: *Thin Solid Films* 480-481 (June 2005), pp. 491–498. ISSN: 0040-6090.

[24] Addis S. Fuhr, Hyeong Jin Yun, Nikolay S. Makarov, Hongbo Li, Hunter McDaniel, and Victor I. Klimov. "Light Emission Mechanisms in $CuInS_2$ Quantum Dots Evaluated by Spectral Electrochemistry". In: *ACS Photonics* 4.10 (Oct. 2017), pp. 2425–2435. ISSN: 2330-4022.

[25] Miguel Contreras, John Tuttle, Dahong Du, Yi Qi, Amy Swartzlander, Andrew Tennant, and Rommel Noufi. "Graded band-gap Cu(In,Ga)Se_2 thin-film solar cell absorber with enhanced open-circuit voltage". In: *Applied Physics Letters* 63.13 (Sept. 1993), pp. 1824–1826. ISSN: 0003-6951.

[26] Yu-Hsiang A. Wang, Xiaoyan Zhang, Ningzhong Bao, Baoping Lin, and Arunava Gupta. "Synthesis of Shape-Controlled Monodisperse Wurtzite $CuIn_xGa_{1-x}S_2$ Semi-

conductor Nanocrystals with Tunable Band Gap". In: *Journal of the American Chemical Society* 133.29 (July 2011), pp. 11072–11075. ISSN: 0002-7863.

[27] Xi Yuan, Ruixin Ma, Wenjin Zhang, Jie Hua, Xiangdong Meng, Xinhua Zhong, Jiahua Zhang, Jialong Zhao, and Haibo Li. "Dual Emissive Manganese and Copper Co-Doped Zn–In–S Quantum Dots as a Single Color-Converter for High Color Rendering White-Light-Emitting Diodes". In: *ACS Applied Materials & Interfaces* 7.16 (Apr. 2015), pp. 8659–8666. ISSN: 1944-8244.

[28] Zhi-Qiang Zhou, Li-Yun Yang, Ren Yan, Jie Zhao, Yu-Qi Liu, Lu Lai, Feng-Lei Jiang, Thomas Maskow, and Yi Liu. "Mn-Doped ZnSe quantum dots initiated mild and rapid cation exchange for tailoring the composition and optical properties of colloid nanocrystals: novel template, new applications". In: *Nanoscale* 9.8 (Feb. 2017), pp. 2824–2835. ISSN: 2040-3364.

[29] Ronghui Zhou, Shaokai Sun, Chenghui Li, Lan Wu, Xiandeng Hou, and Peng Wu. "Enriching Mn-Doped ZnSe Quantum Dots onto Mesoporous Silica Nanoparticles for Enhanced Fluorescence/Magnetic Resonance Imaging Dual-Modal Bio-Imaging". In: *ACS Applied Materials & Interfaces* 10.40 (Oct. 2018), pp. 34060–34067. ISSN: 1944-8244.

[30] Subhendu K. Panda, Stephen G. Hickey, Hilmi Volkan Demir, and Alexander Eychmüller. "Bright White-Light Emitting Manganese and Copper Co-Doped ZnSe Quantum Dots". In: *Angewandte Chemie International Edition* 50.19 (May 2011), pp. 4432–4436. ISSN: 14337851.

[31] Qiu-hang CHEN, Shi-liang MEI, Wu YANG, Wan-lu ZHANG, Gui-lin ZHANG, Jiatao ZHU, and Rui-qian GUO. "Tunable emission of cadmium-free transition metal (Cu, Mn, Ag) co-doped ZnInS/ZnS core-shell quantum dots". In: *Transactions of Nonferrous Metals Society of China* 28.8 (Aug. 2018), pp. 1611–1617. ISSN: 1003-6326.

[32] Lucheng Peng, Dongze Li, Zhuolei Zhang, Keke Huang, Ying Zhang, Zhan Shi, Renguo Xie, and Wensheng Yang. “Large-scale synthesis of single-source, thermally stable, and dual-emissive Mn-doped Zn–Cu–In–S nanocrystals for bright white light-emitting diodes”. In: *Nano Research* 8.10 (Oct. 2015), pp. 3316–3331. ISSN: 1998-0124.

CHAPTER 7

CONCLUSION

Semiconductor nanocrystals continue to attract significant research and industrial attention due to their size and shape dependent optoelectronic properties and large surface-volume ratio, which make them ideal candidates to make an impact on creating renewable sources of energy, developing targeted drug delivery systems, and efficiently brightening our homes. To further develop these materials into useful industrial-scale devices, their fundamental physical properties including ultrafast carrier dynamics and electronic structure should be well-understood to best inform synthetic efforts. Throughout this thesis, I use a third-order nonlinear spectroscopy called two-dimensional electronic spectroscopy (2DES) to study a variety of semiconductor nanocrystals including InP quantum dots (QDs), methylammonium lead-halide ($MAPbX_3$) perovskite QDs, and CdSe nanoplatelets. These materials all have high applicability to modern devices, but require a deeper understanding of their electronic strucutre and ultrafast carrier dynamics to become viable players in the industrial landscape. In addition to getting direct information about inhomogenous/homogeneous broadening, ultrafast relaxation times, and quantum coherences between states, the use of 2DES in these projects also highlights the value of collaborative exploration of these materials. 2DES is able to effectively complement studies such as nanosecond transient absorption, raman spectroscopy, transmission electron microscopy, and photoluminescence excitation spectroscopy to drive toward solutions of synthetic nanomaterials problems. In chapter 3, 2DES was used along with other characterization techniques to understand the origin of the broad emission feature in InP QDs. Through the data presented, it was clear that emission in InP QDs occurs via recombination between a delocalized electron and a localized hole state that relaxes to a shallow mid-gap trap state. This localized hole state is then heavily influenced by lattice vibrations, producing a stronger electron-phonon coupling and broad emission spectra. These shallow hole traps are introduced while healing surface traps of as-synthesized InP QDs by adding a shell layer of ZnS or etching the surface with HF, creating interstitial

and substitutional defects in the crystal lattice. This points to the potential synthetic solution of using only III-V materials for healing surface defects of InP QDs, which will solve substitutional issues with ions like Zn^{2+} as well as strain-induced defects resulting from a lattice mismatch. After developing a ligand-mediated transport synthesis of methyl-ammonium lead-halide perovskite QDs in chapter 4, we used 2DES and nanosecond transient absorption to examine the material's electronic structure and ultrafast carrier dynamics. The QDs were synthesized under ambient conditions and were shown to be scalable, paving the way toward synthetic techniques that can be industrially realized. Transient absorption measurements showed that the photoluminescence decay was independent of pump power, indicating that direct excitonic recombination is the dominant decay pathway in these QDs. The 2DES experiments showed multiple electronic states that shift with the size of the particles and sub-50 fs excitonic relaxation times. Additionally, we observed that the QDs show quantum beating signals in the upper diagonal region of the spectrum. Finally, in chapter 5, I studied 6 monolayer thick CdSe nanoplatelet thin films using 2DES under different fluences and at both room temperature and 77K. The spectra showed distinct excitonic features arising from the heavy hole and light hole states of these colloidal quantum well materials. The excitonic states decay rapidly (sub-50 fs) to the band edge and the heavy hole and light hole states display pronounced electronic coherences even at room temperature. At 77K, the spectra were noisier both because of the slight instability of the continuous flow cryostat affecting the pulse overlap throughout the experiment and photobleaching of the nanoplatelet thin film at powers higher than 500 pJ/pulse. The performance of the next generation of nanomaterial-based LEDs, solar cells, and bioimaging devices critically relies on the details of carrier relaxation pathways, electronic structure, state-to-state electronic and electron-phonon coupling, and multiexciton effects. This dissertation highlights the ability to discover the design principles of novel semiconductor nanomaterials by understanding their electronic structure and ultrafast carrier dynamics through powerful spectroscopic techniques like 2DES. Using these experimental results, we can learn both about the nanomaterials systems that we

studied and how the spectroscopic techniques we are using can be tailored to advance this rapidly evolving field. In the coming years it will become increasingly important to make multidimensional spectroscopic experiments and their results more accessible to a wide-array of researchers that want to learn more about the diverse applicability of nanomaterials. This thesis can hopefully serve as a starting point for collaborative explorations of the interesting physical phenomena produced by semiconductor nanocrystals and lead to the development of spectroscopic methods that can create high-throughput analysis of materials in real device environments.

Appendices

APPENDIX A

PHASE CORRECTIONS IN 2D ELECTRONIC SPECTROSCOPY

When performing two-dimensional electronic spectroscopy (2DES) experiments in the BOXCARS geometry, it is necessary to correct errors in the timing between pulses 1 and 2 as well as pulses 3 and 4 in post-processing. These errors arise due to minute changes in the relative path length of the individual beams as they travel different paths and hit different optics, or travel through transmissive optics or the sample itself at slightly different angles. While it is useful to implement BOXCARS 2D spectrometer designs that use only reflective optics, the relative timing differences needed to alter the phase of the emitted signal cannot be properly compensated by physical optics or controlled by even high-precision delay stages.[1] In the BOXCARS geometry, the three ultrafast pulses that induce the third-order polarization and the local oscillator pulse that is used for heterodyne detection of the emitted signal are focused on the sample position in a box-shaped formation with one beam at each corner (Figure A.1a). The four beams then overlap at the focus, which is positioned to be within the sample volume and exit the sample position as the inverse of the incident box pattern, with the signal emitted in the same direction as the local oscillator pulse. To precisely form a symmetric box pattern both before and after the focus, each beam must have at least one independent controlling mirror, meaning that as the system drifts over the course of an 8-hour 2DES experiment, the four beams will not drift in unison. Therefore, if changes in beam pointing occur, there will be changes in the relative phase of the beams as they interact with the sample. Even in the ideal case that these long-term drifts do not occur, and the system is perfectly stable, the level of timing precision needed to accurately set all pulses to interact at the sample with the same phase is unobtainable. Because of this, it will be impossible to properly separate the real and imaginary parts of the complex signal without first correcting this phase error. Many solutions been implemented to circumvent the phas-

ing issue entirely using a colinear geometry rather than the BOXCARS geometry described above.[2–4] This geometry is identical to a pump probe experiment, but since pulses 1 and 2 need to have controllable timings, a diffractive-optic-based multiple pulse generator must be used in the pump beam path (Figure A.1b). This design forces pulses 1 and 2 to travel the same beam path and to hit identical optics, simplifying the optical alignment and removing the need for phasing. However, there are drawbacks to the pump-probe geometry. Most importantly, the signal-to-noise ratio is worse in a pump-probe geometry both because the collected signal measures often small differences between the probe and pump plus probe spectra, and the signal is no longer naturally background-free since much of the scatter induced by beam 3 travel with the signal and is extremely difficult to remove. Also, just as in a pump probe experiment, 2DES in the colinear geometry produces a real-valued signal on the camera, making it impossible to isolate the rephasing and non-rephasing pathways without phase-cycling methods to recover the full complex-valued data set. Finally, it is not possible to perform experiments such as two-quantum measurements that are used to study phenomena such as biexciton dynamics in semiconductor quantum wells.[5]

If the BOXCARS geometry is used, post-processing methods must be developed to correctly segment the real part of the signal from the imaginary part. The most common of these methods is to separately obtain a pump probe spectrum with the same laser system, laser spectrum, lab conditions, pump powers, and identical compensation for transmissive optical elements as the BOXCARS 2DES setup. The collected pump probe spectrum will then be identical to the real-valued 2DES spectrum if the 2D signal is projected onto the detection axis (all points on the excitation axis are summed together to mimic the lack of excitation timing control in pump probe). The most common phasing method in our group is an unconstrained Nedler-Mead searching algorithm that consists of 3 iterative steps. First, for some waiting time, the summed down 2DES frame is compared with the pump probe spectrum at the same waiting time, with each normalized to the maximum of their absolute valued spectra. The total root mean square (RMS) deviation between the two spectra is

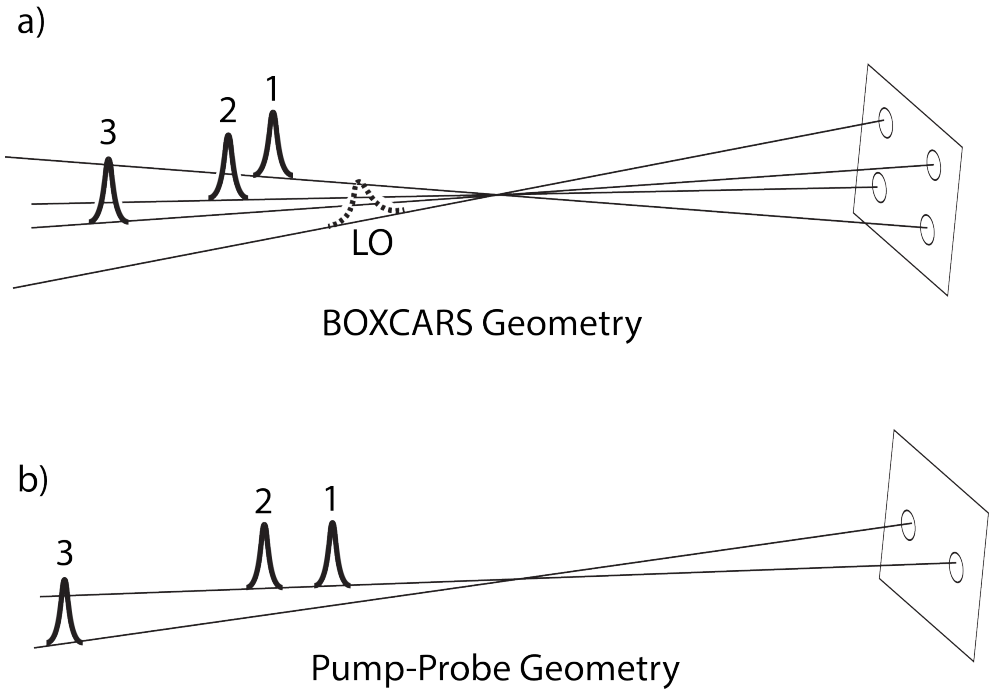

Figure A.1: a) In the BOXCARS 2D Electronic Spectroscopy beam geometry, each beam travels along an independent path in space and will all hit different optics, making this geometry susceptible to minute errors in timing. However, since the signal is emitting in a phase-matched direction with the local oscillator beam and free of a scattering background, the signal-to-noise is improved over the pump probe geometry. b) In the pump-probe geometry, pulses 1 and 2 travel along the same beam path, eliminating errors in the inter-pulse phase due to interacting with different optics or altering the beam pointing.

used as the error metric to minimize in the algorithm. Then, the Nedler-Mead algorithm optimizes a six-parameter phase function by guessing a solution, multiplying the entire 2DES waiting time frame by this phase, determining the RMS deviation from the pump probe spectrum, and searching until a local minimum error is found. Finally, the phase function is applied to the entire 2DES cube, properly separating the real and imaginary parts of the signal. However, this method is sometimes not adequate to properly phase a 2DES data cube. The phase function consists of 6 parameters: an amplitude factor (A), a constant phase factor (ϕ), and linear and quadratic phase corrections in both the excitation (τ) and detection (t) axes.[6] In the following subsections, various situations that can cause non-ideal phasing are discussed along with routes toward refining the fitting algorithm to overcome these challenges.

A.1 Spectral Drift between 2DES Experiment and Pump Probe

As the 2DES community moves toward octave-spanning ultrabroadband laser spectra as an adaptable way to study materials that have electronic states in disparate regions of the visible spectrum, or as a high-throughput tool to study many samples with different spectra, phasing 2DES data becomes inherently more challenging. This is because when working with white light sources such as our system that focuses the output of the regenative amplifier (regen) into a tube of pressurized Argon and broadens the spectrum through a self-phase modulation process, any slight drifts in beam pointing from the regen or changes to the pulse compression will change the spectrum. Usually, the power and beam pointing from the Ti:Sapphire oscillator that seeds the regen cavity will drift over the course of a few days to a few weeks due to oil and dust buildup on the Ti:Sapphire crystal that must be cleaned regularly. This will affect the alignment into the stretcher of the regen and change the output compression. While the phasing procedures for a data set collected with direct regen output is often straightforward, the small changes in compression greatly affect data collected with Ar-based white light. While the spectrum may not drift significantly over the

course of a single 2DES experiment, after a series of 2DES experiments and after the time to switch the system over to a pump probe setup for phasing, the spectrum will often drift enough to make the pump probe trace a non-ideal representative of the summed down 2DES spectrum. There are some ways to mitigate these issues using the optics on the table rather than post-processing, such as using a hermetically sealed oscillator to prevent drift entirely or collecting pump probe spectra immediately before or after each 2DES experiment. However, these solutions are often not practical due to cost for both new instrumentation and upkeep as well as the time that it takes to swap between experimental setups, and in the end these answers may not completely resolve the phasing issues, particularly if the environmental conditions in the laser lab are not well-stabilized. In these cases where the laser spectrum drifts not within the timeframe of an experiment, but between the 2DES experiment and the pump probe data collection, some changes to the phasing algorithm can help to produce consistent phasing of the 2DES signal. First, if the laser spectrum is broader than the all the electronic states of interest, a portion of the 2DES data frame may be able to be phased easily (i.e. the algorithm can converge to a solution quickly and consistently even with different starting parameters). This becomes more applicable the closer the electronic states are to the 800 nm fundamental of the Ti:Sapphire regen output. When the compression out of the regen drifts, the extreme blue (<575 nm) and extreme red (>875 nm) will be affected the most, making the edges of the spectrum very hard to phase and show very inconsistent phase parameters. However, if the signals of interest are in these blue or red regions of the spectrum other phasing methods may need to be used, which will be outlined in the following sections.

A.2 Spectral drift and beam pointing changes during a 2DES experiment

A complementary issue that is much more difficult to deal with than the slow drift described above is when the spectrum or beam pointing changes over the course of a 2DES experiment. In this case, being able to find a good fit between the 2DES spectrum and the pump probe scan at just one or a few waiting time points and applying those parameters to the entire data cube is no longer adequate. The phase parameters will change at each time point, so each 2DES frame must be phased independently. However, the phase parameters should vary continuously throughout the experiment. When applying the typical phasing procedure to these types of data sets, it is not uncommon to see discontinuous jumps from one waiting time point to the next, which even if the system is drifting over time, is likely not physical. The Nedler-Mead algorithm is an unconstrained search and at any two time points, the algorithm may find different local minima that are very close in the total RMS error. One method that can make phasing these types of data sets approachable and circumvent the issues with unconstrained searching algorithms is to use a constrained algorithm. In a method employed by our group, we use a Nedler-Mead algorithm to find an initial set of parameters at some waiting time point that is taken about halfway through the experiment. Then, using an interior-point algorithm that is constrained so that the phase parameters cannot change discontinuously (e.g.$\pm\sim$30% of the initial value), the rest of the waiting time point phase parameters are calculated, first running forward in time and then backwards to converge on an acceptable minimum error at each point. This method can also be used for issues with spectral drift between the 2DES data acquisition and taking the pump probe spectrum since from one frame to the next, the error may be dominated by the blue or red edge of the spectrum and it may be necessary to look at all data frames and find a consistent set of parameters that averages over fluctuations at the edges of the spectrum, which are inherently less stable over time.

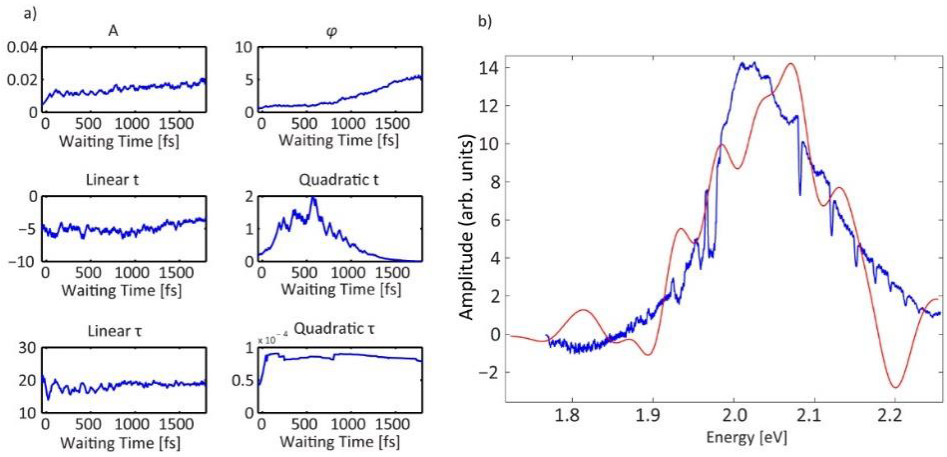

Figure A.2: a) Here the six phase parameters that are fit by the constrained interior-point algorithm are depicted for all waiting times for an InP/ZnS Quantum Dot data set. The parameters are obtained by starting at the midpoint of the waiting time axis and run forwards, and then backwards with constraints to ensure continuity. b) A pump probe trace (blue) plotted alongside a 2DES sum down spectrum showing a minimum error as found by the interior-point algorithm.

Our group and others continue to develop methods for dealing with the phasing issue in 2D electronic spectroscopy. The most glaring problem is that while pump probe acts as an excellent proxy for the sum down of the detection axis in the 2DES spectrum, there is no effective equivalent in the excitation axis to constrain the fitting algorithm in both dimensions. Therefore, there are infinite solutions to phasing that can yield a perfect fit to a pump probe spectrum and discerning the most consistent and physically reasonable set of phase parameters is an inexact process. Though methods like using the heterodyned transient grating signal have been developed to add additional constraints on the fitting parameters,[7] this method is still susceptible to spectral changes and inherent challenges when using thin film samples where no solvent reference is applicable. It is entirely possible that the pump-probe geometry is the most fruitful direction and that a high signal-to-noise colinear 2DES method will be developed that can give at least real-valued spectra with high-throughput. However, it is important not only to approach the challenges inherent in the phasing process and develop more consistent methods of producing accurately phased data, but it is vital to understand that these issues exist when analyzing and interpreting the

results of 2D electronic spectroscopy to successfully impact any field aiming to understand energy transfer and charge carrier dynamics in complex systems.

REFERENCES

[1] T. Brixner, T. Mancal, I. V. Stiopkin, and G. R. Fleming. "Phase-stabilized two-dimensional electronic spectroscopy". In: *Journal of Chemical Physics* 121.9 (2004), pp. 4221–4236. ISSN: 0021-9606.

[2] Erik M. Grumstrup, Sang-Hee Shim, Matthew A. Montgomery, Niels H. Damrauer, and Martin T. Zanni. "Facile collection of two-dimensional electronic spectra using femtosecond pulse-shaping Technology". In: *Optics Express* 15.25 (Dec. 2007), p. 16681. ISSN: 1094-4087.

[3] Sang-Hee Shim and Martin T. Zanni. "How to turn your pump–probe instrument into a multidimensional spectrometer: 2D IR and Vis spectroscopiesvia pulse shaping". In: *Phys. Chem. Chem. Phys.* 11.5 (Feb. 2009), pp. 748–761. ISSN: 1463-9076.

[4] Franklin D. Fuller, Daniel E. Wilcox, and Jennifer P. Ogilvie. "Pulse shaping based two-dimensional electronic spectroscopy in a background free geometry". In: *Optics Express* 22.1 (Jan. 2014), p. 1018. ISSN: 1094-4087.

[5] Katherine W Stone, Kenan Gundogdu, Daniel B Turner, Xiaoqin Li, Steven T Cundiff, and Keith A Nelson. "Two-quantum 2D FT electronic spectroscopy of biexcitons in GaAs quantum wells." In: *Science (New York, N.Y.)* 324.5931 (May 2009), pp. 1169–73. ISSN: 1095-9203.

[6] Haibin Zheng, Justin R Caram, Peter D Dahlberg, Brian S Rolczynski, Subha Viswanathan, Dmitriy S Dolzhnikov, Amir Khadivi, Dmitri V Talapin, and Gregory S Engel. "Dispersion-free continuum two-dimensional electronic spectrometer". In: *Applied Optics* 53.9 (2014), pp. 1909–1917. ISSN: 1559-128X.

[7] Franz Milota, Craig N. Lincoln, and Jürgen Hauer. "Precise phasing of 2D-electronic spectra in a fully non-collinear phase-matching geometry". In: *Optics Express* 21.13 (July 2013), p. 15904. ISSN: 1094-4087.

APPENDIX B

RELATION BETWEEN THE BULK AND THE NANOSCALE

Much attention is given to the size-dependent properties of nanoscale materials and how they differ dramatically from their bulk-scale counterparts. However, analysis of bulk materials offers important insights into how the nanoscale system will behave in various environments. In particular, understanding the electronic structure, the transport properties, and the impact of defects on the material behavior are all challenges that nanomaterials researchers face that have been studied with great effect in the bulk phase for decades. For example, the electronic wavefunctions of quantum dots are approximately given by the solutions to the particle-in-a-sphere Schodinger equation times an envelope function that is dependent on the underlying symmetries of the crystal lattice.[1] In the case of a free-electron model, the conduction and valence band states are parabolic and yield the simple expressions described in chapter 2. However, this is never the case, and the bulk band structure needs to be applied to the nanomaterial to yield the correct state symmetries, effective masses of electrons and holes, and account for intra-band coupling and spin-orbit coupling. The nanocrystal envelope wavefunctions will then often closely resemble the bulk wavefunctions for states at the center of Brillouin zone (Γ), however for some materials such as InP and other related III-V semiconductors, the L-valley states must be included as well.[2] In addition to similarities in electronic structure, for nanomaterials with higher dimensionality such as nanoplatelets, nanorods, or nanowires, charge carrier transport is similar to bulk phase materials in the unconfined dimensions.[3] Finally, important properties like the charge carrier effective masses are determined by the curvature of the bulk band structure near the Brillouin zone center, which is again reliant on computation of the bulk electronic structure and applying it to the nanoscale material.[1, 2, 4] Some of the earliest attempts at determining bulk band structure involved solving the Schrodinger equation for a perfect infinite crystal lattice of the semiconducting material for specific points of symmetry (Γ, X, L, etc.) and then using 2nd order perturbation theory to determine how the bands flow from each point of symmetry

to every 7other one. This methodology known as k dot p theory was first explored by Luttinger, Kohn, and Kane[5–7] in the 1950s and is still an active area of research today, with the method being particularly useful for understanding anharmonicities around the points of symmetry that can impact carrier transport.[8] However, the Luttinger-Kohn model only takes the heavy hole and light hole states into account, and therefore in many cases more intensive models must be developed to include more and more excited electron and hole states. Examples of these methods include the the Kane 6-band model,[6] which includes the split-off band, and the 8-band Pidgeon-Brown model[9] that can more accurately capture phenomena like electron-hole coupling.

Another example of the ways in which nanomaterials researchers can benefit from the decades-long efforts of materials scientists studying bulk-phase semiconductors is the understanding of defect states and dopant atoms and their impact on carrier dynamics and electronic structure. Often mid-gap trap states like surface dangling bonds, dopant atoms, or vacancies in the semiconductor crystal structure will have detrimental effects on the photoluminescence quantum yield in light emitting applications or quantum efficiency in solar devices. Though the material electronic wavefunction of the nanosystem may differ greatly from the bulk, the nature of localized mid-gap defects, such as surface dangling bonds, and how they affect transport and optical properties are often very similar.[10] Moreover, these types of defects are often more often studied in the bulk phase using high precision techniques like scanning tunneling microscopy/spectroscopy which can help researchers learn more about the formation and electronic structure of these states in both bulk and low dimensional systems.[11–15] By using these results and others across decades of research into the electronic structure and materials properties of bulk semiconductors, researchers can gain insight into the toughest problems that hamper the successful development of nanocrystalline devices. Hopefully this small appendix can serve as a jumping-off point to inspire others to familiarize themselves with the theoretical and experimental techniques that have served materials scientists well for years so that they may help drive innovation in nanocrystal

synthesis and spectroscopy in the future.

REFERENCES

[1] Al. L. Efros and M Rosen. "The Electronic Structure of Semiconductor Nanocrystals". en. In: *Annual Review of Materials Science* 30.1 (Aug. 2000), pp. 475–521. ISSN: 0084-6600.

[2] Huaxiang Fu, Lin-Wang Wang, and Alex Zunger. "Applicability of the k p method to the electronic structure of quantum dots". In: *Physical Review B* 57.16 (Apr. 1998), pp. 9971–9987. ISSN: 0163-1829.

[3] Peter Y. Yu and Manuel Cardona. *Fundamentals of Semiconductors*. Graduate Texts in Physics. Berlin, Heidelberg: Springer Berlin Heidelberg, 2010. ISBN: 978-3-642-00709-5.

[4] Peter C. Sercel and Kerry J. Vahala. "Analytical formalism for determining quantum-wire and quantum-dot band structure in the multiband envelope-function approximation". In: *Physical Review B* 42.6 (Aug. 1990), pp. 3690–3710. ISSN: 0163-1829.

[5] J. M. Luttinger and W. Kohn. "Motion of Electrons and Holes in Perturbed Periodic Fields". In: *Physical Review* 97.4 (Feb. 1955), pp. 869–883. ISSN: 0031-899X.

[6] E.O. Kane. "Energy band structure in p-type germanium and silicon". In: *Journal of Physics and Chemistry of Solids* 1.1-2 (Sept. 1956), pp. 82–99. ISSN: 0022-3697.

[7] Evan O. Kane. "Band structure of indium antimonide". In: *Journal of Physics and Chemistry of Solids* 1.4 (Jan. 1957), pp. 249–261. ISSN: 0022-3697.

[8] Indranil Mal, Asish Hazra, D. P. Samajdar, and T. D. Das. "Computation of Electronic and Optical Properties of GaAsNSb with 16 Band k dot p Model". In: Springer, Cham, Dec. 2019, pp. 241–248.

[9] C. R. Pidgeon and R. N. Brown. "Interband Magneto-Absorption and Faraday Rotation in InSb". In: *Physical Review* 146.2 (June 1966), pp. 575–583. ISSN: 0031-899X.

[10] Huaxiang Fu and Alex Zunger. "InP quantum dots: Electronic structure, surface effects, and the redshifted emission". In: *Phys. Rev. B* 56 (3 July 1997), pp. 1496–1508.

[11] S. Urazhdin, D. Bilc, S. H. Tessmer, S. D. Mahanti, Theodora Kyratsi, and M. G. Kanatzidis. "Scanning tunneling microscopy of defect states in the semiconductor Bi2Se3". In: *Physical Review B* 66.16 (Oct. 2002), p. 161306. ISSN: 0163-1829.

[12] Ph. Ebert. "Defects in III-V semiconductor surfaces". In: *Applied Physics A: Materials Science & Processing* 75.1 (July 2002), pp. 101–112. ISSN: 0947-8396.

[13] X. de la Broïse, C. Delerue, M. Lannoo, B. Grandidier, and D. Stiévenard. "Theory of scanning tunneling microscopy of defects on semiconductor surfaces". In: *Physical Review B* 61.3 (Jan. 2000), pp. 2138–2145. ISSN: 0163-1829.

[14] Hajin Kim, J. Lee, S.-J. Kahng, Y.-W. Son, S. B. Lee, C.-K. Lee, J. Ihm, and Young Kuk. "Direct Observation of Localized Defect States in Semiconductor Nanotube Junctions". In: *Physical Review Letters* 90.21 (May 2003), p. 216107. ISSN: 0031-9007.

[15] Warren Wu, John R. Tucker, Glenn S. Solomon, and James S. Harris. "Atom-resolved scanning tunneling microscopy of vertically ordered InAs quantum dots". In: *Applied Physics Letters* 71.8 (Aug. 1997), pp. 1083–1085. ISSN: 0003-6951.